RICE UNIVERSITY

Thermal conductances of aligned structures and thin films with embedded carbon nanotubes

by

Sukesh Shenoy

A THESIS SUBMITTED
IN PARTIAL FULFILLMENT OF THE
REQUIREMENTS FOR THE DEGREE

Doctor of Philosophy

APPROVED, THESIS COMMITTEE

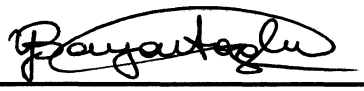

Dr. Yildiz Bayazitoglu,
H.S. Cameron Professor of Mechanical Engineering, Chair

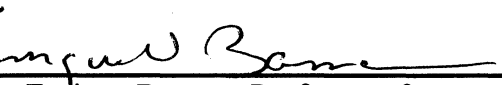

Dr. Enrique Barrera, Professor of Materials Science, Co-Chair

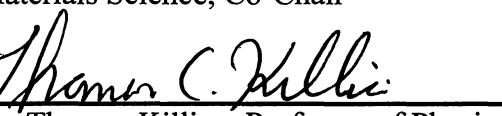

Dr. Thomas Killian, Professor of Physics and Astronomy

HOUSTON, TEXAS
May 2012

Thermal conductances of aligned structures and thin films with embedded carbon nanotubes

by

Sukesh Shenoy

Abstract

Individual carbon nanotubes (CNTs) have superior thermal conductivity than conventional materials. The applications for CNTs range from heat sinks, thin films to thermal interface materials. However, when CNTs are grouped together in macroscopic quantities and embedded in different media their thermal conductivity changes. Therefore, it is important to determine the thermal conductance changes when CNTs are embedded in different media. In my research, CNTs were embedded in thin films and as aligned structures (fins) in water. Analytical and experimental methods were used to determine the thermal conductances of these aligned structures and thin films. The primary goals of this research were to develop novel analytical methods to determine thermal conductivity and also experimental techniques to determine effectiveness of the embedded CNTs as carriers of heat by thermal conductance evaluation. It is observed that CNTs fins are effective carriers of heat and result in up to 57% decrease in thermal resistance. In the case of CNTs embedded in thin films, it is important to consider non Fourier effects and neglecting non Fourier effects would lead to an underestimation of the thermal conductivity. In addition to the thermal conductivity value, the analysis also provides a way to determine the thermal relaxation time of thin films.

Acknowledgments

I would like to thank my co-advisors Dr. Yildiz Bayazitoglu and Dr. Enrique V. Barrera for giving me the opportunity to work on this amazing topic. I was given the flexibility, encouragement and the resources to work on many different projects. These projects provided me with gaining valuable analytical, experimental and numerical modelling experience. I also profoundly thank Dr. Thomas Killian for serving as a member on my dissertation committee.

I am thankful to my group members for their friendship and support. I would like to especially thank Jami Tullius for her valuable input. I am indebted to all my friends at Rice University for making my graduate student life enriching and pleasant. I am grateful to Daniel Hashim and Dr. Robert Vajtai from Dr. Pullickel Ajayan's group for providing me with the carbon nanotubes grown on silicon substrate. I would also like to thank Joe Gesenhues for his help with the experimental setup. A special thank you to my dear friend Gary Jarvis who made my life as a graduate student so much easier.

Finally, I would like to thank my parents for their blessings and for being patient and supportive throughout my graduate studies.

Contents

List of Figures

List of Tables

Chapter 1

Introduction

1.1. Motivation

Carbon nanotubes (CNTs) have superior thermal properties and have the potential to be used in many different applications ranging from heat sinks, thermal interface materials to heat sinks. The thermal conductivity of individual carbon nanotubes (SWNTs) has been experimentally measured to be up to 5800 W/mK [1] and for individual multiwalled carbon nanotubes (MWNTs) to be up to 3000 W/mK [2]. The thermal conductivity values change when the carbon nanotubes are grouped together in bulk – for MWNTs the measured value ranged from 4.1 – 150 W/mK [3, 4] and for SWNTs to 200 W/mK [5]. Potential applications of CNTs in heat sinks, thermal interface materials and thin films require that they be "embedded" as aligned structures in water or "embedded" in thin films. Therefore it is important to determine the thermal conductance/thermal conductivity in such cases. We would

like to mention here that we have used thermal conductance and thermal resistance interchangeably in this thesis. In addition thermal conductance and thermal conductivity are related and its relevance is based on the application considered. Thermal conductance is relevant when we consider heat sinks and thermal conductivity is important when we consider thin films and thermal interface materials.

1.2. Carbon Nanotubes

CNTs were first discovered by Ijima in 1991 [6] and have unique thermal, electrical and mechanical properties. Carbon nanotubes are part of the Fullerene structural family and can be considered to be a rolled-up 2D planar sheet of graphite (graphene). Their diameters usually range from 1 nm to 100 nm (hence the name carbon nanotubes) but can be up to microns in length. CNTs are synthesized at high temperatures using methods like carbon arc discharge, pulsed laser evaporation of graphite, thermal or plasma-assisted chemical vapor deposition and high pressure CO decomposition [7]. These synthesis methods yield good quality CNTs but the control over the chirality is rather limited. In addition these methods provide little control over defects in CNTs. Needless to say, synthesis of CNTs is one of the most fertile research areas, where a lot of issues still need to be addressed, if we envision CNTs to be used in real world applications.

1.2.1. Types of Carbon Nanotubes

The two main types of CNTs are single-walled nanotubes (SWNTs) and multi-walled nanotubes (MWNTs). MWNTs are basically made of concentrically placed SWNTs. The properties of SWNTs and MWNTs are quite similar due to the decoupling of SWNT rings in the MWNTs [8].

It is important to understand the geometry of a Graphene sheet to understand how the rolling of the sheet results in different types of SWNTs. Fig. 1.1 shows the vectors on a Graphene sheet. The point O denotes the origin and the other point A is any point that can be reached by the use of the chiral vector C_h. The vectors a_1 and a_2 are the primitive vectors of the unit cell. The chiral angle Θ is the angle the chiral vector makes with the zig zag axis of the Graphene sheet. The chiral vector can be formed from the primitive vectors using integers n and m such that

$$C_h = na_1 + ma_2 \tag{1.1}$$

Rolling the Graphene sheet where the point A coincides with origin O leads to a SWNT with (n,m) chirality. If we were to roll the sheet along the zig zag axis (i.e. Θ = 0) then we get a zig zag SWNT as show in Fig. 1.2a. We see that this corresponds to the m = 0 therefore all zig zag SWNTs are denoted by (n, 0) chirality. The armchair axis of the Graphene sheet is specified by $\Theta = \pi/6$ and this corresponds to n = m.

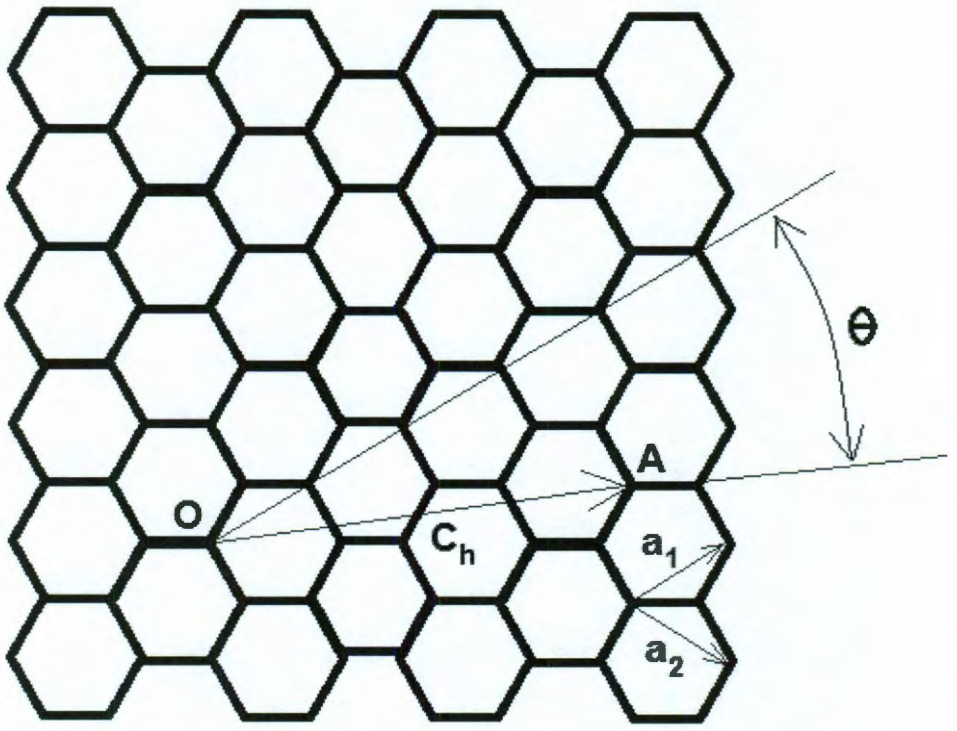

Figure 1.1: Schematic view of the vectors on a Graphene sheet.

Therefore, rolling the sheet along the armchair axis gives rise to the armchair SWNT denoted by (n,n) chirality as showing in Fig. 1.2b. A SWNT generated with any other Θ is known as a general SWNT and is denoted by the (n,m) chirality as shown in Fig. 1.2c.

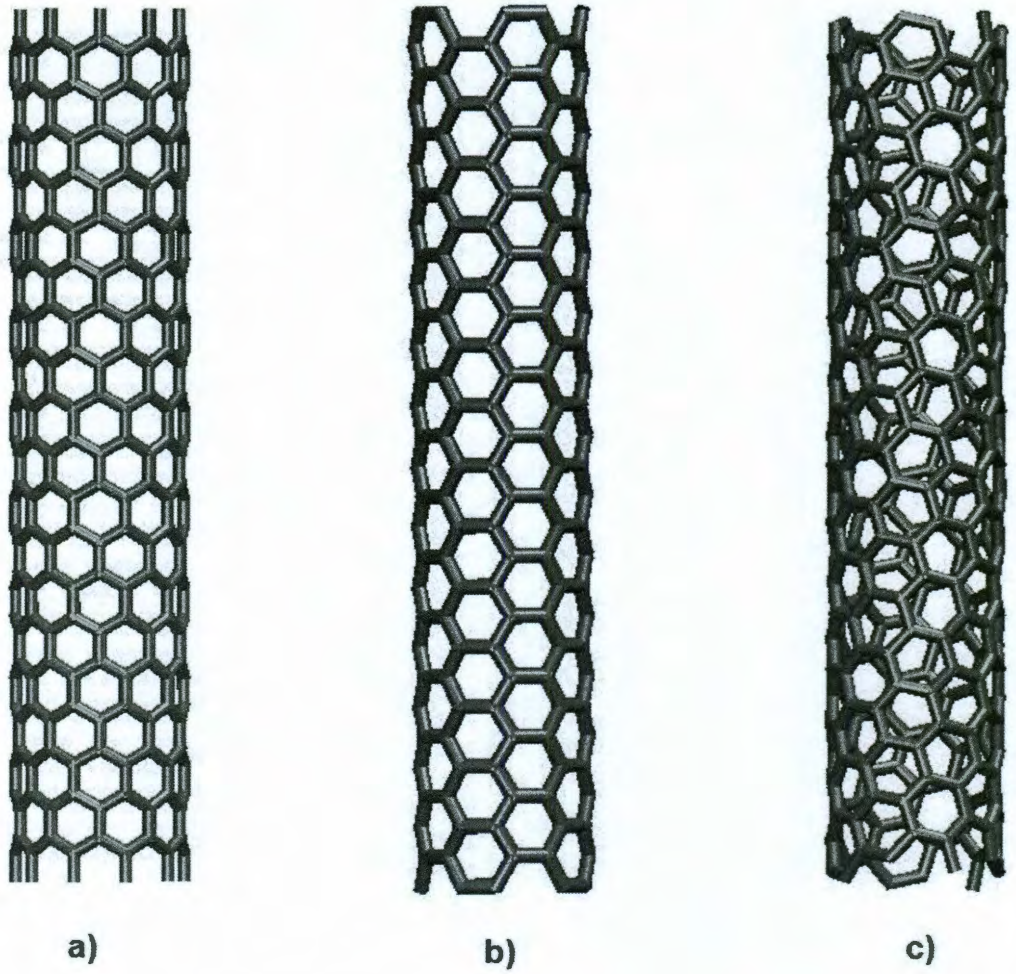

Figure 1.2: SWNT types based on chirality a) (10,0) zig zag SWNT b) (5,5) armchair SWNT c) (7,3) general SWNT.

The direction in which the Graphene sheet is rolled has an effect on the properties (including thermal) of the SWNTs. This gives rise to either metallic or semiconducting SWNTs and are defined by the formula,

$$r = (n - m) \bmod 3 \tag{1.2}$$

If r = 0, then the SWNT is metallic else it is semiconducting. Therefore the armchair SWNT is always metallic. For the semiconducting SWNT, the band gap depends on the diameter of the SWNT.

1.2.2. Thermal Properties

CNTs have excellent thermal properties owing to their strong sp^2 bonding. Carbon nanotubes have good temperature stability: up to 2800 ^{0}C in vacuum and 750 ^{0}C in air. This makes it better suited than metals in applications involving high temperatures since metals tend to get oxidized [9]. The thermal conductivity of CNTs along the axis is very high due to the 1D nature that leads to long phonon mean free paths. CNTs are interesting due to the fact that unlike metals where electrons carry both heat and electricity, in the case of CNTs the predominant carriers of heat are phonons [10].

The thermal conductivities of individual SWNTs and MWNTs was measured to be around 5800 W/mK and 3000 W/mK at room temperature as mentioned earlier. The thermal conductivity values change when measured in bulk. The thermal conductivity of disordered bulk SWNTs is around 35 W/mK [11] and for aligned bulk SWNTs it was measured to be 200 W/mK [5], while for bulk MWNTs the measured value ranged from 4.1 W/mK – 150 W/mK [3, 4]. The decrease in thermal conductivity suggests a weak coupling between the different CNTs [5]. The variability in the thermal conductivity values is attributed to the difference in synthesis methods and the experimental techniques used to measure the values.

Thermal conductance of bulk CNT structures have been found to be dependent on the interfacial properties of individual CNTs [12] and are also influenced by its diameter and structure [13]. In some cases thermal conductance values 2-3 times that of copper wires were observed. In general it was observed that the thermal conductance of SWNTs depends largely on its diameter and chirality whereas for MWNTs it depends on the tube diameter, length and number of shells [14]. Our literature search on thermal conductance of CNT structures in a fluid yielded no results.

1.3. Thermal conductance and thermal conductivity

Thermal conductance by definition is the quantity of heat passing in unit time through a plate of particular area and thickness when the plate's opposite faces are at a one degree temperature difference. It is a quantity that can be derived from the thermal conductivity and its unit is W/K. Unlike thermal conductivity, thermal conductance is dependent on the geometry of the structure. Thermal conductance or thermal conductivity is used in this thesis depending on the type of application considered. For applications like aligned structures of CNTs that are embedded in water, thermal conductance is of utmost importance, whereas for CNTs that are embedded in thin films the thermal conductivity is of importance. In the case of aligned CNT structures in water it is clear that the convective heat transfer into the water will depend on the geometry of the aligned structures thus making thermal conductance an important parameter. However, for thin films the conductive heat transfer is governed by thermal conductivity parameter and less by the geometry of

the thin fims. Therefore, in general we could say that for CNTs embedded in a fluid medium, thermal conductance is an important parameter whereas when CNTs are embedded in a solid medium then thermal conductivity is an important parameter.

1.3.1. Measurement techniques

1.3.1.1. Thermal conductance

One of the most simple and prevalent methods to determine the thermal conductance or resistance (reciprocal of conductance) of any structure that is embedded in a fluid is by adopting the heat sink methodology. The fluid can be considered to be air, water or any other type of fluid. The structures could be any material and in our case we consider CNTs. A heat sink facilitates the transfer of heat from the hot structure to the cold fluid. Tuckerman and Pease [15] were the first to characterize the performance of a heat sink using the total thermal resistance formula (R_{tot}) which they defined mathematically as

$$R_{tot} = \frac{T_w - T_{in}}{Q} \tag{1.3}$$

where T_w is the heat sink temperature, T_{in} is the inlet temperature of the fluid and Q is the heat dissipated by the heat sink. The total thermal resistance is independent of the heat dissipated but is dependent inversely on the flow rate of the fluid. The quantities in the Eq. (1.3) can be experimentally measured providing a simple way to measure the thermal resistance.

1.3.1.2. Thermal conductivity

The thermal conductivity measurement techniques for thin films have seen significant development in the last 20 years [16]. The measurement techniques can be divided into optical heating and sensing techniques and electrical heating and sensing techniques.

Optical heating and sensing techniques use laser irradiation to heat the thin films. Optical heating methods use the pump and probe lasers where the pump laser heats the thin film while the time delayed probe laser measures the temperature response of the thin film. Based on the response, the thermal diffusivity value is determined and then the thermal conductivity is calculated using a simple formula [17]. Therefore optical methods are sometimes called the indirect method to measure thermal conductivity. One of the disadvantages of optical heating methods is that it is difficult to determine the amount of heat absorbed by the thin films. Based on the measurement domain, optical techniques can be further divided into time domain techniques [18] and frequency domain techniques [19]. Time domain methods use the temporal decay of temperature in the thin film while the frequency domain methods use phase-sensitive lock-in techniques to measure the amplitude and phase of temperature in the thin film.

In electrical heating and sensing methods, the heating and sensing elements could be separate or in some methods the heater acts as a temperature sensor too. The advantage of the electrical sensing method is that it is easier to determine the amount of heat deposited on the thin film and the temperature rise. One of the most

commonly used methods to determine the thin film thermal conductivity is the 3 omega method [20]. 3 omega method offers the additional advantage that the measurement time is short (a few seconds) and the radiation losses are negligible since the thin film temperature rises only a few degrees above ambient.

Fig. 1.3 shows the schematic view of the 3ω measurement method. It consists of a metal line that acts as a heater/thermometer deposited onto the sample (thin film). If the resistance of the metal line is R_l and an alternating current (a.c) of ω frequency is passed through the metal line such that

$$I = I_o e^{i\omega t} \tag{1.4}$$

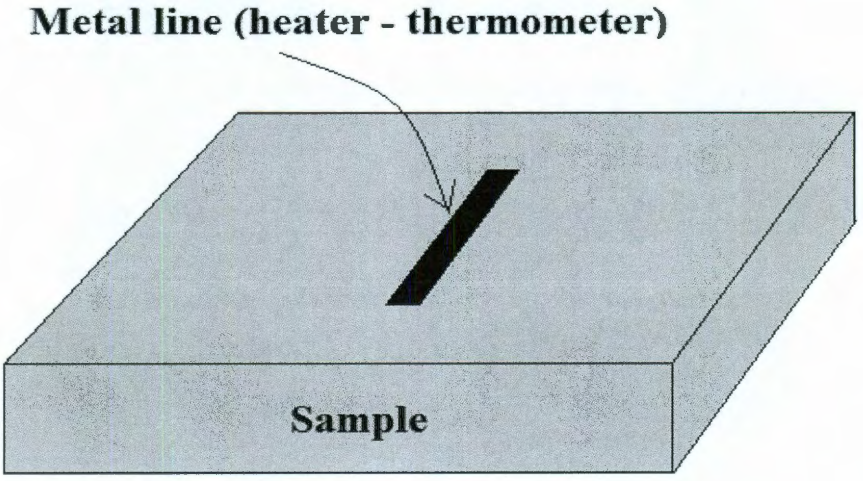

Figure 1.3: Schematic view of the 3ω measurement method

where I_o is the amplitude of the current. The current in the metal line leads to Joule heating Q at 2ω frequency

$$Q = I^2 R_l = (I_0)^2 e^{i2\omega t} R_l = P e^{i2\omega t} \tag{1.5}$$

where P is power generated in the metal line.

The Joule heating gives rise to temperature oscillations in the sample at 2ω frequency. Since the resistance of the metal line is linearly proportional to temperature, there is a small oscillatory component added to the metal line at 2ω frequency and the resistance of the metal line becomes

$$R = R_l + R_o e^{i2\omega t} \tag{1.6}$$

If we measure the voltage V across the metal line,

$$V = IR = I_o R_l e^{i\omega t} + I_o R_o e^{i3\omega t} = V_\omega + V_{3\omega} \tag{1.7}$$

we have an oscillatory component at ω frequency and also a small oscillatory component of voltage at 3ω frequency. Measuring the 3ω voltage yields the temperature oscillations data in the sample. The thermal conductivity value of the sample can be obtained by taking the slope of the in-phase temperature oscillations versus the heater frequency.

1.4. Non Fourier equation

Thermal conductivity measurement is predominantly governed by the Fourier equation. One of the drawbacks of the Fourier equation is that it assumes that heat travels at infinite speed [21]. At time scales that are sufficiently long like those encountered in most of the real world situations, the use of the Fourier equation is valid. However, when we consider very short time scales like those encountered in laser heating of materials and high speed electronics, the Fourier equation cannot be used. This is because in such cases local thermal equilibrium has not been achieved.

The 1D non Fourier equation (also known as the Cattaneo equation) and the associated hyperbolic heat conduction equation (HHCE) can be derived from the Boltzman transport equation (Appendix A),

$$\frac{\partial}{\partial x}\left(k(x)\frac{\partial v}{\partial x}\right)=\rho c_p\left(\frac{\partial v}{\partial t}+\tau\frac{\partial^2 v}{\partial t^2}\right) \tag{1.8}$$

where k is the thermal conductivity, ρ is the density, c_p is the specific heat and τ is the relaxation time. Clearly, we see that Eq. (1.8) shows that heat travels in the form of waves and has a finite speed c given by

$$c=\sqrt{\frac{k}{\rho c_p \tau}} \tag{1.9}$$

The 1D HHCE equation in cylindrical coordinates can be easily derived and is given by

$$\frac{1}{r}\frac{\partial}{\partial r}\left(k(r)r\frac{\partial v}{\partial r}\right)=\rho c_p\left(\frac{\partial v}{\partial t}+\tau\frac{\partial^2 v}{\partial t^2}\right) \tag{1.10}$$

If we assume k to be constant then Eq. 1.10 becomes

$$\tau\frac{\partial^2 v}{\partial t^2}+\frac{\partial v}{\partial t}=\alpha\left(\frac{\partial^2 v}{\partial r^2}+\frac{1}{r}\frac{\partial v}{\partial r}\right) \tag{1.11}$$

Chapter 2

Aligned structures of carbon nanotubes embedded in water

This chapter deals with an experimental study conducted to determine the thermal resistance of multiwall carbon nanotubes (MWNTs) grown in a silicon minichannel with water as the cooling medium. Two different devices based on different MWNT architectures – one fully covered with MWNTs and the other with 6 x 12 (rows, columns) of MWNT bundles were tested and compared to a device with no MWNTs. The performance was evaluated based on a constant heat flux applied to the silicon base versus the corresponding silicon base temperature. The experiments were performed at two different volumetric flow rates of 40 ml/min and 80 ml/min. The experimental results were also validated against computational modeling results. Finally, the thermal resistance of the three devices was calculated and compared. It was observed that the presence of MWNTs enhanced the heat removal from the silicon base.

2.1. Background

The next generation microchips with high power densities would require novel methods of cooling. Minichannels and microchannels provide an effective way of cooling microchips. The high heat fluxes can be dissipated using forced convection in microchannels and minichannels [15, 22-25]. Microchannels provide enhanced heat transfer ability when compared to minichannels due to having a smaller hydraulic diameter however they come with increased pumping requirement. In addition the fabrication of microchannels would require novel techniques that are time consuming and cost intensive. Several methods of altering the microchannels surfaces including rectangular grooves [26], offset fins [27] and longitudinal fins [28] have been investigated. All of them reported an increase in heat transfer due to increased surface area, better flow mixing, and an increased heat transfer coefficient but they also had the disadvantage of added pressure drop.

The working fluid investigated for liquid cooling has been predominantly water. In addition to the single phase heat transfer techniques mentioned above, flow boiling has also been investigated by several authors [29, 30]. Two phase flows provide high heat transfer coefficients when compared to single phase flows and are suited for high heat flux dissipation [31]. Nanofluids with water as the base fluid with various added nanoparticles offer several advantages for cooling. The thermal properties for these fluids can be tailored to suit the cooling requirements. Experimental investigations on convective heat transfer performance have been carried out using CuO [32, 33], Al_2O_3 [33-35], TiO_2 [36] and Cu [37] based

nanofluids. Nanofluids come with certain drawbacks like sedimentation, clogging of channels, erosion and increased pressure drop [38]. Dielectric fluids as the working fluid have also been investigated by various authors [39-41]. Dielectric fluids with their low boiling point and increased wetting properties provide an excellent way for increased heat transfer however they are plagued by dry out and reverse flow problems.

Numerous authors have investigated CNTs as thermal interface materials in microchannels for cooling. Flow boiling analysis with CNT coating in microchannels and water as the cooling medium has been reported by various authors [42, 43]. The authors claim an enhancement of critical heat flux owing to the fact that the CNT coating in microchannels provides numerous nucleation sites. Single phase cooling using CNTs with water as cooling medium on the other hand was researched by Mo et al [44]. They applied different heat rates to the base of the silicon microchannel while holding the pressure drop across the device constant. This was then compared to a silicon microchannel with no CNTs. They observed in the case of silicon microchannels with CNT fins, that they could apply 23% higher input power and still keep the temperature of the transistor lower than a silicon microchannel with no CNTs. Jakaboski et al [45] conducted further research on CNTs in silicon microchannels and achieved an increase in heat rate removal. Recently forced convection with water over single walled nanotubes was tested for different heat fluxes and flow rates [46]. Unlike previously reported, the results showed that single walled nanotubes result in no increase in heat dissipation but add a thermal resistance. The authors attributed this to the hydrophobic nature of the CNTs.

As far as we know, there is contradictory study on the enhancement of heat transfer using CNTs with water as the working fluid in single phase. In our research we have presented experimental results ranging from the single phase to the nucleation phase in the flow boiling regime. A comparison of the experimental results to the computationally modeled results was done and observed differences are explained. In general we found that the presence of MWNTs results in enhanced heat removal from the silicon minichannel.

2.2. Methodology

2.2.1. Device fabrication

Three different devices were fabricated – one with no MWNTs, one with fully covered MWNTs and one with a 6 x 12 array (6 rows and 12 columns) of MWNT bundles. The word bundles used in this thesis means bundles of MWNTs that form a cylindrical fin. Fig. 2.1 shows the basic steps involved in the fabrication of the three devices. We began with a 3" diameter, 1 mm thick silicon wafer that was diced using the Disco High Tech Scribe Saw into a 55 mm x 45 mm rectangular piece. To cut the octagonal hole in the center of the wafer, we first tried wet etching with potassium hydroxide [47] but we observed that it did not provide us with adequate dimensional control and the etching rate was too slow therefore we used laser cutting to cut the hole. The widest and longest part of the channel is 25 mm and 35 mm, respectively. Another 3" dia silicon wafer but 500 microns thick (pre-coated

with 500 nm silicon dioxide) was diced into a 55 mm x 45 mm rectangular piece. To bond the 1mm thick silicon wafer and the 500 microns thick silicon wafer, different

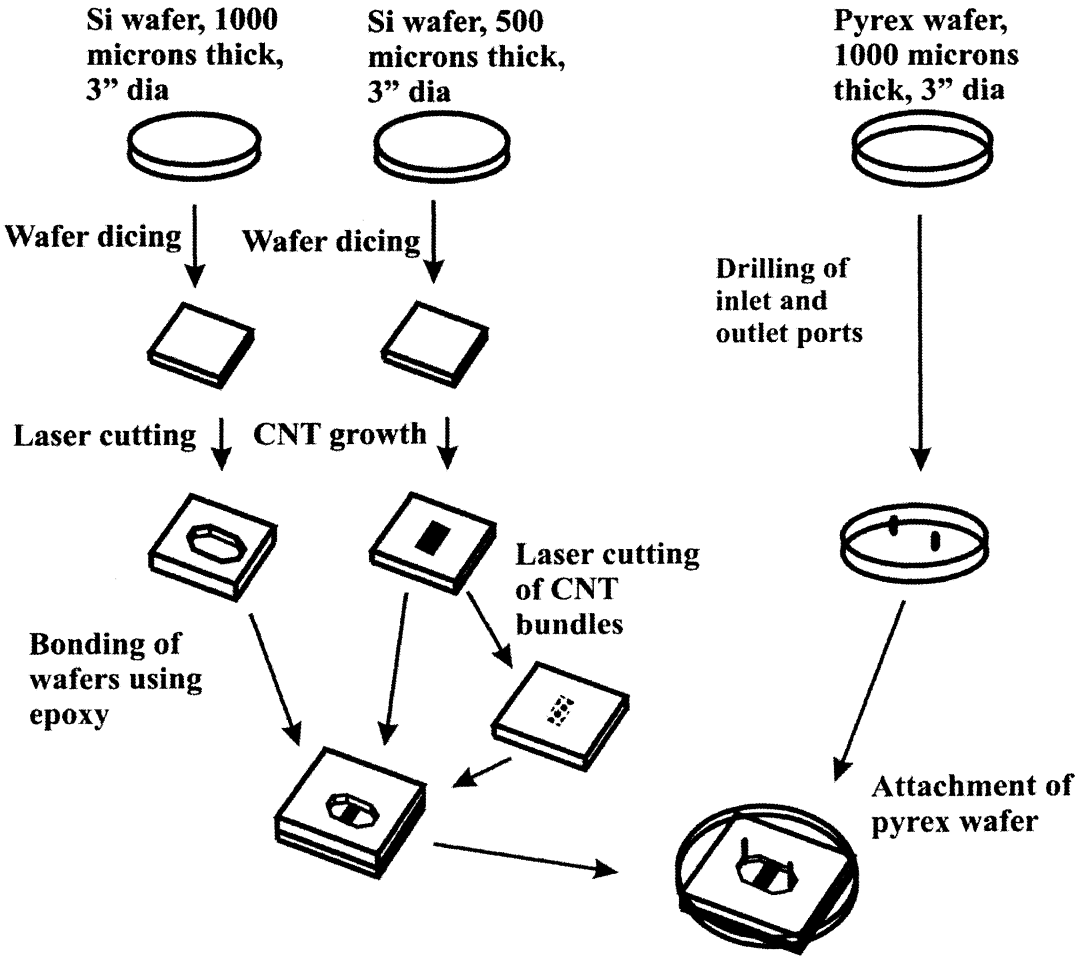

Figure 2.1: Steps showing the fabrication of MWNTs on silicon device.

methods were considered [48, 49] however we found that for our application, using an epoxy was the best option. It provided us with a quick, cost effective way to bond the wafers. We used the Devcon 2 Ton Epoxy that provided us with a work time of 30 minutes so as to provide us with ample time to correct alignment errors. To form the cover plate for the channel, we used a 3 " diameter, 1 mm thick Pyrex wafer with two holes for inlet and outlet of water. The two holes with 1.5 mm diameter were drilled at a distance of 31 mm from each other using a diamond tipped drill bit housed in a bench top drill press. Plastic capillary tubing of 1.5 mm outer diameter and 1 mm inner diameter was used then to form the inlet and outlet manifolds. The capillary tubing was attached to the Pyrex wafer using epoxy. The Pyrex wafer was then bonded on top of the silicon wafer assembly using an epoxy. This formed the base version i.e. the device with no MWNTs. The device and the channel dimensions are shown in Fig. 2.2.

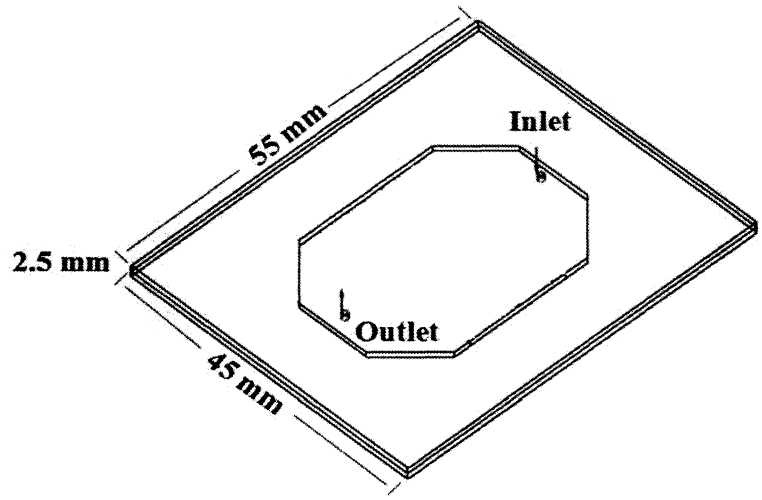

a)

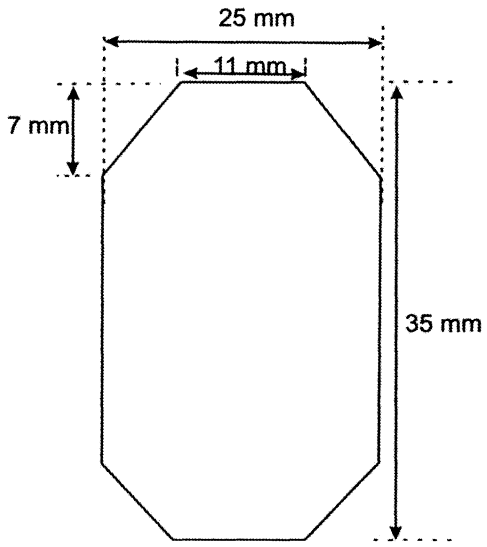

b)

Figure 2.2: Dimension of a) Device b) Octagonal Channel (1mm deep).

The fully covered MWNT device and the 6 x 12 MWNTs device were fabricated along the similar lines as the device with no MWNTs. The MWNTs were grown using chemical vapor deposition at 775 °C with a ferrocene catalyst and a xylene source with a mixture of argon and hydrogen as the carrier gas. The SEM image (Fig. 2.3) of the MWNTs shows a dense entangled network of tubes with a broad diameter distribution of 10 - 100 nm. In the case of the fully covered MWNT device, the 500 microns thick Si wafer had a rectangular area of 24 mm x 15 mm covered with MWNTs that was 500 microns in height in the center of the wafer. The 6 x 12 MWNT bundles were formed by laser cutting a fully covered MWNTs area. Fig. 2.4 shows an SEM image of a section of these bundles. The bundles are staggered in nature with a diameter of 1 mm and a height of 500 microns.

Raman spectroscopy of the 6 x 12 MWNTs device was done before and after laser cut. It was observed that the characteristic Raman spectrum (Fig. 2.5) of MWNTs remains the same i.e. the MWNTs remained intact. In between the bundles, we observed a peak at 512 cm^{-1} (Fig. 2.5c), which is the characteristic silicon peak, in addition to the characteristic MWNT peaks. We believe that in between the bundles there were regions where the silicon was exposed in addition to some residual MWNTs. We would like to point out here that the as grown MWNTs were hydrophobic in nature but we observed that the wetting properties of MWNTs changed towards hydrophilic once the fins were submerged in water over time. This change in wetting properties is an interesting phenomenon that requires further investigation since we were not able to find any explanation for this in the published literature.

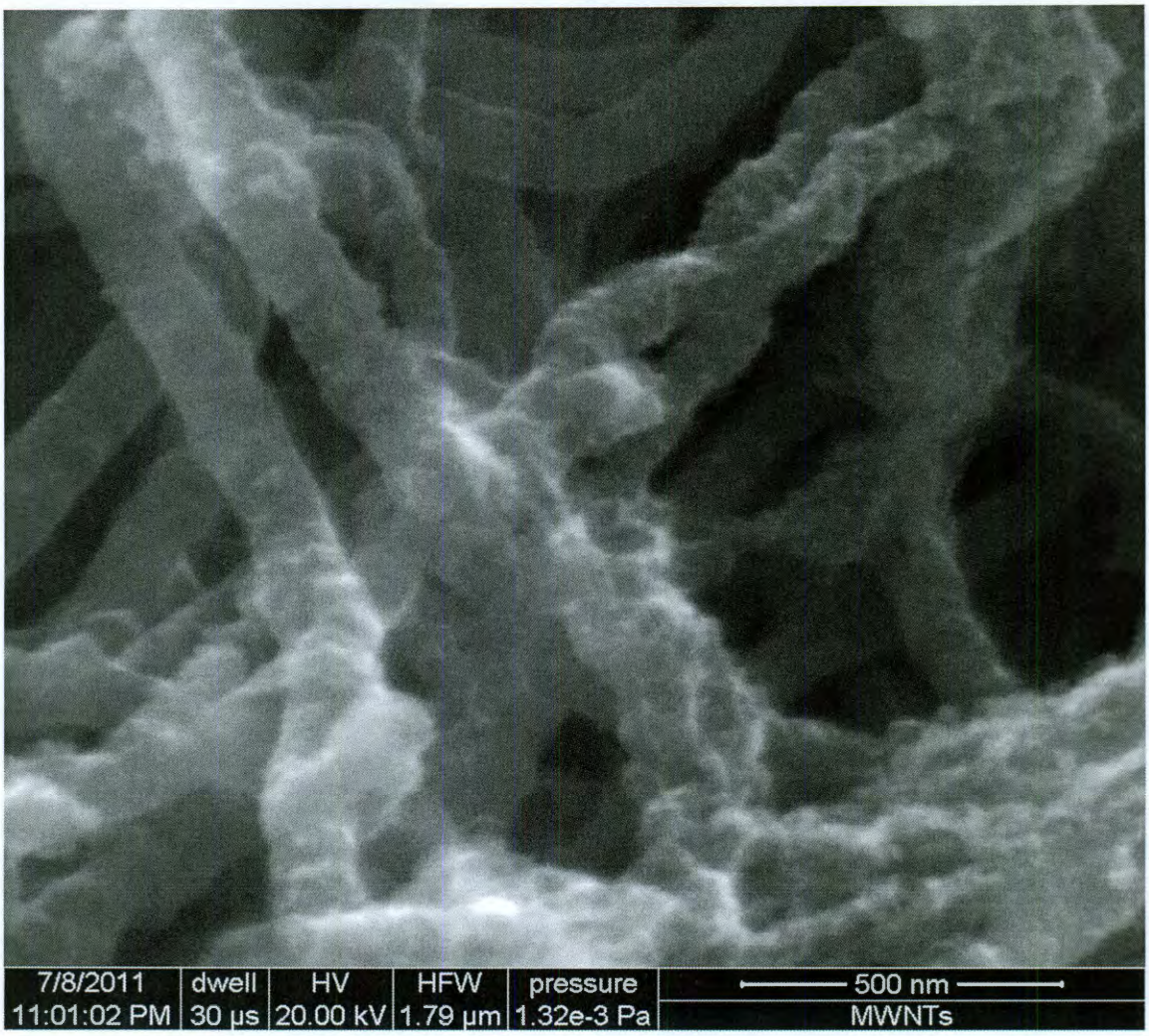

Figure 2.3: SEM image of MWNTs.

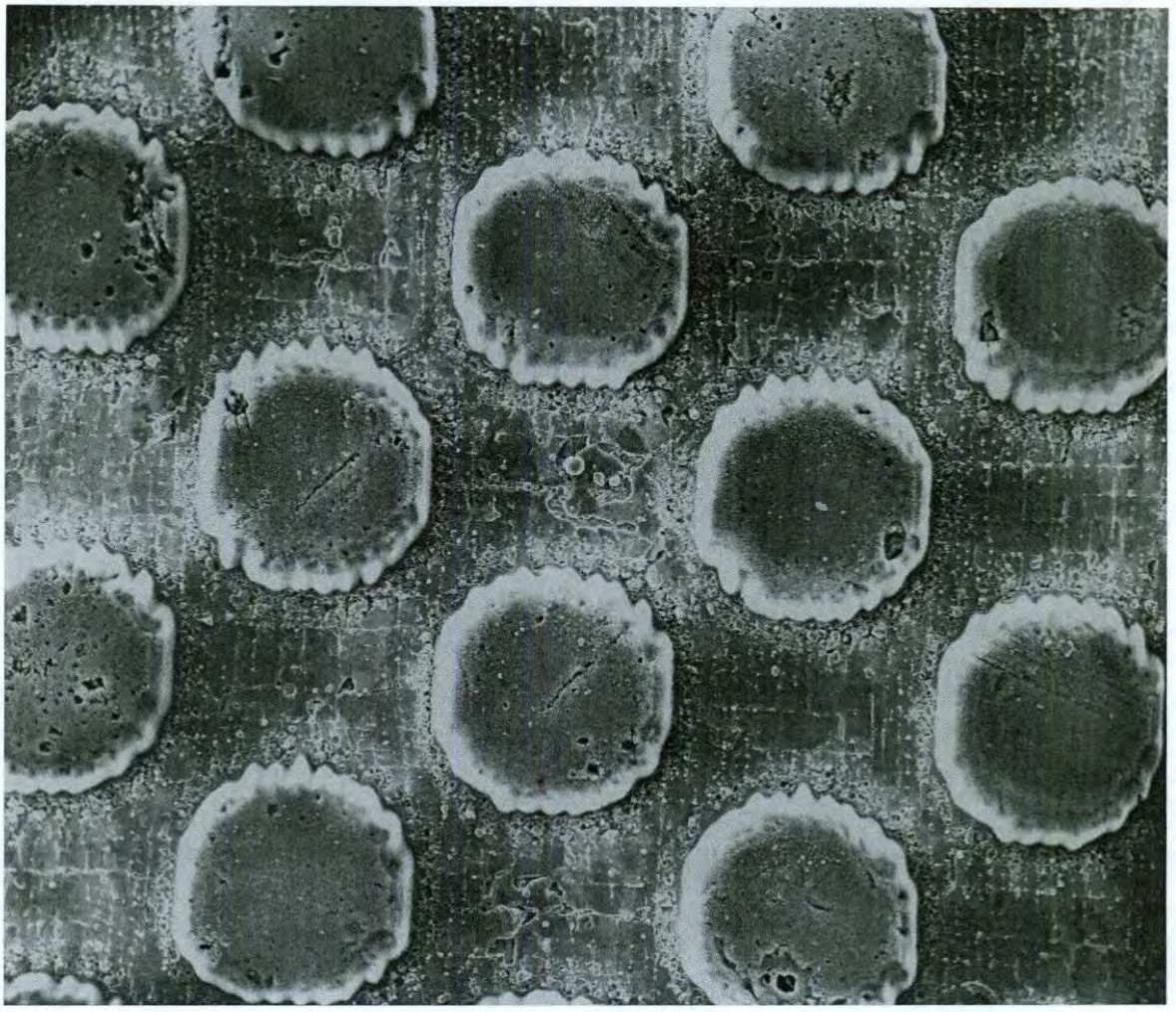

Figure 2.4: SEM image of MWNTs bundles as cylindrical columns.

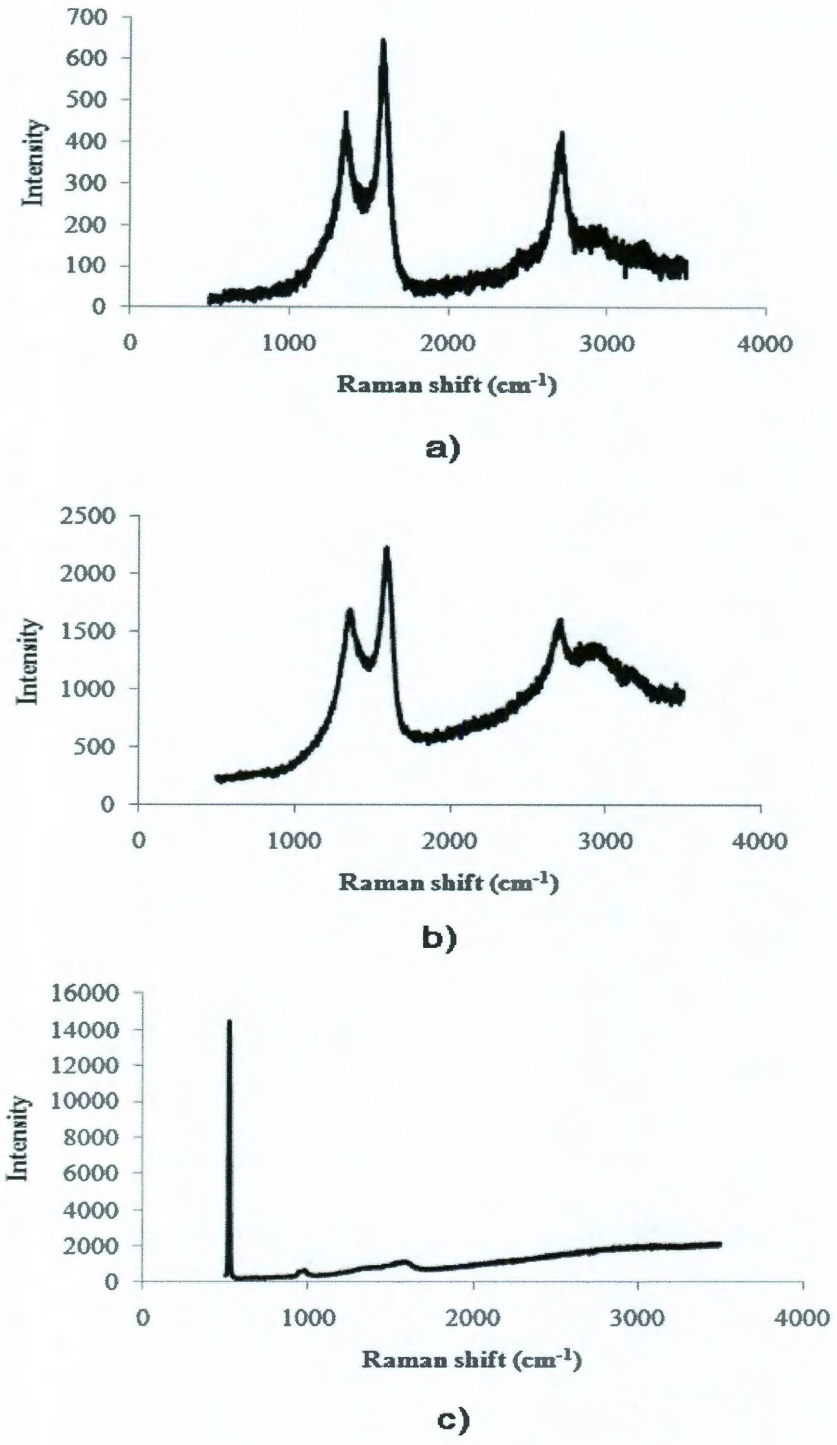

Figure 2.5: Raman spectra of the MWNTs. (a) Before laser cutting. (b) Bundles. (c) In between the bundles. The peak at 512 cm^{-1} shows that there is exposed silicon in addition to residual MWNTs.

2.2.2. Experimental setup

The experimental setup used to test the devices can be divided into two parts – flow loop and the test fixture. Fig. 2.6 shows the flow loop for water. De-ionized water is pumped through the setup using a Cole Parmer peristaltic pump. The peristaltic pump consists of a pump head and a drive to control the flow rate. A rotameter (ABB) flow meter is used to measure the volumetric flow rate of the water. The water then passes through the device holder that is used to hold the three devices to be tested and is finally collected in a beaker. A toggle valve (Swagelok) is provided to take care of unintended pressure build up in the flow loop

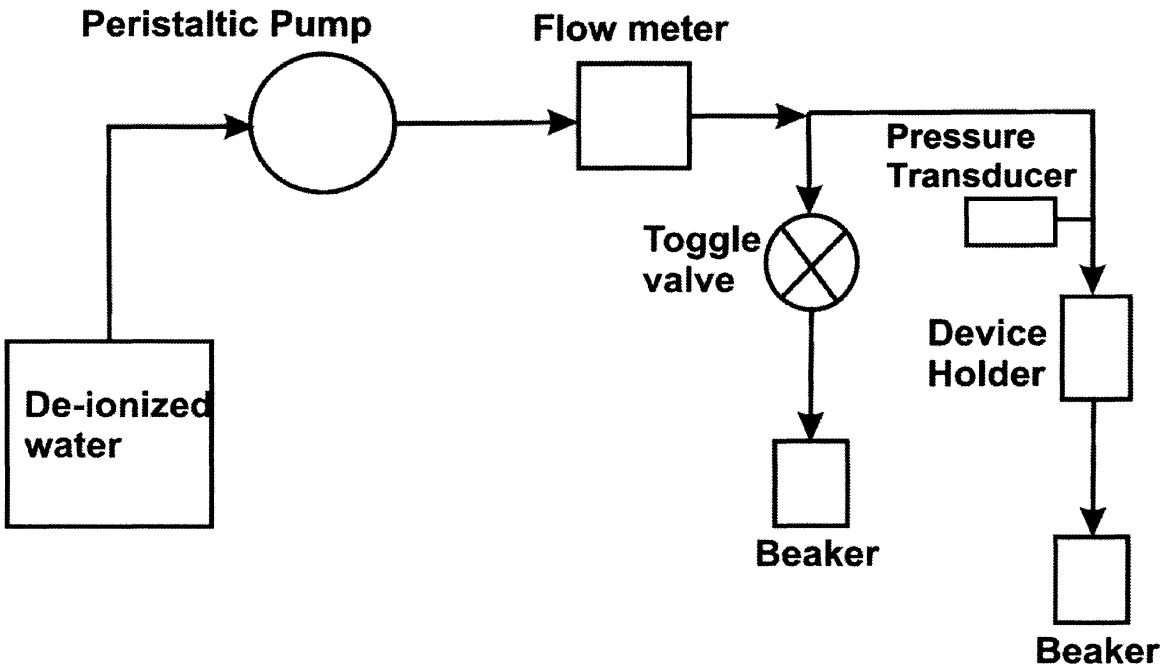

Figure 2.6: Flow loop for water.

due to obstructions. A differential pressure transducer (OMEGA PX-26-30 DV) is used to measure the pressure drop across the 3 devices. Since this is an open loop system, only one port of the transducer was connected to the inlet of the device. Since the outlet of the water was at atmospheric pressure, the pressure transducer provides the differential pressure. The differential pressure transducer was calibrated using a dead weight tester and a linear equation providing the pressure in Pascal from the corresponding voltage reading was obtained (Appendix B). In addition there were two thermocouples (not shown in the Fig. 2.6.) that were used to measure the inlet and outlet water temperature.

The test fixture that holds the devices to be tested is shown in Fig. 2.7. The device is held in the device holder made of fiberglass. The fiberglass has a 55 mm x 45 mm rectangular recess and in the middle of the recess is a 25 mm x 15 mm rectangular slot that houses a copper block. A Watson ceramic heater that is controlled by a variac heats the copper block that in turn heats the back surface of the silicon of the devices. Ceramic cloth insulation is used around the copper block to minimize heat loss. A thin layer of thermal interface material (Antec Formula 5) is applied to achieve good thermal contact between the copper block and the silicon surface. In addition, mechanical clamping was used to achieve a good thermal contact. Three holes drilled into the copper block are used to house Omega 30 gauge type T thermocouples. The thermocouples were anchored to the copper block using the Arctic Silver thermal epoxy. The thermocouples are used to measure the heat flux applied to the devices using Fourier's law.

$$q = k\frac{\Delta T}{\Delta x} \tag{2.1}$$

where Δx is the distance between the thermocouples, ΔT is the difference between the thermocouple temperatures and k is the thermal conductivity of the copper block. The top most thermocouple that is just below the silicon bottom surface is assumed to give the silicon surface temperature. The heater comes with an inbuilt thermocouple that provides a method to monitor the heater temperature. The data from the thermocouples and the differential pressure transducer was recorded using a data acquisition unit.

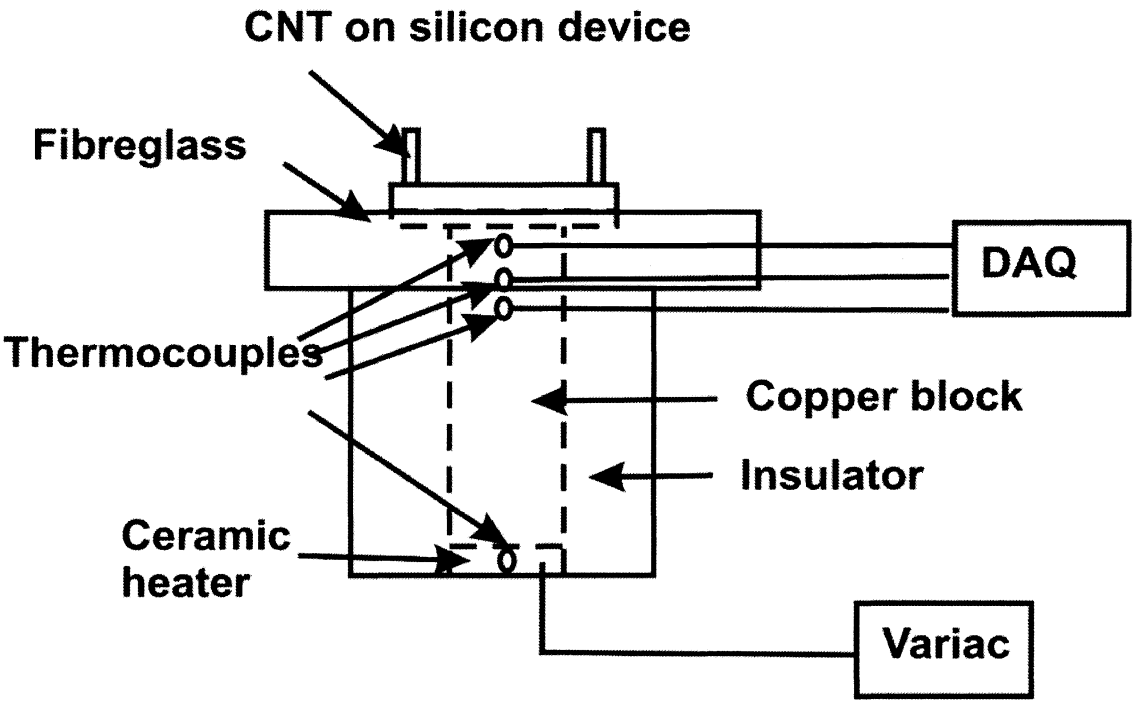

Figure 2.7: Test fixture.

2.3. Data acquisition

Data acquisition was performed using the Measurement Computing USB-TC-AI data acquisition unit. The data acquisition unit has 4 channels for thermocouples and 4 channels for voltage. The thermocouples are connected to the 4 channels while the output from the pressure transducer is connected to one of the voltage channels. The data from the data acquisition unit was displayed and recorded on a Dell desktop computer using the LabView 6.0 software. The LabView block diagram and the LabView front panel are shown in Fig. 2.8. The software begins displaying the data once the start timer is activated. The displayed data can then be either recorded on a text file or discarded by using the "save to file" button. The data displayed is written to a text file every 60 seconds when the "save to file" button is clicked. In the case of the pressure transducer, the software converts the voltage to an equivalent pressure drop using the linear calibration formula as obtained earlier. The software also records the four thermocouple readings. It used the silicon base, TC2 and the TC3 thermocouple data to calculate the heat flux values using the Fourier's law as explained in the previous section. The average heat flux was then obtained from the three heat flux values. The heat flux from the heater is also displayed using the software though we do not use it for any calculation purposes. In addition we also monitored the temperature of the ceramic heater through a thermocouple connected to a multimeter so as to ensure that the heater was within the operational temperature range.

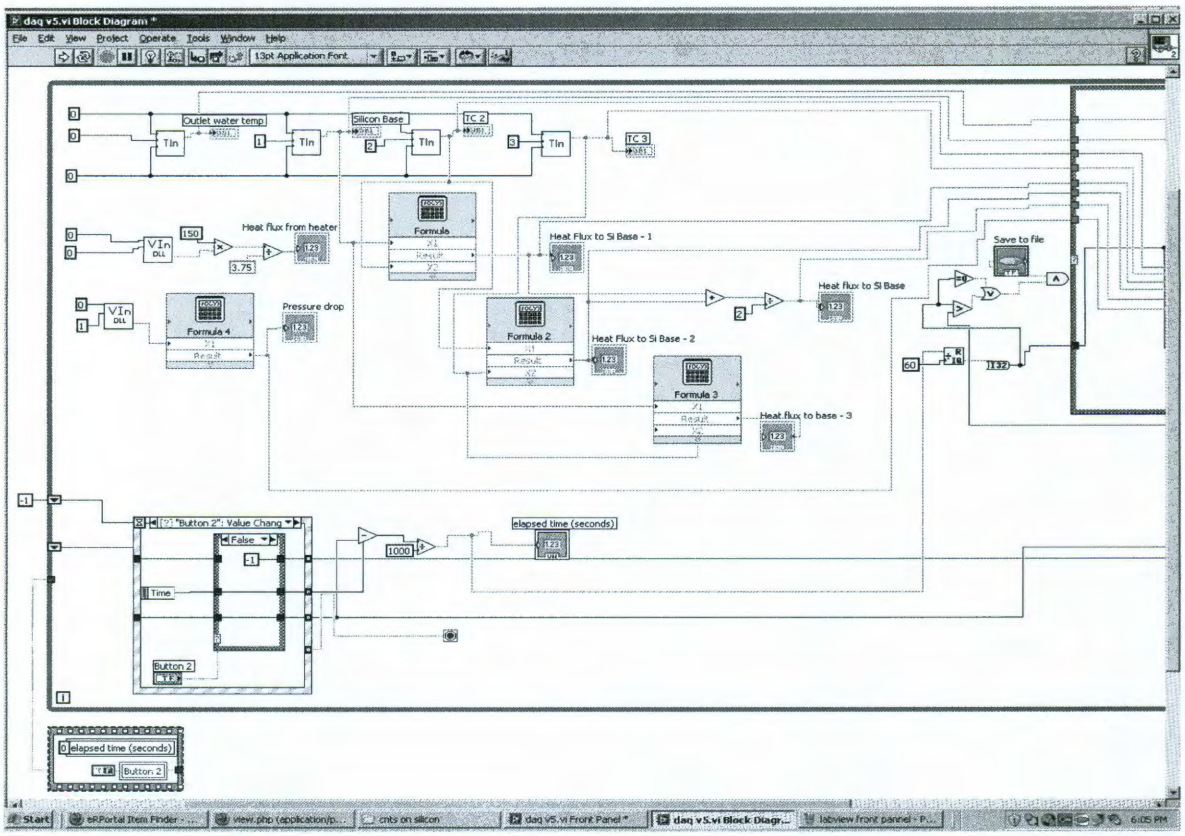

a)

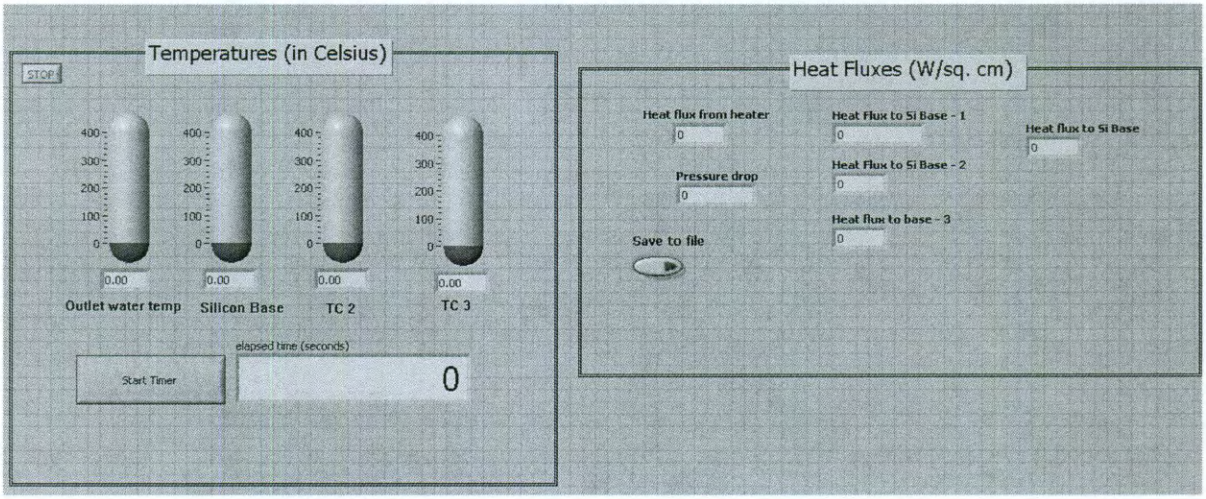

b)

Figure 2.8: LabView diagrams a) Block b) Front panel.

2.4. Data reduction and uncertainty

Uncertainties in measured quantities are 6% for the rotameter, 0.1 °C for the thermocouples and 7% for the pressure transducer. The heat loss was determined using computational modeling for the no MWNTs devices at different flow rates (Appendix C). The heat loss values obtained were then used to adjust the measured heat flux thus giving the heat flux applied to the base for the fully covered MWNTs devices and the 6 x 12 MWNTs device. The uncertainty (Appendix D) associated with the heat flux applied to the base was in the range of 3.6 - 17%, the uncertainties being higher at lower heat fluxes.

2.5. Results

2.5.1. Pressure drop analysis

The measured pressure drop measures not only the pressure drop across the channel but also includes the pressure drop across the norprene tubing, the inlet and outlet manifolds and the pressure drop due to contraction and expansion as the water enters through different tubing sizes as shown in Fig. 2.9.

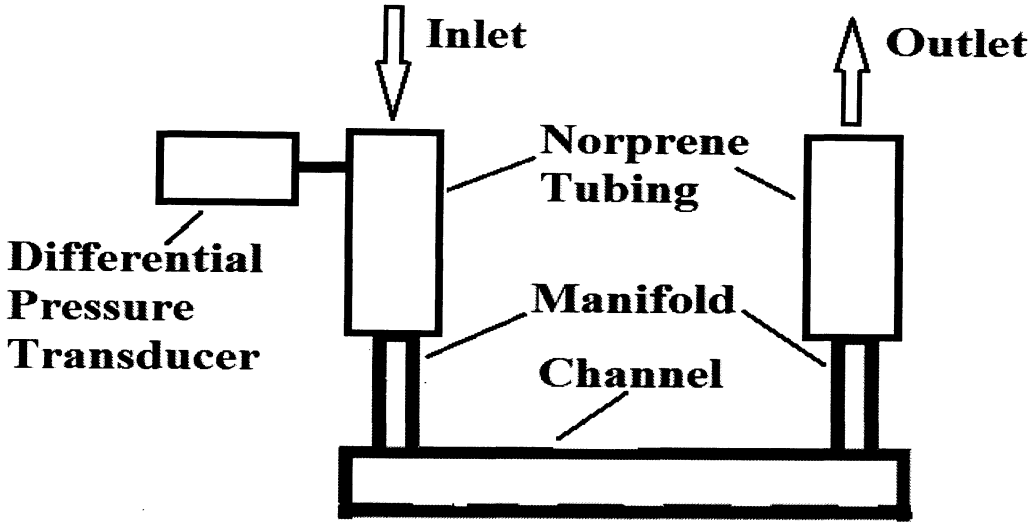

Figure 2.9: Pressure drop schematic

Therefore, the predicted pressure drop was determined by

$$\Delta P = \Delta P_m + \Delta P_n + \Delta P_c + \Delta P_e + \Delta P_{ch} \tag{2.2}$$

where ΔP_m and ΔP_n are the pressure drops across the manifolds and the norprene tubing. They are expressed using the Darcy Weisbach equation,

$$\Delta P_m = f \frac{L}{D_{hm}} \frac{\rho}{2} u_m^2 \tag{2.3}$$

and

$$\Delta P_n = f \frac{L}{D_{hn}} \frac{\rho}{2} u_n^2 \tag{2.4}$$

where u_m and u_n are the fluid velocities in the manifold and norprene tubing and ρ is the density of water.

ΔP_c is the pressure drop due to contraction as the water flows from the large norprene tubing into the inlet manifold tubing and ΔP_e is the pressure drop due to expansion as the water flows from the outlet manifold into the norprene tubing. They are expressed as [26]

$$\Delta P_c = \frac{\rho}{2}\left(u_m^2 - u_n^2\right) + \frac{k_c \rho u_m^2}{2} \tag{2.5}$$

and

$$\Delta P_e = \frac{\rho}{2}\left(u_n^2 - u_m^2\right) + \frac{k_e \rho u_n^2}{2} \tag{2.6}$$

The loss coefficients due to contraction (k_c) and expansion (k_e) are taken as unity. ΔP_{ch} is the pressure drop across the minichannel and is determined through computational modeling. Table 2.1 shows the values of the measured pressure drop and the predicted measure drop for single phase. We observe that the predicted pressure drop values and the measured pressure drop values are in good agreement with each other. The difference in two values was found to be within the measurement uncertainty calculated for the pressure transducer. For both flow rates, the fully covered MWNTs device caused higher pressure drops when compared to the no MWNTs device and 6 x 12 MWNT bundles devices.

Table 2.1: Single phase experimental and predicted pressure drops for the three devices.

Flow rate (ml/min)	Device	Pressure drop (kPa)	
		Predicted	Measured
40	No MWNTs	2.76	2.66
	Fully covered MWNTs	2.85	2.86
	6 x 12 MWNT bundles	2.78	2.76
80	No MWNTs	7.53	7.9
	Fully covered MWNTs	7.75	9.0
	6 x 12 MWNT bundles	7.56	8.05

2.5.2. Heat transfer analysis

The experimental and modeling results of the heat flux applied to the base versus the silicon base temperature for the three different devices are shown in Fig. 2.10. The CFD modeling results for the no MWNTs device are omitted since they have been used to calculate the heat loss values. The experimental results are an average plotted over 2 different runs for 40 ml/min and 80 ml/min volumetric flow rates. The plot shows the experimental results for both the single phase and boiling regimes. Since the modeling software was limited to single phase flows, the modeling results do not include the boiling regime. As clearly seen from the graphs, the devices with MWNTs perform much better than the device with no MWNTs in both regimes. It is seen that higher volumetric flow rates for each device results in higher heat transfer which means that a higher heat flux can be applied to the base while still keeping the silicon base temperature at a certain value. Table 2.2 provides the minimum heat fluxes for the different devices beyond which visible boiling starts to occur. For the 6 x 12 MWNT bundles device and the fully covered MWNTs device, surface area is much higher than the device with no MWNTs therefore more heat is removed. The system takes longer to reach the saturation temperature providing a higher heat flux before nucleation. No visible boiling was observed in the case of no MWNTs device.

Table 2.2: Heat flux data denoting the transition point from single phase to boiling.

Device	Flow rate (ml/min)	Heat flux (W/cm^2)
6 x 12 MWNT bundles	80	19.79
	40	18.93
Fully covered MWNTs	80	18.57
	40	17.25

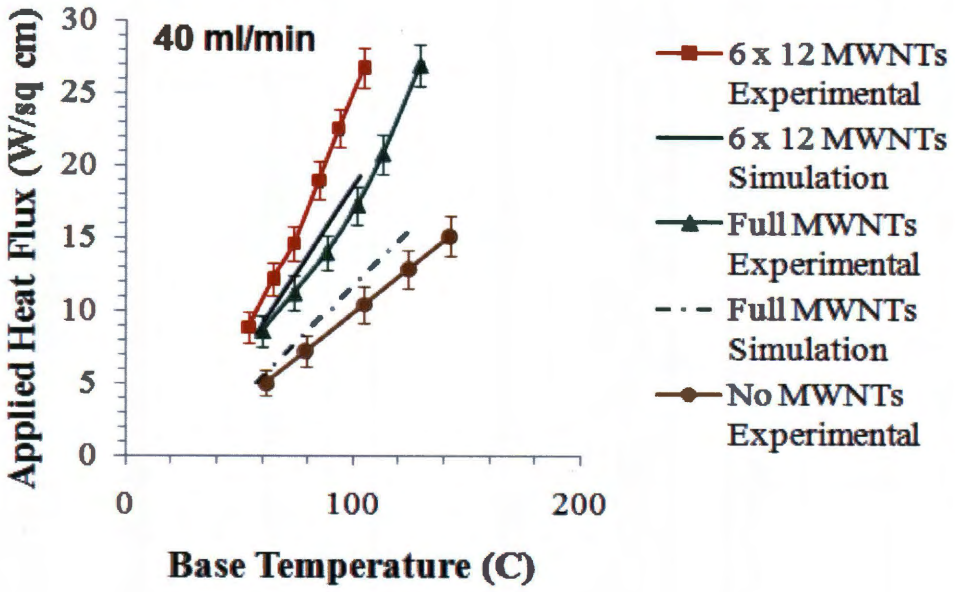

a)

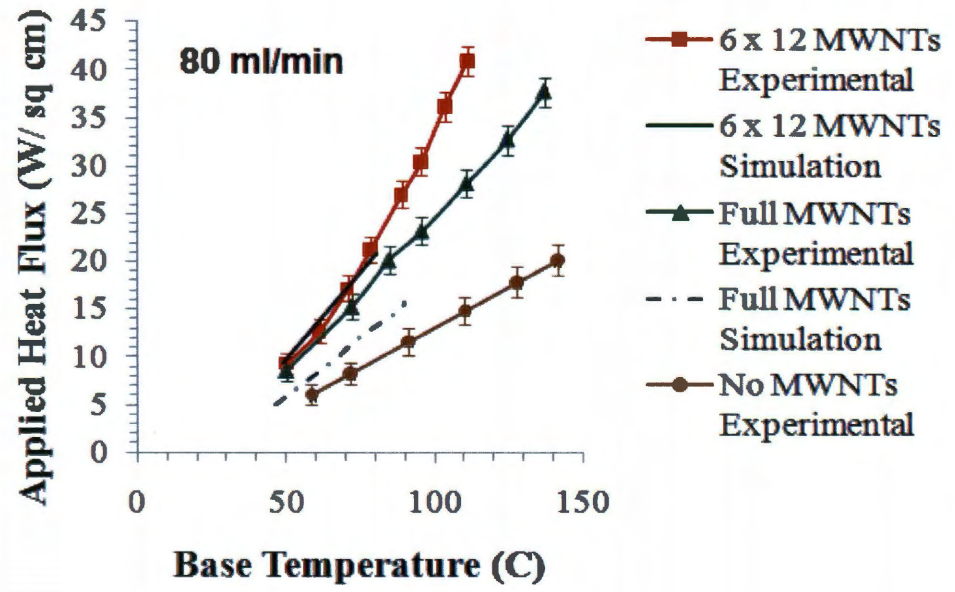

b)

Figure 2.10: Experimental and modeling results of heat flux applied to the base at different silicon base temperatures for: (a) 40 ml/min (b) 80 ml/min.

Fig. 2.11 shows the measured and predicted water temperature rise using the energy balance equation.

$$\rho V c_p (T_{out} - T_{in}) = Q \tag{2.7}$$

We have only considered heat flux ranges that keep the water in single phase. For both 40 ml/min and 80 ml/min, the measured water temperature rise and the predicted water temperature rise are reasonably close proving the validity of our heat loss calculations. As seen from Fig. 2.10, in the single phase regime, the devices with MWNTs perform much better. For a volumetric flow of 40 ml/min, one can apply only 6 W/cm^2 using no MWNTs device compared to 10 W/cm^2 using fully covered MWNTs device and 14 W/cm^2 using 6 x 12 MWNT bundles device while keeping the silicon base temperature at 70 °C. Using 80 ml/min flow rate and the same base temperature one can apply higher heat fluxes of 8 W/cm^2, 15 W/cm^2, 18 W/cm^2 using no MWNTs device, fully covered MWNTs device and 6 x 12 MWNT bundles device, respectively. For the fully covered MWNTs device, the decrease in hydraulic diameter, as seen from the increase in pressure drop, is the major factor for heat transfer enhancement. In the case of 6 x 12 MWNT bundles device, the enhancement could be due to a number of factors - predominantly it is due to the increase in surface area due to the bundles and also due to the decrease in hydraulic diameter as evident from the slight increase in the pressure drop. In addition to these factors, at higher temperatures there is significant wetting of the nanotubes by water [50] that might lead to increased heat transfer and is explained in detail later in the paper.

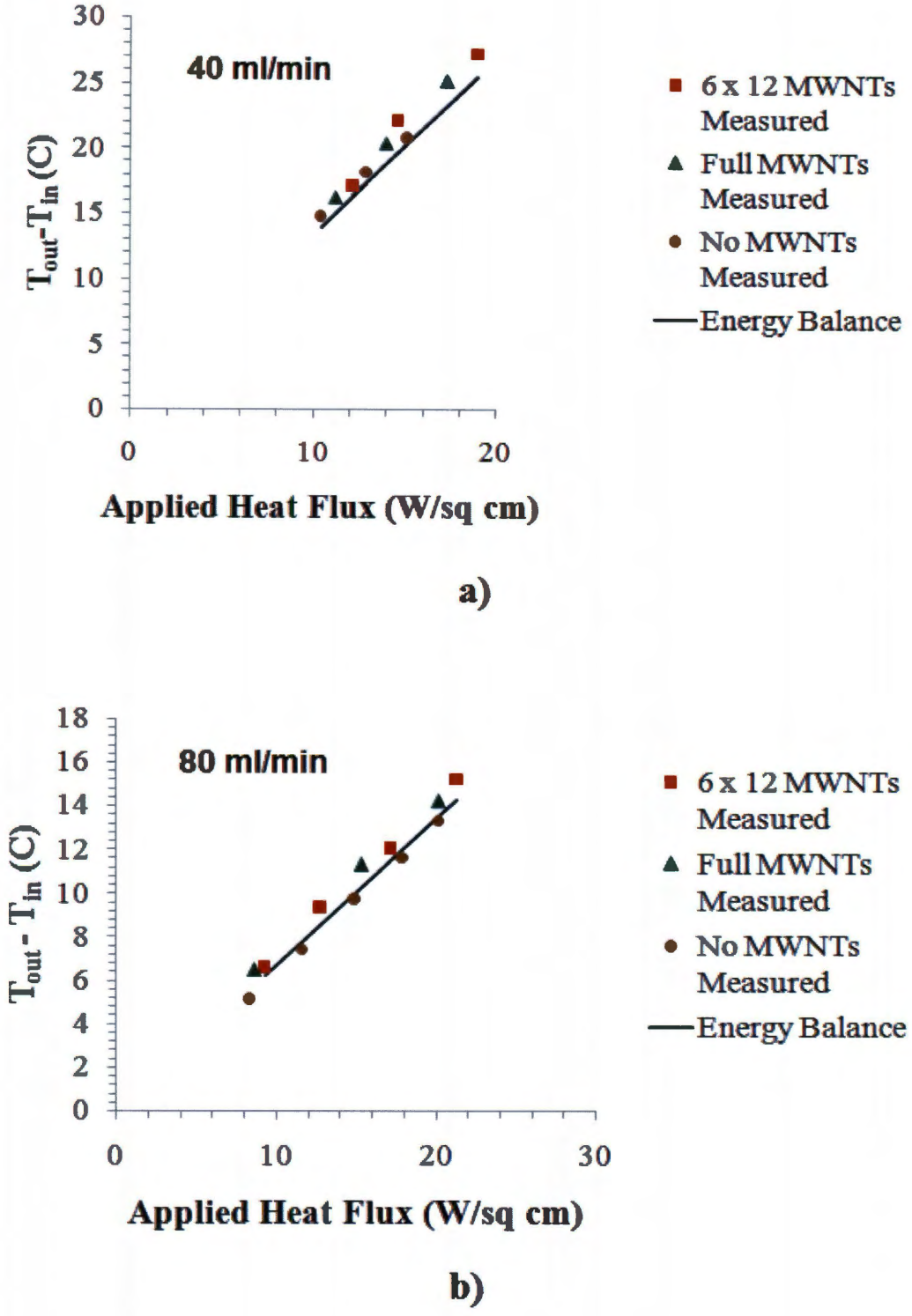

Figure 2.11: Measured water temperature rise and the predicted water temperature rise using energy balance for; (a) 40 ml/min (b) 80 ml/min.

The difference between the modeling results and the experimental results for fully covered MWNTs device for both 40 ml/min and 80 ml/min is significant as evident through Fig. 2.10. The measured pressure drop and the predicted pressure drop are in agreement therefore we cannot attribute this to the difference in hydraulic diameters. There are other factors that cause the significant difference in the modeling and experimental results. One of the main reasons could be that the model considers the fully covered MWNTs area as a solid block, whereas in reality, the fully covered MWNTs area has numerous hydrophilic MWNTs intertwined and entangled with nanoscale pores in between them allowing water to penetrate through the MWNTs. To illustrate further, the heat transfer coefficient obtained through modeling for 40 ml/min and 80 ml/min are 1649 $W/m^2.K$ and 2327 $W/m^2.K$. Using the heat transfer coefficients we can find the corresponding surface area available for heat transfer in experiments using Newton's law of cooling,

$$A = \frac{Q}{h(T_w - T_b)} \tag{2.8}$$

where T_w is the base temperature, T_b is the bulk fluid temperature, Q is heat supplied to the base and h is the heat transfer coefficient. For 40 ml/min using an experimental heat flux of 13.9510 W/cm^2 and a bulk fluid temperature of 32.17 °C, the surface area obtained was 36 % higher than the modeling surface area and for 80 ml/min using an experimental heat flux of 15.32 W/cm^2 and a bulk fluid temperature of 27.21 °C, the surface area obtained was 32 % higher than the modeling surface area. This ties in well with the amount of water absorbed by the carbon nanotubes versus the fluid temperature reported in [50]. It is also clear that

as the fluid temperature rises, there is increased wetting of the MWNTs which could lead to increased heat transfer. In the case of 6 x 12 MWNT bundles device the region occupied by MWNTs is much less than the fully covered MWNTs device and any increase in wetting would not cause a substantial increase in heat transfer. Therefore, the modeling results and the experimental results for both 40 ml/min and 80 ml/min are in reasonable agreement.

The three devices can be considered to be as heat sinks and one of the primary parameters to characterize a heat sink is its thermal resistance. The thermal resistance (R_{tot}) is given by [15]

$$R_{tot} = \frac{T_w - T_{in}}{Q} \tag{2.9}$$

where Q is the heat applied to the base, T_w is the base temperature and T_{in} is the inlet water temperature.

Fig. 2.12 gives the total thermal resistance for the 3 different devices at two different flow rates. Clearly, as the flow rate increases from 40 ml/min to 80 ml/min the total thermal resistance decreases due to increased convective heat transfer. For a particular flow rate, the fully covered MWNTs device had total thermal resistance that was 45% less when compared to the no MWNTs device. However, the fully covered MWNTs device did have a higher pressure drop. Similarly for the 6 x 12 MWNT bundles device, we obtained 57% decrease in the total thermal resistance when compared to a no MWNTs device. The pressure drop in this case was slightly

higher than the no MWNTs device. It is clearly seen that devices with MWNTs have a much lower thermal resistance when compared to the no MWNTs device.

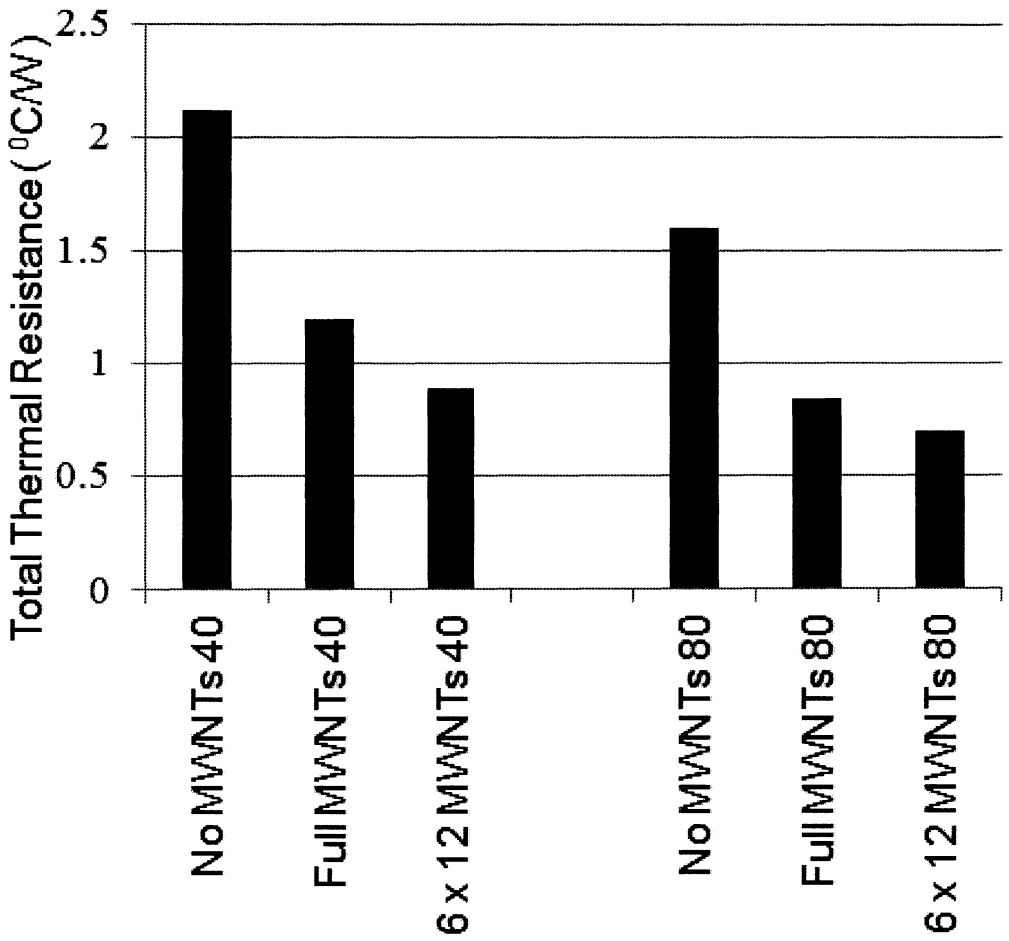

Figure 2.12: Total thermal resistance values for the three devices at two different flow rates.

Chapter 3

Non Fourier 3ω method for thermal conductivity measurement of thin films with embedded carbon nanotubes

The present chapter describes the 3-omega method for thermal conductivity measurement. Mathematical expressions for thermal conductivity using the hyperbolic heat conduction equation and the Fourier equation are derived for a Fourier boundary condition at the heat source. Mathematical conditions when non Fourier effects cannot be neglected are derived. Results are presented based on parameterized thermophysical properties. The hyperbolic heat conduction model is validated by comparing with the experimental results obtained by Cahill [20]. The hyperbolic heat conduction model is not only applied to a thin CNT composite film but is also applied to a biological material like bologna meat.

3.1. Background

The 3 ω method was originally developed to measure the thermal conductivity of dielectric solids [20]. It uses a thin metallic film that is deposited on the sample that acts as a heat source and thermometer. The metallic film is subjected to Joule heating and the governing Fourier equation is used to derive an integral for the steady state temperature oscillations arising in the sample due to a finite heater width. An approximate solution of this integral depicts a linear relationship between the heater frequency and the temperature oscillations thus providing a method for measuring the thermal conductivity of the sample. Lee et al [51] numerically integrated the integral in order to derive an expression for calculating the heat capacity of the sample. Subsequently the solution was extended to determine the thermal conductivity of thin dielectric films [52-54]. Raudzis et al [55] and Ahmed et al [56] have increased the heater frequencies well into the KHz and MHz regions making it possible to measure the thermal conductivity of thinner films than earlier possible. Recently, the method has also been used to measure the thermal conductivity of soft conductive substrates like polyaniline [57], CNTs [58] and thermoelectric materials [59]. The conventional 3ω method has a drawback that the method can be applied to determine the thin film conductivity only if the substrate and the thin film-substrate interface properties are known.

Fourier's law assumes that heat conduction occurs at infinite speed. While this works well in the macroscopic regime, this law breaks down at short time scales. Cattaneo [60] and Vernotte [61] modified the Fourier's heat conduction equation to incorporate the finite heat conduction speed by introducing a thermal relaxation time. The resulting equation is a hyperbolic heat conduction equation (HHCE) depicting the wave nature of heat. Joseph and Preziosi [21] provide an excellent review of the propagation of heat waves. The transient heat conduction through thin films has been studied using the application of the HHCE [62-64]. With regard to the application of HHCE to biological materials some authors [65, 66] have questioned its validity while others [67-70] have suggested that non Fourier effects exist and the heat conduction is primarily governed by HHCE.

Both Fourier's law and HHCE can be derived from the Boltzmann transport equation (BTE) by making certain assumptions. BTE describes the time evolution of a classical mechanical system in non equilibrium. It is more general in application than Fourier's law and HHCE. It is applicable across all heat transfer regimes including very short time and length scales where Fourier's law and HHCE are not valid. HHCE is derived from BTE by assuming local equilibrium and an average relaxation time. However, the solutions to HHCE have shown sharp wavefronts [71] that have invalidated these assumptions. In addition, HHCE also gives physically unreasonable results like negative absolute temperatures [72] and negative entropy generation violating the second law of thermodynamics [73]. Jou et al [74] later suggested that for non equilibrium thermodynamics phenomenon like hyperbolic heat conduction, the entropy generation is dependent on heat flux in addition to

classical thermodynamic variables thus resulting in positive entropy generation, justifying the validity of HHCE.

3.2. Physical model

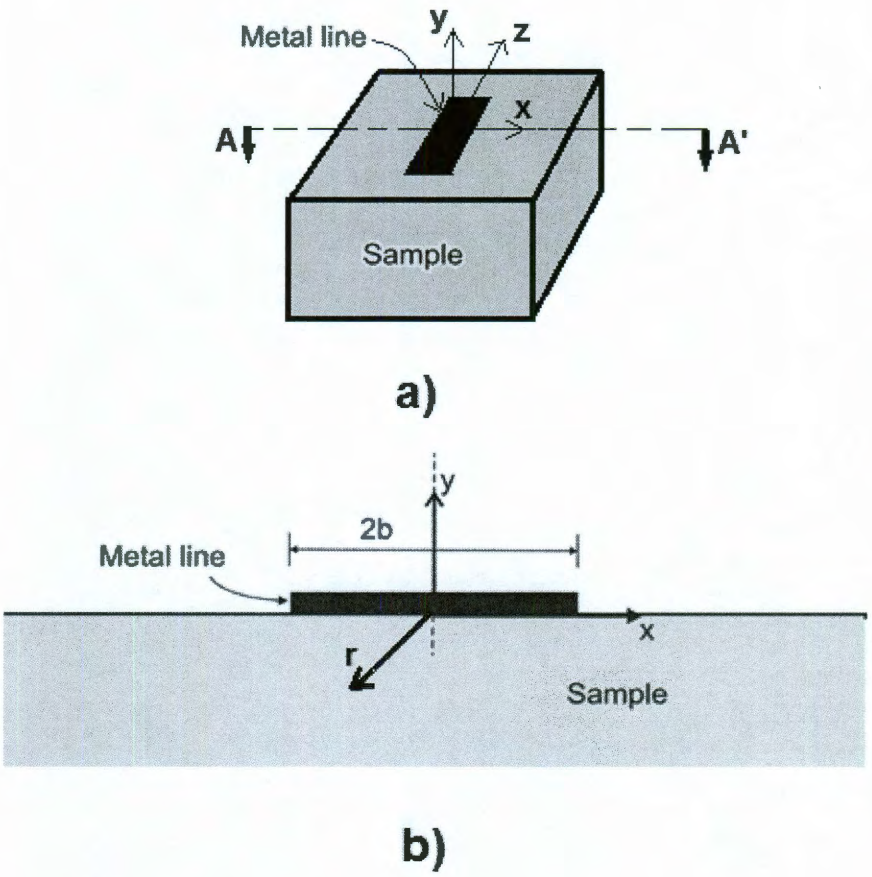

Figure 3.1: Schematic view of sample with the metal line a) 3 D view b) 2D view along section AA'.

Fig. 3.1 shows the schematic view of the sample on which a thin metallic film that acts as a heater/thermometer is deposited. The figure is not drawn to scale and

the sample thickness (semi infinite) is considered to be much larger than the metal line thickness and the edge effects are neglected. We assume that the sample thermal diffusivity (α) is known. The coordinate system is as shown in the figure with y being perpendicular to the surface of the sample, x being along the plane of the sample and the z axis being along the length of the metal line. The metal line has a length l and the width of the metal line is 2b. The quantity b is the half width of the metal line and is an important physical parameter in the analysis. The thickness of the metal line is assumed to be negligible and is not considered in the analysis. Though we are assuming a non conductive sample for our analysis we can consider a conductive sample by depositing a very thin passivation layer between the metal line and the sample.

3.3. Thermal model

The joule heating (P) produced by the alternating current at ω frequency in the metal line results in temperature oscillations at 2ω frequency in the sample. Since we are assuming a semi-infinite sample we can safely say that at sufficiently far away from the metal line, the temperature oscillations die down to the initial temperature v_i. We present a thermal model that considers the temperature oscillations travelling into the sample governed by Fourier equation and HHCE. In addition we also consider the boundary condition at the metal line to be a Fourier boundary condition where we first assume the metal line to be a line source and that all the heat is instantaneously deposited into the sample without any time lag.

After solving governing equation for a line source boundary condition we then consider the finite width of metal line and then modify the solution accordingly.

3.3.1 Hyperbolic heat conduction equation

The radial flow of heat from the thin metallic film into the sample with sets up temperature oscillations (v) which can be expressed by the following HHCE.

$$\tau \frac{\partial^2 v}{\partial t^2} + \frac{\partial v}{\partial t} = \alpha \left(\frac{\partial^2 v}{\partial r^2} + \frac{1}{r} \frac{\partial v}{\partial r} \right) \tag{3.1}$$

The boundary conditions are given by

$$Lim_{r \to 0} r \frac{\partial v}{\partial r} = -\frac{Pe^{i2\omega t}}{\pi kl} \tag{3.2a}$$

$$v(r = \infty, t > 0) = v_i \tag{3.2b}$$

$$v(r, t = 0) = v_i \tag{3.2c}$$

Using $T = v - v_i$, Eqs. (3.1)-(3.4) become

$$\tau \frac{\partial^2 T}{\partial t^2} + \frac{\partial T}{\partial t} = \alpha \left(\frac{\partial^2 T}{\partial r^2} + \frac{1}{r} \frac{\partial T}{\partial r} \right) \tag{3.3}$$

$$Lim_{r \to 0} r \frac{\partial T}{\partial r} = -\frac{Pe^{i2\omega t}}{\pi kl} \tag{3.4a}$$

$$T(r = \infty, t > 0) = 0 \tag{3.4b}$$

$$T(r, t = 0) = 0 \tag{3.4c}$$

The general solution of the steady periodic temperature oscillations at a distance r from the center line of the metal heater can be separated into a position component ($\Delta T(r)$) and a time component ($e^{i2\omega t}$) as shown below

$$T(r,t) = \Delta T(r) e^{i2\omega t} \tag{3.5}$$

Using Eq. (3.5), we can solve (Appendix E.1) the Eq. (3.3) subject to the boundary conditions given by Eqs. (3.4) to determine the amplitude of the steady state temperature oscillations in terms of modified bessel function (K_0) at a distance r in the sample.

$$\Delta T(r) = \frac{P}{\pi k l} K_0(qr) \tag{3.6}$$

with

$$q \equiv \left(\frac{i2\omega}{\alpha} - \frac{4\tau\omega^2}{\alpha} \right)^{1/2} \tag{3.7}$$

The magnitude of complex quantity 1/q gives the hyperbolic thermal wavelength of the thermal wave. It is a quantity that provides a means of knowing how far the oscillations have penetrated into the sample.

Since we are considering only the surface oscillations, we take y = 0 and Eq. (3.7) becomes

$$\Delta T(x) = \frac{P}{\pi k l} K_0(qx) \tag{3.8}$$

Eq. (3.7) is similar to the one obtained by Cahill [20] and accordingly the amplitude of temperature oscillations measured by a heater of finite width is obtained (Appendix F.1) as

$$\Delta T = \frac{P}{\pi k l}\int_0^{\infty} \frac{\sin^2(zb)}{(zb)^2 (z^2+q^2)^{1/2}}\, dz \tag{3.9}$$

For the condition where the hyperbolic thermal wavelength is much larger than the heater half width, $|qb| \ll 1$, the integral can approximated by the expression

$$\Delta T = \frac{P}{\pi k l}\int_0^{1/b} \frac{1}{(z^2+q^2)^{1/2}}\, dz \tag{3.10}$$

Eq. (3.10) can now be solved easily using standard integral transforms (Appendix G.1) to obtain the real and imaginary parts of the temperature oscillations

$$\Delta T = \mathrm{Re}(\Delta T) + i\,\mathrm{Im}(\Delta T) \tag{3.11}$$

where,

$$\mathrm{Re}(\Delta T) = \frac{P}{\pi k l}\left[\frac{1}{2}\ln\left((1+m)^2+n^2\right) - \frac{1}{2}\ln\omega - \frac{1}{4}\ln\left(4\tau^2\omega^2+1\right) - \frac{1}{4}\ln\frac{4b^4}{\alpha^2}\right] \tag{3.12}$$

$$\mathrm{Im}(\Delta T) = \frac{P}{\pi k l}\left[i\left(\tan^{-1}\left(\frac{n}{1+m}\right) - \frac{1}{2}\tan^{-1}\left(\frac{1}{-2\tau\omega}\right)\right)\right] \tag{3.13}$$

and,

$$m = \frac{1}{\sqrt{2}}\sqrt{1 - \frac{4\tau\omega^2 b^2}{\alpha} + \sqrt{\left(1 - \frac{4\tau\omega^2 b^2}{\alpha}\right)^2 + \frac{4\omega^2 b^4}{\alpha^2}}} \tag{3.14}$$

$$n = \frac{\omega b^2}{\alpha m} \tag{3.15}$$

$\mathrm{Re}(\Delta T)$ represents the in-phase oscillations and $\mathrm{Im}(\Delta T)$ represents the out-of-phase oscillations. The $\tan^{-1}$ in the above formulation represents the inverse tangent function.

From Eq. (3.12), we can consider two sets of conditions one in which non Fourier effects can be neglected and one in which non Fourier effects cannot be neglected. The first condition is given by,

$$\frac{\omega b^2}{\alpha} \ll \frac{1}{4} \quad and \quad \tau\omega < \frac{1}{2} \tag{3.16}$$

Consequently, $m \approx 1$ *and* $n \ll \frac{1}{4}$, reducing Eq. (3.12) to

$$\mathrm{Re}(\Delta T) = \frac{P}{\pi k l}\left[\ln(2) - \frac{1}{2}\ln\omega - \frac{1}{4}\ln\frac{4b^4}{\alpha^2}\right] \tag{3.17}$$

We see that the in-phase oscillations are linearly dependent on the log of the heater frequency and hence can be used to determine the thermal conductivity of the sample. This expression is similar to the one obtained by Lee et al [51] and is applicable in scenarios when non Fourier effects can be neglected.

$$k = -\frac{P}{2\pi k l}\frac{d(\ln\omega)}{d(\mathrm{Re}(\Delta T))} \tag{3.18}$$

The second condition is given by

$$\frac{\omega b^2}{\alpha} \ll \frac{1}{4} \quad and \quad \tau\omega > \frac{1}{2} \quad and \quad \frac{\tau\omega^2 b^2}{\alpha} \ll \frac{1}{4} \tag{3.19}$$

Consequently $m \approx 1$ *and* $n \ll \frac{1}{4}$, Eq. (3.12) reduces to

$$\mathrm{Re}(\Delta T) = \frac{P}{\pi k l}\left[\ln(2) - \ln\omega - \frac{1}{4}\ln(4\tau^2) - \frac{1}{4}\ln\frac{4b^4}{\alpha^2}\right] \tag{3.20}$$

Eq. (3.20) can be used to find the thermal conductivity of the sample when the non Fourier effects cannot be neglected however in this case we see that the expression for thermal conductivity differs from Eq. (3.18).

$$k = -\frac{P}{\pi l}\frac{d(\ln\omega)}{d(\mathrm{Re}(\Delta T))} \tag{3.21}$$

3.3.2 Fourier equation

Based on the physical model in Section 3.2, the temperature oscillations travelling into the sample can be expressed by the following Fourier equation in cylindrical coordinates.

$$\frac{\partial v}{\partial t} = \alpha\left(\frac{\partial^2 v}{\partial r^2} + \frac{1}{r}\frac{\partial v}{\partial r}\right) \tag{3.22}$$

The above equation is subject to the following boundary conditions.

$$Lim_{r\to 0} r\frac{\partial v}{\partial r} = -\frac{Pe^{i2\omega t}}{\pi k l} \tag{3.23a}$$

$$v(r=\infty, t>0)=v_i \tag{3.23b}$$

$$v(r,t=0)=v_i \tag{3.23c}$$

Using $T=v-v_i$, Eqs. (3.22)-(3.23) become

$$\frac{\partial T}{\partial t}=\alpha\left(\frac{\partial^2 T}{\partial r^2}+\frac{1}{r}\frac{\partial T}{\partial r}\right) \tag{3.24}$$

$$Lim_{r\to 0} r\frac{\partial T}{\partial r}=-\frac{Pe^{i2\omega t}}{\pi kl} \tag{3.25a}$$

$$T(r=\infty, t>0)=0 \tag{3.25b}$$

$$T(r,t=0)=0 \tag{3.25c}$$

The general solution of the steady periodic temperature oscillations at a distance r from the center line of the metal heater is given by

$$T(r,t)=\Delta T(r)e^{i2\omega t} \tag{3.26}$$

Eqs. (3.24) and (3.25) can now be solved (Appendix E.2) to determine the amplitude of the steady periodic temperature oscillations at a distance r in the sample.

$$\Delta T=\frac{P}{\pi kl}K_0(q_f r) \tag{3.27}$$

with

$$q_f \equiv \left(\frac{i2\omega}{\alpha}\right)^{1/2} \tag{3.28}$$

The magnitude of complex quantity $1/q_f$ gives the Fourier thermal wavelength of the thermal wave. As explained in Section 3.3.1 it provides a means of determining how far the thermal wave has penetrated into the sample. In general the Fourier thermal wavelength and the hyperbolic thermal wavelength would be similar in the macroscale but when we get into smaller and smaller sample sizes these two quantities will differ.

Considering only the surface oscillations with y = 0, we get

$$\Delta T(x) = \frac{P}{\pi kl} K_0(q_f x) \tag{3.29}$$

Eq. (3.29) can be modified to include the finite width of the heater (Appendix F.2) to give amplitude of temperature oscillations measured by the heater

$$\Delta T = \frac{P}{\pi kl} \int_0^{\infty} \frac{\sin^2(zb)}{(zb)^2 (z^2 + {q_f}^2)^{1/2}} dz \tag{3.30}$$

For the condition, $|q_f b| \ll 1$, the integral can approximated by the expression

$$\Delta T = \frac{P}{\pi kl} \int_0^{1/b} \frac{1}{(z^2 + {q_f}^2)^{1/2}} dz \tag{3.31}$$

Eq. (3.31) can now be solved (Appendix G.2) to obtain the real and imaginary parts of the temperature oscillations

$$\Delta T = \mathrm{Re}(\Delta T) + i\,\mathrm{Im}(\Delta T) \tag{3.32}$$

where,

$$\mathrm{Re}(\Delta T)=\frac{P}{\pi kl}\left[\frac{1}{2}\ln\left((1+m)^2+n^2\right)-\frac{1}{2}\ln\omega-\frac{1}{4}\ln\frac{4b^4}{\alpha^2}\right] \tag{3.33}$$

$$\mathrm{Im}(\Delta T)=\frac{P}{\pi kl}\left[i\left(\tan^{-1}\left(\frac{n}{1+m}\right)-\frac{\pi}{4}\right)\right] \tag{3.34}$$

and,

$$m=\frac{1}{\sqrt{2}}\sqrt{1+\sqrt{1+\frac{4\omega^2 b^4}{\alpha^2}}} \tag{3.35}$$

$$n=\frac{\omega b^2}{\alpha m} \tag{3.36}$$

$\mathrm{Re}(\Delta T)$ represents the in-phase oscillations and $\mathrm{Im}(\Delta T)$ represents the out-of-phase oscillations. It is evident that for the condition $\frac{\omega b^2}{\alpha}$ □ $\frac{1}{4}$ the Eq. (3.33) reduces to

$$\mathrm{Re}(\Delta T)=\frac{P}{\pi kl}\left[\ln(2)-\frac{1}{2}\ln\omega-\frac{1}{4}\ln\frac{4b^4}{\alpha^2}\right] \tag{3.37}$$

The Eq. (3.37) is assumed to be valid across both the Fourier and non Fourier regimes unlike the scenario considered with the hyperbolic heat conduction equation. We see that the in-phase oscillations are linearly dependent on the log of the heater frequency and hence can be used to determine the thermal conductivity of the sample.

$$k=-\frac{P}{2\pi kl}\frac{d(\ln\omega)}{d\left(\mathrm{Re}(\Delta T)\right)} \tag{3.38}$$

3.4. Thermophysical data

The relaxation time and the thermal diffusivity constitute some of the important thermophysical data required in our analysis. The thermal diffusivity values are readily available in literature however the relaxation time needs to be calculated or experimentally determined. The definition of the relaxation time (τ) varies for homogeneous and nonhomogeneous materials. For homogeneous materials it is the time lag between when the temperature gradient is applied and when the heat flow commences. For nonhomogeneous materials, it is the time required to accumulate the energy required to propagate it to next element [67]. Tentatively, the relaxation time can give a reasonable idea as to when one can neglect non Fourier effects and when one cannot.

For homogeneous materials like dielectrics, the heat transfer is predominantly through phonons. The phonon relaxation time can be calculated using the thermal diffusivity (α) and speed of sound in the material (c_s) [75].

$$\tau = \frac{3\alpha}{c_s^{\,2}} \tag{3.39}$$

However, for nonhomogeneous materials like biological tissues there is no mathematical expression available for calculating the relaxation time and one has to resort to experimental methods to determine its value. Table 3.1 lists the thermophysical data for dielectrics at low temperatures (100 K) and room

Table 3.1: Thermophysical data and the relaxation time used for dielectrics and tissues.

Material	Temp (K)	$k\ (W/m.K)$	$\rho\ (kg/m^3)$	$c_p\ (J/kg.K)$	$\alpha\ (m^2/s)$	$c_s\ (m/s)$	τ (s)
CVD Diamond	100	4000	$3.51*10^3$	$0.2*10^2$	$5.56*10^{-2}$	18000	$5.14*10^{-10}$
Boron Nitride (cubic)	100	1300	$3.4*10^3$	$0.04*10^3$	$9.56*10^{-3}$	14000	$1.46*10^{-10}$
Silicon Carbide	100	400	$3.31*10^3$	$0.3*10^3$	$4.02*10^{-4}$	11820	$8.65*10^{-12}$
Pyrex	100	0.6			$9.0*10^{-7}$	5900	$7.75*10^{-14}$
CVD Diamond	300	2000	$3.4*10^3$	$0.52*10^3$	$1.14*10^{-3}$	18000	$1.06*10^{-11}$
Boron Nitride (cubic)	300	1300	$3.4*10^3$	$0.63*10^3$	$6.11*10^{-4}$	14000	$9.36*10^{-12}$
Silicon Carbide	300	200	$3.31*1*10^3$	10^3	$6.04*10^{-5}$	11820	$1.29*10^{-12}$
Pyrex	300	1			$7.0*10^{-7}$	5900	$6.60*10^{-14}$
Silicon dioxide	300	1.35			$8.3*10^{-7}$	5900	$7.15*10^{-14}$
Bologna meat	300	0.8			$1.4*10^{-7}$		16

Taken from Refs. [68, 76-81]

temperature including the relaxation times calculated using Eq. (3.39). We see that there is a dependency of the relaxation time on the thermal diffusivity. As the thermal diffusivity increases, the relaxation time also proportionally increases. Infact this can be used to parameterize the thermophysical data for dielectrics. The room temperature values of the thermophysical data for bologna meat are also provided.

In 3ω method, the size of the dielectric film and its thermal diffusivity determines the heater frequency. For sub micron thin films like CVD diamond and CNTs that have high thermal diffusivity, we need to use heater frequencies in the MHz regime. The period of resulting temperature oscillations in the film is comparable to the phonon relaxation time making the consideration of non Fourier effects important. The phonon relaxation time is temperature dependent. For dielectrics it is as high as 10^{-10} secs at 100 K and decreases as the temperature increases. Therefore non Fourier effects will play an important role in dielectric films with high thermal diffusivity at low temperatures where the phonon relaxation time is high. Similarly in the case of biological materials like bologna meat that have relaxation time in tens of seconds at room temperature, we can assume that one will have to consider non Fourier effects while calculating the thermal conductivity.

3.5. Results

A matlab code was written to integrate Eq. (3.9) and Eq. (3.30) for different thermophysical parameters available through Table 1. Fig. 3.2 shows the in-phase temperature oscillations for three different sets of $\omega b^2/\alpha$. For all the three sets, $\tau\omega^2 b^2/\alpha \square 1/4$. We see that beyond the $\tau\omega = 1/2$ line the HHCE solution differs significantly from the Fourier solution, in agreement with the conditions formulated

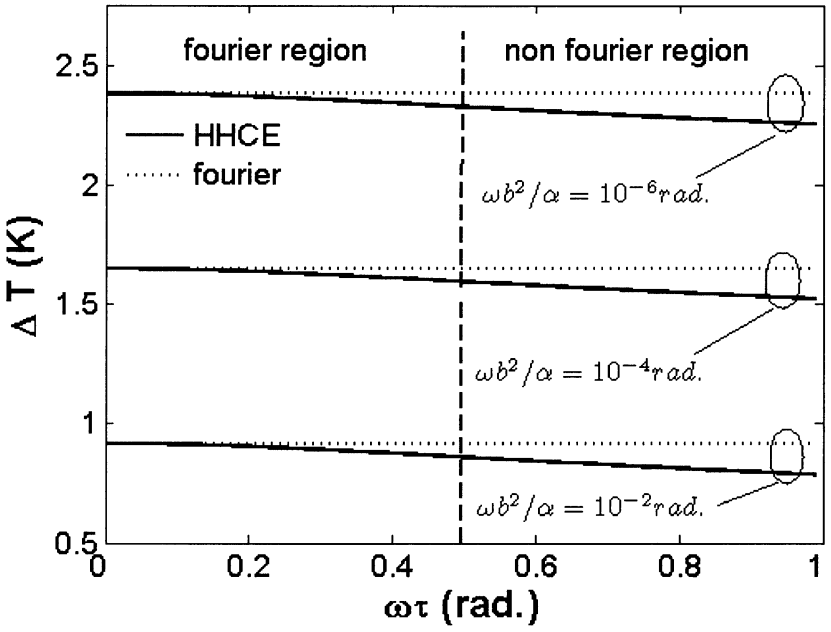

Figure 3.2: In-phase temperature oscillations measured using Eq. (3.9) and Eq. (3.30). The vertical dotted line at $\tau\omega = 1/2$ acts as a demarcation for Fourier and non Fourier effects when using hyperbolic heat conduction equation.

by Eq. (3.16) and Eq. (3.19). As mentioned previously the thermal diffusivity and the relaxation time for dielectrics are related and can be parameterized into four cases:

$$case\ 1 \rightarrow \alpha = 10^{-1}\ {}^{m^2}\!/_{s} : \tau = 10^{-9}\ s,$$
$$case\ 2 \rightarrow \alpha = 10^{-2}\ {}^{m^2}\!/_{s} : \tau = 10^{-10}\ s,$$
$$case\ 3 \rightarrow \alpha = 10^{-3}\ {}^{m^2}\!/_{s} : \tau = 10^{-11}\ s,$$
$$case\ 4 \rightarrow \alpha = 10^{-6}\ {}^{m^2}\!/_{s} : \tau = 10^{-13}\ s$$

These four cases span the data from CVD Diamond to Pyrex for different temperatures. Fig. 3.3 shows the in-phase temperature oscillations obtained by solving Eq. (3.9) and Eq. (3.30) using a metal line half-width of $1\mu m$ for the different cases and we limit the frequency to the MHz regime. The frequency cutoff for each case is determined by the $|qb| < 1$ condition which limits the frequency to 793 MHz, 625 MHz and 79 MHz respectively. The cutoff frequency for case 4 is below MHz so its results have not been shown in Fig 3.2. In any case for values of thermal diffusivity and relaxation time lesser than those of case 3, the Fourier and HHCE solutions will not differ. For all the cases the condition ${}^{\omega b^2}\!/_{\alpha} \square\ 1/4$ *and* ${}^{\tau\omega^2 b^2}\!/_{\alpha} \square\ 1/4$ is satisfied.

For high thermal diffusivity and high relaxation time, cases 1 and 2, we observe a marked difference between the solutions obtained by using Fourier and HHCE. The error in the solutions predicted can be as high as 150% for case 1 as

shown in Fig. 3.4. The error value is the percentage deviation of the Fourier solution from the HHCE solution.

$$\%Error = \left(\frac{\Delta T_{fourier} - \Delta T_{HHCE}}{\Delta T_{HHCE}} \right) 100\,\% \tag{3.40}$$

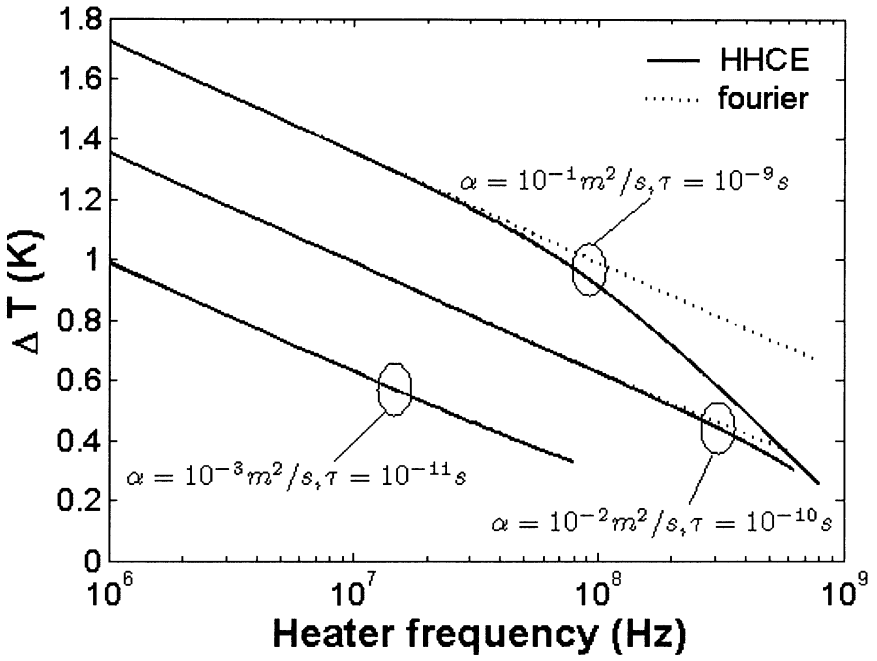

Figure 3.3: In-phase temperature oscillations measured using b = 1 μm . The 3 cases are based on the parameterization of Table 1 values for thermal diffusivity and relaxation time. Non Fourier effects are clearly evident for cases 1 and 2.

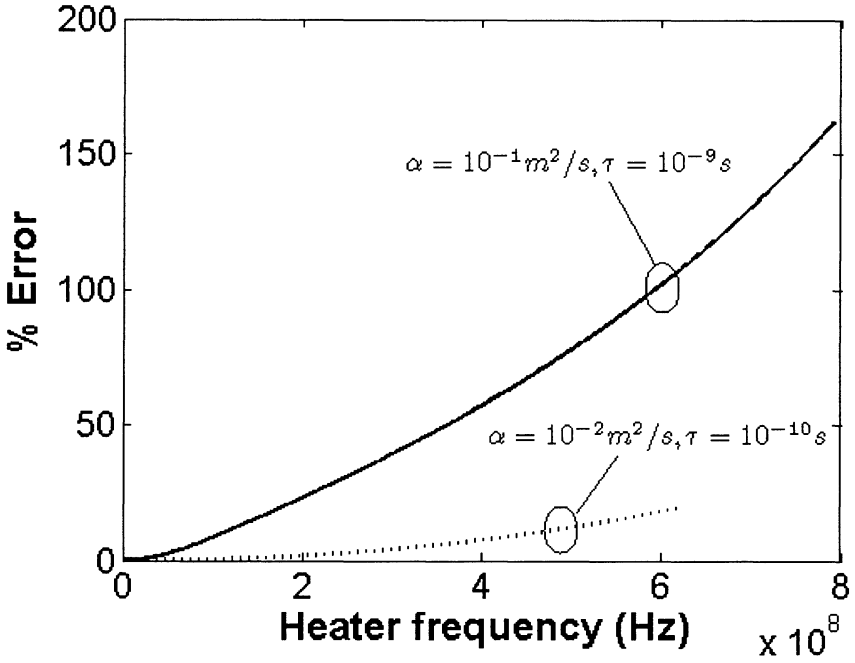

Figure 3.4: Percentage error calculated using Eq. (3.40). Only cases 1 and 2 are only displayed since for case 3 the Fourier and HHCE solutions do not differ.

Fig. 3.5 shows the temperature oscillations measured on semi-infinite sample of a-SiO_2 at 300 K. Heater width of $40\mu m$ and the thermophysical parameters available from Table 1 were used. In order to satisfy the condition $|qb| < 1$, we need to apply moderate frequencies much below the MHz regime. As a result $\tau\omega < 1/2$ thus falling into the Fourier regime of Fig. 3.2. Using Fig. 3.3 based on the combination of α, τ *and* ω, the resulting solutions obtained by Fourier and HCCE will have to be similar. We see that the result obtained is similar to the one obtained by Cahill [20].

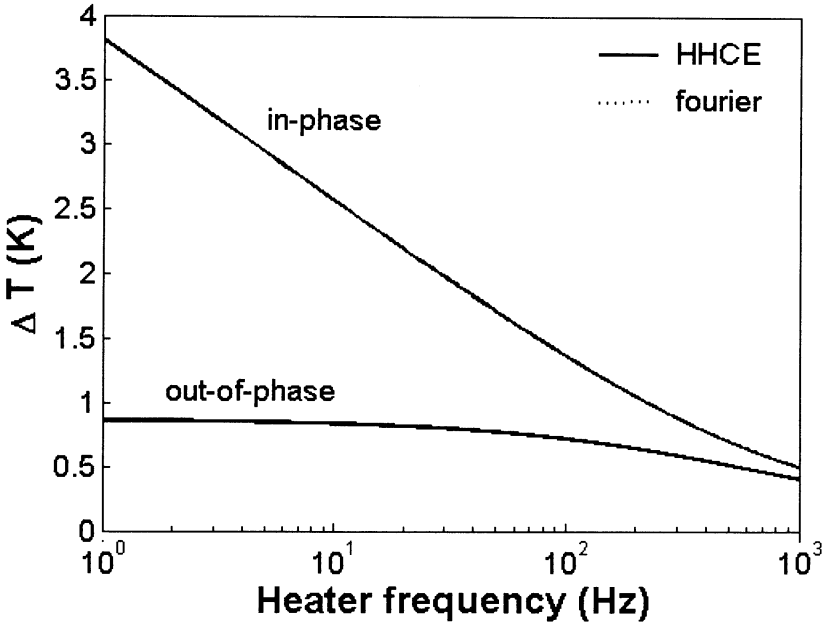

Figure 3.5: Temperature oscillations measured for a-SiO_2 using $b = 40\mu\, m$ at 300 K. Thermophysical parameters and relaxation time are obtained from Table 3.1. Non Fourier effects can be neglected since $\tau\omega < 1/2$ also evident from the similar solutions obtained by Fourier and HHCE. The results are comparable to those obtained by Cahill [20].

The $3\,\omega$ method can be applied to measure the thermal conductivity of thin films provided that the following condition is satisfied.

$$b \square \left|\frac{1}{q}\right| \square \ \textit{film thickness} \tag{3.41}$$

Physically this means that the thermal wave does not reach the other side of the film and thus the surface losses at the other end do not come into picture. Fig 3.6 shows the temperature oscillations measured on a $5\mu m$ thin CNT composite film (we use

properties of diamond since the CNT thin film properties are not known) at 100 K using a heater width of $1\mu m$. In order to satisfy Eq. (3.41), we will have to use a frequency range 100-110 MHz. At these frequencies, $\tau\omega > 1/2$ and according to Fig. 3.2 the non Fourier effects cannot be neglected. As the heater frequency gets higher, the period of the heat generated by the heater is in the regime of the relaxation time leading to a phase lag between the heat generated and the temperature oscillations thus resulting in a decrease in the magnitude of the in-phase oscillations and an increase in the magnitude of the out-of-phase oscillations. Clearly, Eq. (3.21) needs

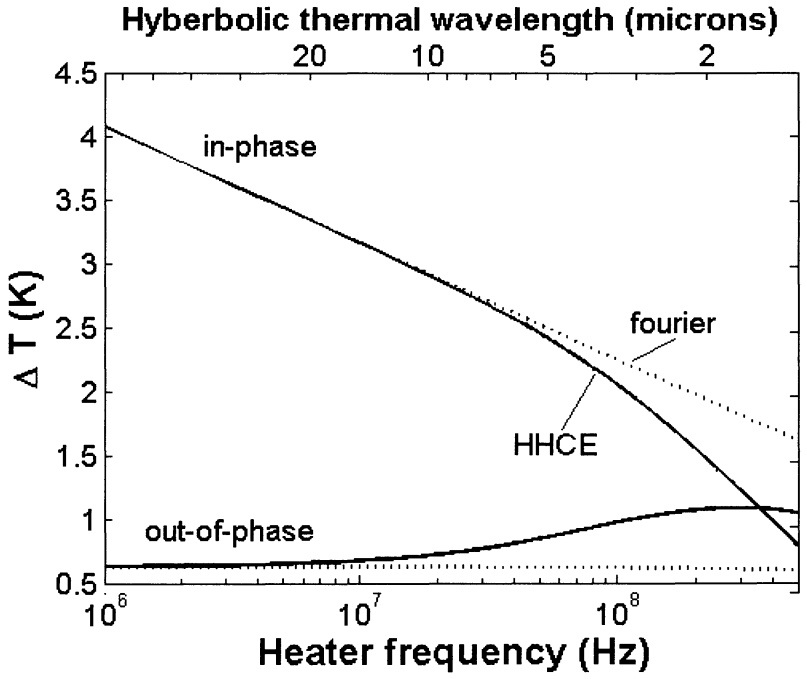

Figure 3.6: Temperature oscillations measured on a $5\mu m$ thin CNT composite film at 100 K using b = $1\ \mu m$.

to be used to calculate the thermal conductivity and using Eq. (3.38) in this case will lead to a 50 % underestimation of thermal conductivity.

In the case of biological tissues the lack of relaxation time data has curtailed our efforts to parameterize the results. Biological tissue is essentially a soft material that is electrically conductive. We believe that coating the tissue with an insulator like a-SiO_2 and then depositing the metal on the insulator, one can measure the thermal conductivity of biological tissues [57]. Fig. 3.7 shows the results obtained for bologna meat considered to be a semi-infinite substrate at 300 K using a heater width of $5\mu m$. To calculate the thermal conductivity we use a frequency range of 0.1-0.5 Hz. The relaxation time of bologna meat is high (16 secs) and the measurements falls in the $\tau\omega > 1/2$ region where non Fourier effects cannot be neglected. We see a large difference between the solutions obtained by Fourier and HHCE. Again as for thin dielectric films we see that we need to use Eq. (3.38) to obtain the correct thermal conductivity value.

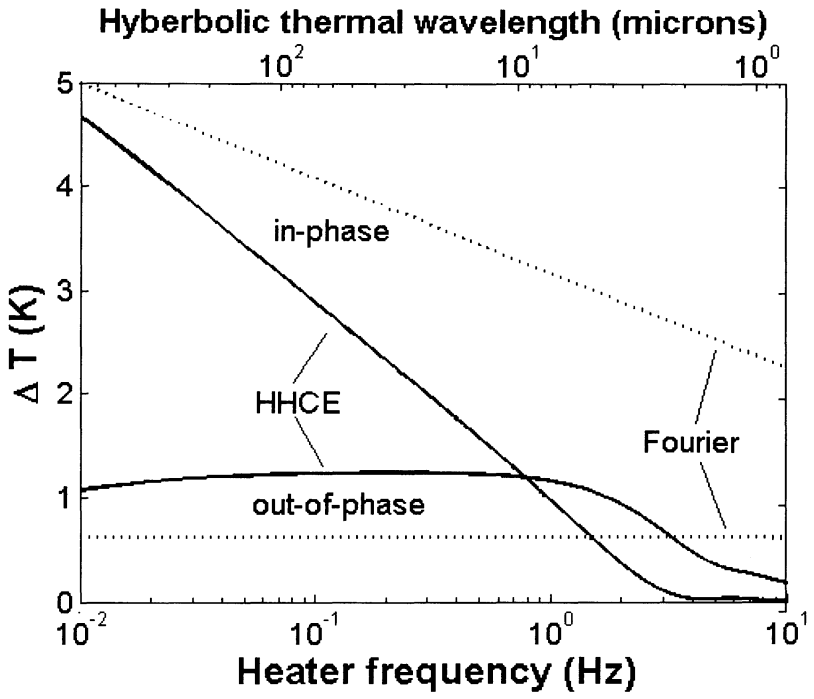

Figure 3.7: Temperature oscillations measured on bologna meat using b = $5\mu m$ at 300 K.

Chapter 4

Effect of non Fourier boundary condition on the 3 omega method

This chapter focuses on the effect of non Fourier boundary condition on the 3-omega method for measuring the thermal conductivity of thin films using hyperbolic heat conduction equation and Fourier equation. In the previous chapter we assumed the boundary condition at the heat source to be the Fourier boundary condition, whereas in this chapter we consider the heat source to be subjected to a non Fourier boundary condition. From the analysis it was observed that for thin films, neglecting the non Fourier boundary condition when using the Fourier equation leads to 80 % error in the temperature oscillations. The error increases to 85 % by not incorporating the non Fourier boundary condition and the hyperbolic heat conduction equation. The solution of Fourier equation with Fourier boundary condition underestimates the thermal conductivity and the solution of Fourier boundary condition with the hyperbolic heat conduction equation overestimates it.

The solution of the non Fourier boundary condition with the hyperbolic heat conduction equation gives the most accurate thermal conductivity expression. In addition to thermal conductivity value, the analysis also provides a method of determining the relaxation time. The relaxation time is of fundamental importance and it has been theoretically determined to be in the order of microseconds to picoseconds for metals, superconductors and semiconductors [82]. Various authors have suggested photothermal [83] and electrical techniques [84, 85] to determine the relaxation time. Both techniques are at a disadvantage because excitation and measurements must be done separately. In addition the suggested photothermal technique works only when the interface thermal resistance of the layers is negligible. Based on our analysis, we can extend the non Fourier thermal conductivity method to experimentally determine the thermal relaxation time.

4.1. Derivation of non Fourier boundary condition

The non Fourier boundary condition is derived by taking into consideration a similar physical model as shown in the previous chapter (Fig. 3.1). The heat source is considered as a line source meaning all the heat is deposited at r = 0. The finite width of the heat source will be incorporated at a later stage in the analysis. The heat from the heat source travels into the sample symmetrically across z and the azimuthal coordinate (ϕ) thus the 1D Cattaneo equation (similar to the Eq. A.25) is given by

$$\tau \frac{\partial q}{\partial t} + q = -k \frac{\partial v}{\partial r} \tag{4.1}$$

Assuming that there is no convection or radiation losses and that all the heat from the heat source goes into the sample, we see that the area (A) through with the heat travels into the sample is dependent on the distance r from the heat source and it is given by,

$$A = \pi r l \tag{4.2}$$

where l is the length of the heat source.

Considering that the heat rate (Q) is the product of heat flux (q) times the area (A), using Eq. (4.2) in Eq. (4.1) yields

$$\tau \frac{\partial Q}{\partial t} + Q = -k\pi r l \frac{\partial v}{\partial x} \tag{4.3}$$

Since the metal line is subject to joule heating with power (P) and oscillatory frequency 2ω, therefore at r = 0

$$Q = Pe^{i2\omega t} \tag{4.4}$$

Using Eq. (4.4) in Eq. (4.3) yields the non Fourier boundary condition at the heat source (i.e. as r tends to 0)

$$Lim_{r\to 0} r\frac{\partial T}{\partial r} = -\frac{Pe^{i2\omega t}}{\pi k l}\left(1 + i2\omega\tau\right) \tag{4.5}$$

4.2. Physical model

We consider a non Fourier boundary condition at the surface and solve for the temperature oscillations by considering first the hyperbolic heat conduction governing equation and then the Fourier governing equation.

4.2.1. Hyperbolic heat conduction equation

The radial flow of heat from the thin metallic film into the sample can be expressed by the following HHCE.

$$\tau\frac{\partial^2 v}{\partial t^2}+\frac{\partial v}{\partial t}=\alpha\left(\frac{\partial^2 v}{\partial r^2}+\frac{1}{r}\frac{\partial v}{\partial r}\right) \tag{4.6}$$

The boundary conditions are given by

$$lim_{r\to 0} r\frac{\partial v}{\partial r}=-\frac{Pe^{i2\omega t}}{\pi kl}\left(1+i2\omega\tau\right) \tag{4.7}$$

$$v(r=\infty,t>0)=v_i \tag{4.8}$$

$$v(r,t=0)=v_i \tag{4.9}$$

Using $T=v-v_i$, Eqs. (4.6)-(4.9) become

$$\tau\frac{\partial^2 T}{\partial t^2}+\frac{\partial T}{\partial t}=\alpha\left(\frac{\partial^2 T}{\partial r^2}+\frac{1}{r}\frac{\partial T}{\partial r}\right) \tag{4.10}$$

$$lim_{r\to 0} r\frac{\partial T}{\partial r}=-\frac{Pe^{i2\omega t}}{\pi kl}\left(1+i2\omega\tau\right) \tag{4.11}$$

$$T(r=\infty,t>0)=0 \tag{4.12}$$

$$T(r,t=0)=0 \tag{4.13}$$

We proceed with the analysis as in the previous chapter to obtain the steady periodic temperature oscillations (Appendix E.3 and F.3) measured by the metal heater

$$\Delta T = \frac{P}{\pi k l}\left(1 + i2\omega\tau\right)\int_0^\infty \frac{\sin^2(zb)}{(zb)^2\left(z^2+q^2\right)^{1/2}}\,dz \tag{4.14}$$

where

$$q \equiv \left(\frac{i2\omega}{\alpha} - \frac{4\tau\omega^2}{\alpha}\right)^{1/2} \tag{4.15}$$

Eq. (4.15) can be solved (Appendix G.3) to obtain

$$\Delta T = \mathrm{Re}(\Delta T) + i\,\mathrm{Im}(\Delta T) \tag{4.16}$$

and

$$\mathrm{Re}(\Delta T) = \frac{P}{\pi k l}\left[\frac{\ln\left((1+m)^2+n^2\right)}{2} - \frac{\ln\omega}{2} - \frac{\ln\left(4\tau^2\omega^2+1\right)}{4} - \frac{1}{4}\ln\frac{4b^4}{\alpha^2} - 2\tau\omega\left(\tan^{-1}\left(\frac{n}{1+m}\right) - \frac{1}{2}\tan^{-1}\left(\frac{1}{-2\tau\omega}\right)\right)\right] \tag{4.17}$$

$$\mathrm{Im}(\Delta T) = \frac{P(2\tau\omega)}{\pi k l}\left[\frac{\ln\left((1+m)^2+n^2\right)}{2} - \frac{\ln\omega}{2} - \frac{\ln\left(4\tau^2\omega^2+1\right)}{4} - \frac{1}{4}\ln\frac{4b^4}{\alpha^2} + \frac{1}{2\tau\omega}\left(\tan^{-1}\left(\frac{n}{1+m}\right) - \frac{1}{2}\tan^{-1}\left(\frac{1}{-2\tau\omega}\right)\right)\right] \tag{4.18}$$

where

$$m = \frac{1}{\sqrt{2}}\sqrt{1 - \frac{4\tau\omega^2 b^2}{\alpha}\sqrt{\left(1 - \frac{4\tau\omega^2 b^2}{\alpha}\right)^2 + \frac{4\omega^2 b^4}{\alpha^2}}} \tag{4.19}$$

and

$$n = \frac{\omega b^2}{\alpha m} \tag{4.20}$$

4.2.2. Fourier equation

The radial flow of heat into the sample can be expressed using the following Fourier equation

$$\frac{\partial v}{\partial t} = \alpha\left(\frac{\partial^2 v}{\partial r^2} + \frac{1}{r}\frac{\partial v}{\partial r}\right) \tag{4.21}$$

The boundary conditions are given by Eqs. (4.7-4.9). We proceed according to the analysis in the previous section to obtain the steady state temperature oscillations (Appendix E.4 and F.4) by the heater

$$\Delta T = \frac{P}{\pi k l}\left(1 + i2\omega\tau\right)\int_0^\infty \frac{\sin^2(zb)}{(zb)^2\left(z^2 + q_f{}^2\right)^{1/2}}\,dz \tag{4.22}$$

where

$$q_f \equiv \left(\frac{i2\omega}{\alpha}\right)^{1/2} \tag{4.23}$$

Eq. (4.22) can be solved (Appendix G.4) to obtain the in phase ($\mathrm{Re}(\Delta T)$) and out of phase ($\mathrm{Im}(\Delta T)$) temperature oscillations

$$\Delta T = \mathrm{Re}(\Delta T) + i\,\mathrm{Im}(\Delta T) \tag{4.24}$$

$$\mathrm{Re}(\Delta T) = \frac{P}{\pi k l}\left[\frac{\ln\left((1+m)^2 + n^2\right)}{2} - \frac{\ln\omega}{2} - \frac{1}{4}\ln\frac{4b^4}{\alpha^2} - 2\tau\omega\left(\tan^{-1}\left(\frac{n}{1+m}\right) - \frac{\pi}{4}\right)\right] \tag{4.25}$$

$$\mathrm{Im}(\Delta T) = \frac{P(2\tau\omega)}{\pi kl}\left[\frac{\ln\left((1+m)^2+n^2\right)}{2} - \frac{\ln\omega}{2} - \frac{1}{4}\ln\frac{4b^4}{\alpha^2} + \frac{1}{2\tau\omega}\left(\tan^{-1}\left(\frac{n}{1+m}\right) - \frac{\pi}{4}\right)\right] \quad (4.26)$$

where

$$m = \frac{1}{\sqrt{2}}\sqrt{1+\sqrt{1+\frac{4\omega^2 b^4}{\alpha^2}}} \quad (4.27)$$

and

$$n = \frac{\omega b^2}{\alpha m} \quad (4.28)$$

Table 4.1 provides the thermal conductivity formulas based on both the HHCE solution and the Fourier solution. It is evident that in the Fourier regime the solutions are same and hence similar expressions for thermal conductivity are obtained. This is similar to the one derived by Lee et al [51]. However, in the non Fourier regime the two solutions provide different formulas for the thermal conductivity. The physical model also provides us with a method of determining the relaxation time as will be explained later in this chapter.

Table 4.1: Thermal conductivity formulations based on the HHCE and the Fourier equation by considering non Fourier boundary condition.

Regime	Condition	Governing Equations	$\mathrm{Re}(\Delta T)$ (^{0}C)	k (W/m.^{0}C)
Fourier	$\frac{\omega b^2}{\alpha} \ll \frac{1}{4}$ and $\tau\omega < \frac{1}{2}$	HHCE	$\frac{P}{\pi kl}\left[\ln(2) - \frac{1}{2}\ln\omega - \frac{1}{4}\ln\frac{4b^4}{\alpha^2}\right]$	$-\frac{P}{2\pi l}\frac{d(\ln\omega)}{d(\mathrm{Re}(\Delta T))}$
		Fourier		
Non Fourier	$\frac{\omega b^2}{\alpha} \ll \frac{1}{4}$, $\tau\omega > \frac{1}{2}$ and $\frac{\tau\omega^2 b^2}{\alpha} \ll \frac{1}{4}$	HHCE	$\frac{P}{\pi kl}\left[\ln(2) - \ln\omega - \frac{\ln(4\tau^2)}{4} - \frac{1}{4}\ln\frac{4b^4}{\alpha^2} + \pi\tau\omega - \frac{1}{2}\right]$	$-\frac{P}{\pi l}\left(\frac{d(\ln\omega) - \pi\tau d(\omega)}{d(\mathrm{Re}(\Delta T))}\right)$
		Fourier	$\frac{P}{\pi kl}\left[\ln(2) - \frac{\ln\omega}{2} - \frac{1}{4}\ln\frac{4b^4}{\alpha^2} + \frac{\pi\tau\omega}{2}\right]$	$-\frac{P}{2\pi l}\left(\frac{d(\ln\omega) - \pi\tau d(\omega)}{d(\mathrm{Re}(\Delta T))}\right)$

4.3. Results

A Matlab code was written to numerically integrate Eq. (4.14) and Eq. (4.22) for different thermophysical parameters. Based on the thermophysical parameters we parameterized the data into different combinations of thermal diffusivities and relaxation times (Table 3.1). Fig. 4.1 shows the magnitude of the in-phase

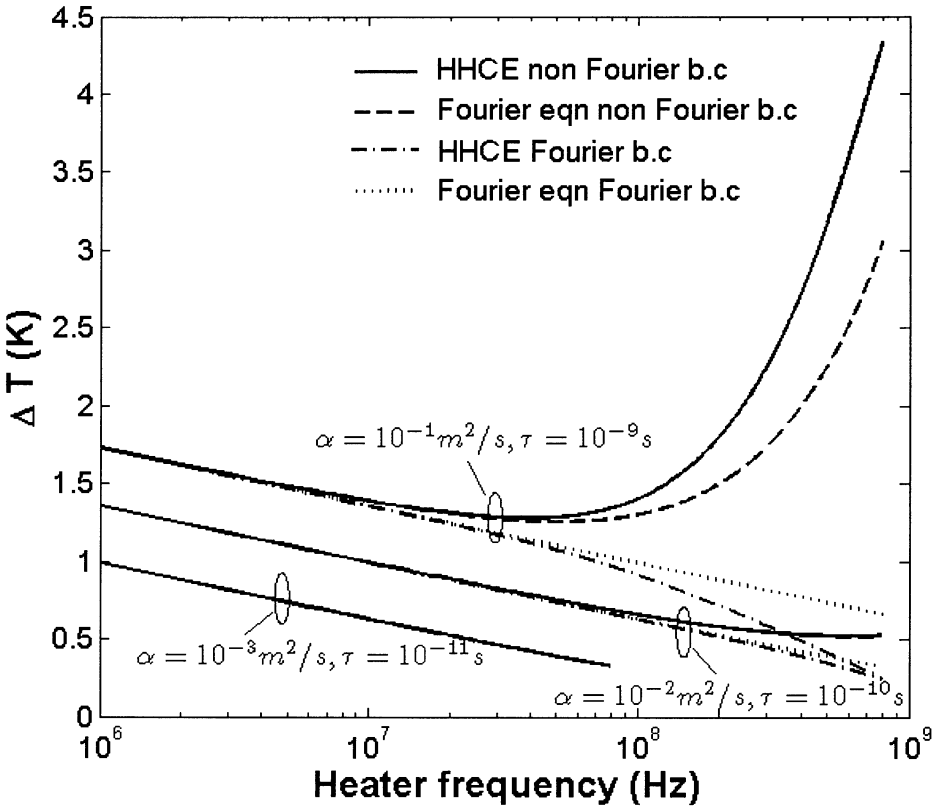

Figure 4.1: In-phase temperature oscillations measured using b = 1 μm . The solutions are based on the parameterized values of thermal diffusivity and relaxation time.

temperature oscillations obtained using a metal line half-width of $1\mu m$ for $\alpha = 10^{-1}\ m^2/s : \tau = 10^{-9}\ s$, $\alpha = 10^{-2}\ m^2/s : \tau = 10^{-10}\ s$ and $\alpha = 10^{-3}\ m^2/s : \tau = 10^{-11}\ s$. The results for the Fourier boundary condition from the previous chapter are also plotted. The frequency cutoff for each case is determined by the $|q_f b| < 1$ condition or a maximum frequency of 800 MHz. For high thermal diffusivity and high relaxation

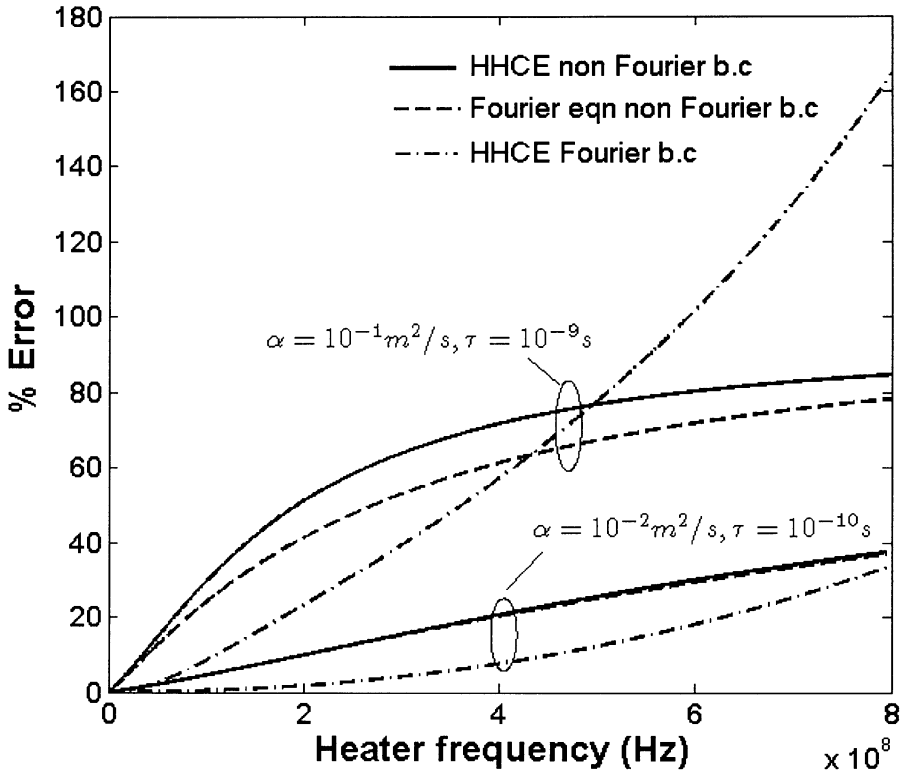

Figure 4.2: Percentage error between the solution obtained using Fourier equation with Fourier boundary condition and the solutions obtained with HHCE with Fourier boundary condition , Fourier with non Fourier boundary condition and HHCE with non Fourier boundary condition.

time, $\alpha = 10^{-1}\ m^2/s : \tau = 10^{-9}\ s$ and $\alpha = 10^{-2}\ m^2/s : \tau = 10^{-10}\ s$, we observed a significant difference between the solutions obtained by using Fourier boundary condition with Fourier equation and HHCE, and the solutions obtained using the non Fourier boundary condition with Fourier equation and HHCE. The error in the solutions predicted can be as high as 85% for HHCE with non Fourier boundary condition and 80% for Fourier equation with non Fourier boundary condition as shown in Fig. 4.2.

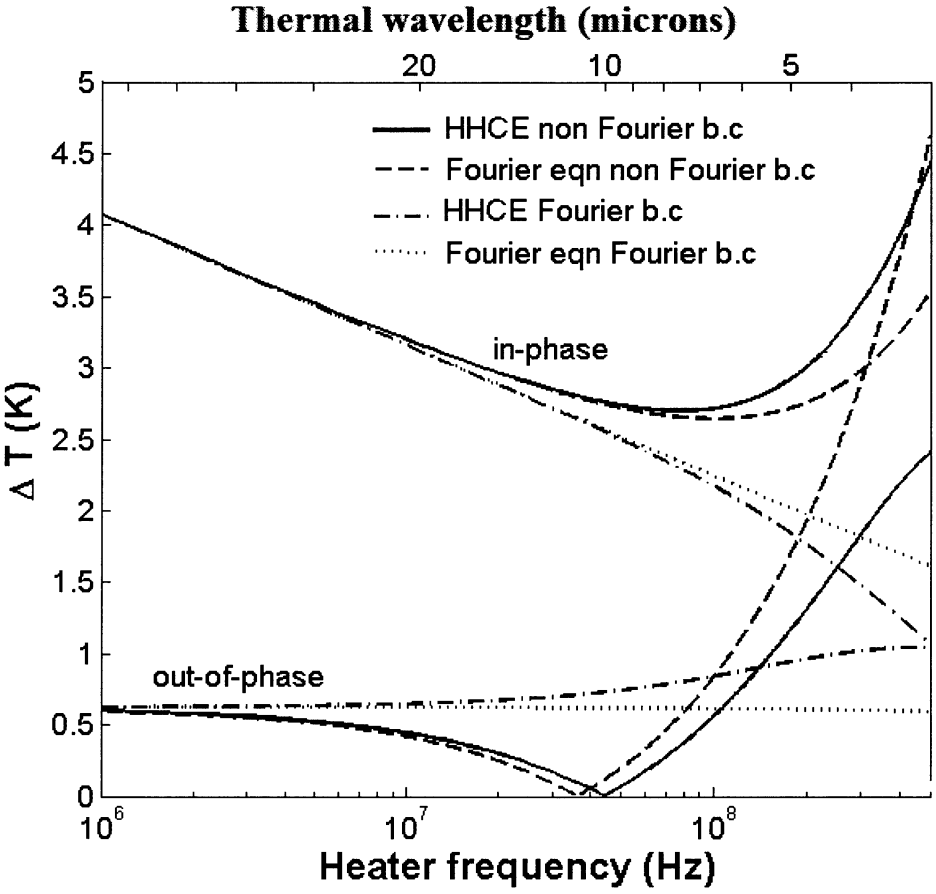

Figure 4.3: Temperature oscillations measured on a $10\mu m$ thin CNT composite film at 100 K using b = 1 μm.

Though this is lower than the error for HHCE with Fourier boundary condition (160 %), we believe that this is still significant. The error value is the percentage deviation of the solution of the Fourier equation with the Fourier boundary condition with the rest of the solutions.

Fig. 4.3 shows the temperature oscillations measured on a $10\mu m$ thin CNT composite film at 100 K using a heater width of $1\mu m$. In order for the substrate effects to be avoided we need to make sure the thermal wavelength is much smaller than the film thickness thus entailing the use of high frequencies (>100 MHz). At these frequencies, $\tau\omega > 1/2$ and we see a significant difference in the solutions obtained by using Fourier boundary condition with Fourier equation and HHCE and the solution obtained by using non Fourier boundary condition. At high frequencies, the period of the heat generated by the heater is reasonably close to the relaxation time, therefore the non Fourier effects come into picture. As the temperature oscillations travel into the sample, the solutions obtained using Fourier boundary condition predict a higher damping of the oscillations than the solutions obtained using non Fourier boundary condition [86]. As the heater frequency increases further, the damping of amplitude predicted by using non Fourier boundary condition decreases thus causing the in-phase and out-of-phase components of the amplitude to curve upwards. It is evident that since we are measuring the temperature oscillations within a certain length of the film close to the metallic heater boundary, the incorporation of the non Fourier boundary condition into the Fourier equation and the HHCE would provide solutions that are qualitatively

similar. The thermal wavelength shown in the plot in this regime denotes a minimum thermal wavelength since under non Fourier effects the waves travel further due to less attenuation. Clearly, in such a scenario we need to use the thermal conductivity formulas as tabulated in the non Fourier regime in Table 4.1. The formula obtained using non Fourier boundary condition with HHCE will provide the most accurate value.

The non Fourier boundary condition results have an interesting behavior where the in phase temperature oscillations magnitude decreases as the frequency increases, reaching a minimum value and then sharply increases. Let us consider only the solution of HHCE with non Fourier boundary condition. Taking the slope of the in-phase temperature oscillations magnitude with respect to heater frequency,

$$\frac{d(\mathrm{Re}(\Delta T))}{d\omega} = -\frac{1}{\omega} + \pi\tau \tag{4.29}$$

Therefore by knowing the heater frequency at which the in-phase temperature oscillations are a minimum, it is possible to determine the relaxation time of the CNT film using

$$\tau = \frac{1}{\pi\omega_{\min}} \tag{4.30}$$

Using a minimum frequency of 79 MHz, a relaxation time of 64 ns was obtained compared to the relaxation time of 50 ns that we used for our analysis. It is interesting to see that both values are reasonably close with similar orders of magnitude. Therefore, we see that in addition to the thermal conductivity value, the analysis provide a method to experimentally determine the relaxation time.

Chapter 5

Conclusion

Determining thermal conductance of aligned structures and thin films with embedded CNTs is extremely important if we envision their use in heat sinks, thin films and thermal interface materials. Specifically, experimental techniques were used to determine the thermal conductance of MWNT structures that were grown in silicon minichannels with water as the cooling medium whereas in the case of CNTs embedded in thin composite films, novel analytical methods were used.

In the case of MWNTs grown in a silicon minichannels with water as the cooling medium, it was observed that contrary to what previous research suggests, the presence of MWNTs enhances heat removal from the silicon base. In the single phase regime, using a fully covered MWNTs device 1.6 times the heat flux to the silicon base compared to a no MWNTs device can be applied while still maintaining the same silicon base temperature. This increase had a drawback of the fully covered MWNTs device increasing the pressure drop by 7% for 40 ml/min and 14%

for 80 ml/min. When using the 6 x 12 MWNT bundles device 2.3 times the silicon base heat flux compared to a no MWNTs device can be applied while maintaining the same silicon base temperature. The corresponding increase in pressure drop observed was 1.8 % for 40 ml/min and 3.7% for 80 ml/min. By considering the silicon minichannels as heat sinks, the fully covered MWNTs device had total thermal resistance that was 45% less when compared to the no MWNTs device. Similarly for the 6 x 12 MWNT bundles device, we obtained 57% decrease in the total thermal resistance when compared to a no MWNTs device.

It was observed that at higher heat fluxes there is increased wetting of MWNTs by water resulting in enhanced heat removal. The increase in heat transfer may also be contributed to the motion of the individual nanotube. The MWNTs are intertwined within the structures with one end fixed to the silicon surface and the other side free. The unbounded end may act like a nanoscale cantilever beam, resonating with heat and enhancing heat removal because of the Brownian motion effect similar to the phenomena in nanofluids. The computational modeling results differed from the experimental results with the experimental results showing higher heat removal than predicted by the model. This was true especially in the case of the fully grown MWNTs device. One of the reasons we attribute this is due to the fact that the computational modeling considered the MWNTs as a solid medium whereas in reality the MWNTs are a nanostructured porous medium. Therefore any future computational modeling of MWNTs should take their porosity into account.

In the case of thin films with embedded CNTs, we developed a novel non Fourier 3 omega method to determine the thermal conductivity. The analysis was initially applied by considering a Fourier boundary condition at the heat source (metal line) and subsequently a non Fourier boundary condition at the heat source was applied. It was observed in both the cases that at high heater frequencies and high relaxation times satisfying the condition given by,

$$\frac{\omega b^2}{\alpha} << \frac{1}{4} \; and \; \tau\omega > \frac{1}{2} \; and \; \frac{\tau\omega^2 b^2}{\alpha} << \frac{1}{4}$$

the non Fourier effects should not be neglected. At high frequencies, in the case of the analysis with a Fourier boundary condition the error between the temperature oscillations obtained from Fourier and HHCE governing equation were as high as 150 %. However when a non Fourier boundary condition was applied, the Fourier governing equation gave an 80 % error and the HHCE governing equation gave an 85% error in temperature oscillations when compared to the Fourier boundary condition with Fourier equation solution.

The analysis was applied to determine the thermal conductivity of a thin CNT composite film and it was observed that the use of high frequencies to measure the thermal conductivity entails that non Fourier effects be taken into consideration. There is a significant difference in the solutions obtained from HHCE and Fourier equation with non Fourier boundary condition, and HHCE and Fourier equation with Fourier boundary condition solutions. In such a case, we need to use the thermal conductivity equation based on the non Fourier regime as given in Table

4.1. We believe the thermal conductivity equation obtained using HHCE with non Fourier boundary condition would give the most accurate result. It is also clear that if one were to use the thermal conductivity equation based on the Fourier solution with Fourier boundary condition, one might underestimate the thermal conductivity whereas using the thermal conductivity equation based on the HHCE with Fourier boundary condition solution will lead to an overestimation of the thermal conductivity. It is evident that as we go to thinner films than the one considered above, the non Fourier effects become highly dominant and the temperature oscillations would travel further due to decreased attenuation thus limiting the size of the films one can measure. In addition to the expression for thermal conductivity, the analysis with the non Fourier boundary condition and the HHCE governing equation also provides a simple expression for the relaxation time. The relaxation time can be experimentally determined by finding the heater frequency at which the magnitude of the in-phase temperature oscillations is the least.

Chapter 6

Future work

The non Fourier 3 omega method for determining thermal conductivity of thin films was an analytical work and it would require experimental validation. As part of our future work we also intend to experimentally determine the thermal relaxation time of different thin films. In our analysis we considered an electrical heating method; we intend to extend our analysis to optical heating methods like laser heating that are also used to measure the thermal conductivity. Laser heating of the sample is usually carried out by using nanosecond, picosecond or femtosecond lasers that lead to temperature oscillations whose period is comparable to the relaxation time. The thermal diffusion in the sample is assumed to be governed according to Fourier's law. However, in such cases one needs to consider non Fourier effects and the thermal conductivity needs to be calculated according to HHCE.

In our research we have already dealt with aligned structures and thin films with embedded CNTs. As part of our future work we intend to embed the CNTs in bulk media and measure its thermal conductivity. Specifically, we want to create copper-CNT composites and measure its thermal conductivity. Literature search on copper-CNT composites shows that the thermal and electrical conductivity of these composites depends on the fabrication method involved. In the case of metals the thermal conductivity can be obtained from the electrical conductivity using the Weidemann Franz law [87]. The two main methods employed to fabricate copper-CNT composites are electrodeposition and sintering. Chen el al. [88] used electrodeposition to create copper-CNT composites with thermal conductivity that was 66% higher than that of pure copper. Yang et al. [89] obtained copper-CNT composites fabricated through electrodeposition with thermal conductivity comparable to that of pure copper. Copper-CNT composites created from sintering provides lower values of thermal conductivity ranging from 105 W/mK to 250 W/mK [90-92]. The authors attribute the lower values of thermal conductivity to the creation of voids in the composites. As part of our future work we intend to first create green compacts of copper and CNT powders using powder metallurgy. The green compacts will then be melted using induction heating to create the composite. The electrical conductivity of these composites will be measured and from that the thermal conductivity will be calculated. One of the advantages of induction heating is that the heating is very fast and the compacts can be melted in a matter of minutes compared to a conventional oven where it would take hours. The electromagnetic forces generated during induction heating levitate the green compact and melt it so

there is no need for a container to hold the compact. In addition the electromagnetic forces offer the added advantage of stirring the molten compact so as to minimize void creation.

We have conducted some preliminary work on the fabrication of copper-CNT composites. The copper powder obtained from Alfa Aesar (99.9% purity, -625 mesh size) has cuprous oxide that needs to be removed. The oxide impurity hinders both electrical and thermal conductivity. The de-oxidation of the copper powder

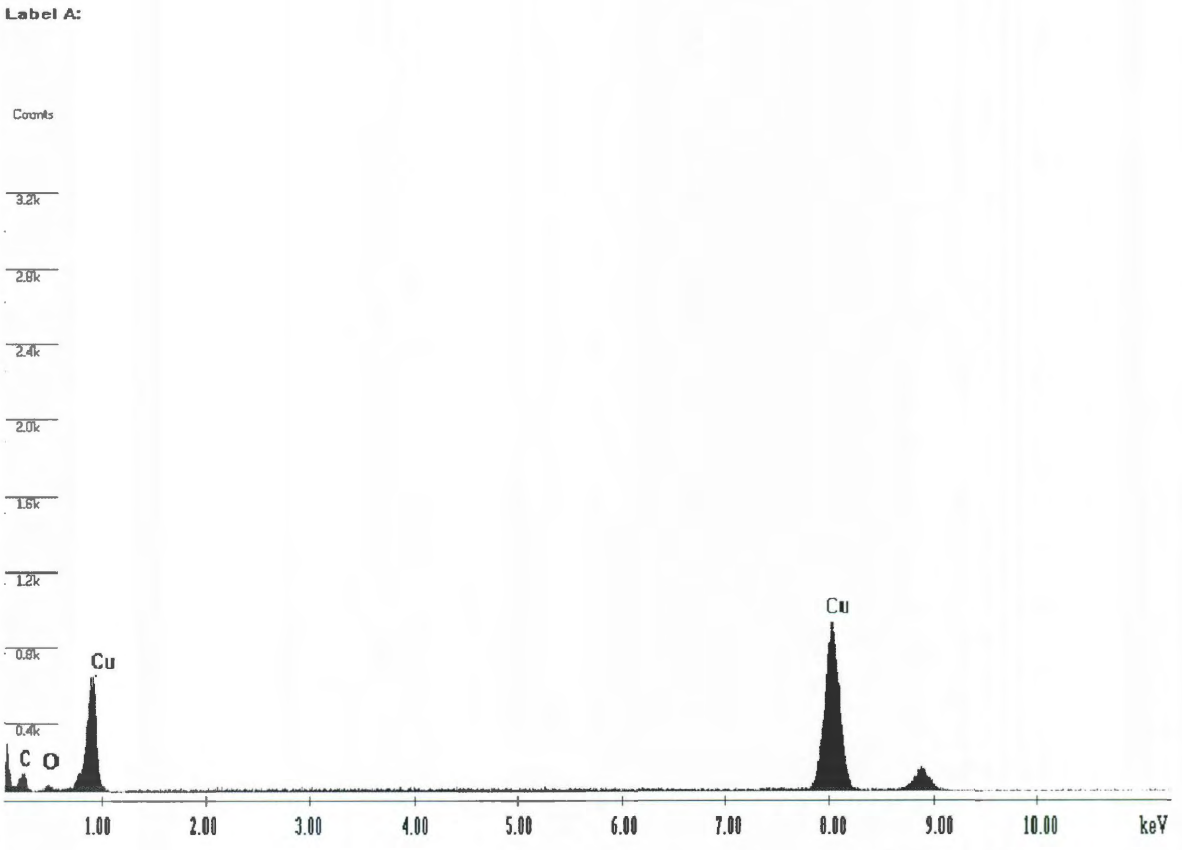

a)

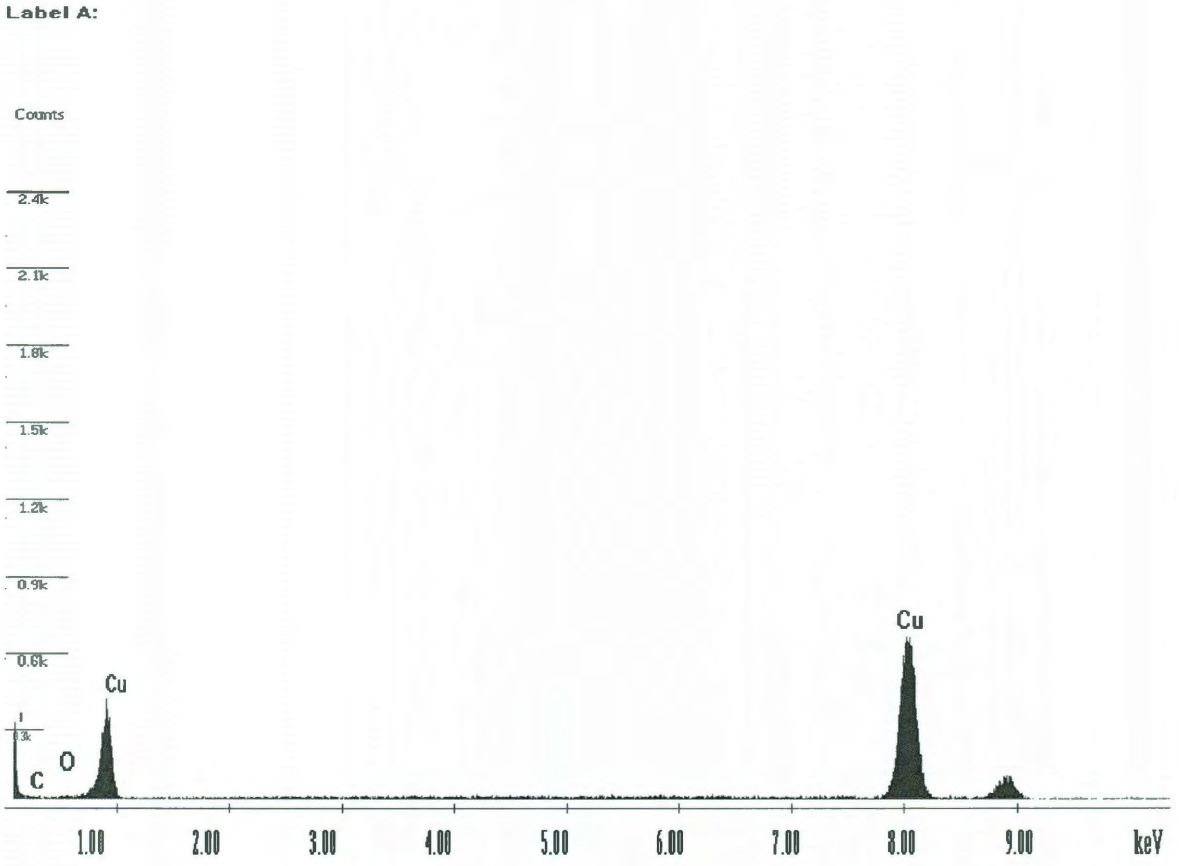

b)

Figure 6.1: Energy Dispersive Spectroscopy of a) Raw copper powder b) Hydrogen reduced copper powder.

was done using hydrogen reduction [93]. The hydrogen reduction was carried out using rapid thermal annealing at 700 ^{0}C with 200 sccm of $H_2$80%He gas. Energy Dispersive Spectroscopy (EDS) was conducted on the copper powder to determine if the oxide had been removed. Fig. 6.1a shows the EDS of the raw copper powder and the Fig. 6.1b shows the EDS of the hydrogen reduced copper powder. As seen from

the figure, the O peak denoting the presence of oxygen is quite prominent in the raw copper powder whereas the peak is hardly visible in the hydrogen reduced copper powder.

The as obtained raw HiPco CNTs were purified using the method described in [94]. 100 mg of raw HiPco CNTs were stirred at 600 rpm in 40 ml of 1N hydrochloric acid and 40 ml of hydrogen peroxide to form slurry. The slurry was heated for 6 hours at 60 ^{0}C, and the hydrogen peroxide and the hydrochloric acid were replenished every hour. The isolated CNTs were then collected on a filter paper, washed and dried to obtain purified CNTs.

A green compact of hydrogen reduced copper powder was formed by first balling milling the copper powder in a SPEX 8000 Mixer/Mill for 15 hours [95]. 5 mg of the milled copper powder was then cold compacted in a hydraulic press with 15 tsi pressure for 10 mins to obtain a green compact of 12.7 mm diameter and 5 mm in height.

The green compact was heated in a Radyne EI 40 high frequency induction heating generator. The generator converts 60 Hz of commercial power line frequency to radio frequencies of 450 KHz. The radio frequency power creates a strong electromagnetic field that induces eddy currents in metals and is sufficient to melt them. The green compact requires an inert argon atmosphere and this is accomplished by using a glove box that has been specifically altered to house the conical coil that will carry the high frequency power. A conical coil is used since it will provide a means to levitate and melt the compact. At this point we encountered

several issues that need to be resolved with respect to the glove box and the radio frequency generator. One of the major issues is the inability to create an inert atmosphere due to a leaky glove box. The lack of inert atmosphere is leading to the oxidation of the compact as it gets heated to high temperatures. Different methods were tried to plug the leaks, from replacing the rubber gloves on the glove box to replacing the o-rings. However, the creation of inert atmosphere in the glove box still remains elusive. We believe the glove box will have to be replaced. The second issue encountered was the inability to both levitate and melt the compact. The generator provides enough power to levitate the compact but not enough to melt it. The generator has a failed rectifier due to which we were able to go only up to 9 KV while the generator is rated up to 12 KV. At 9 KV the generator trips and shuts down. Replacing the rectifier would allow the generator to go up to 12 KV and could result in both levitating and melting the compact.

Appendix A: Derivation of non Fourier Equation

We begin with considering the Boltzmann Transport Equation for a classical system of N molecules. If there are m degrees of freedom, then the coordinated needed to specify the system are l = Nm. With regard to the phase space we have l coordinates of $\hat{q}_i$ and l corresponding momenta $\hat{p}_j$. Thus by knowing the initial values of the phase space, one can determine the time evolution of the system using equations of motion.

A phase point describes the state of a system at time t. As time changes, the phase points traces out a trajectory. Let us consider an ensemble approach with microcanonical (NVU) systems. We can define the number density $f_{es}(p,q,t)$ of the ensemble such that $f_{es}(p,q,t)dpdq$ gives the number of phase points in the region dpdq about p,q at time t in the phase space. where $p \in \hat{p}_1, \hat{p}_2 \ldots\ldots\ldots \hat{p}_l$, $q \in \hat{q}_1, \hat{q}_2 \ldots\ldots\ldots \hat{q}_l$, $dp \in \hat{dp}_1, \hat{dp}_2 \ldots\ldots\ldots \hat{dp}_l$, $dq \in \hat{dq}_1, \hat{dq}_2 \ldots\ldots\ldots \hat{dq}_l$

Consider a differential element in the phase space $\hat{\delta p}_1, \hat{\delta p}_2 \ldots\ldots\ldots \hat{\delta p}_l$, $\hat{\delta q}_1, \hat{\delta q}_2 \ldots\ldots\ldots \hat{\delta q}_l$ about the point $\hat{p}_1, \hat{p}_2 \ldots\ldots\ldots \hat{p}_l$, $\hat{q}_1, \hat{q}_2 \ldots\ldots\ldots \hat{q}_l$. The number of phase points within this element is

$$\delta n = f_{es}(\hat{p}_1, \hat{p}_2 \ldots\ldots \hat{p}_l, \hat{q}_1, \hat{q}_2 \ldots\ldots_l)\, \hat{\delta p}_1, \hat{\delta p}_2 \ldots\ldots \hat{\delta p}_l, \hat{\delta q}_1, \hat{\delta q}_2 \ldots\ldots \hat{\delta q}_l \qquad \text{(A.1)}$$

The number of points entering and leaving this volume element changes with time.

If we consider points entering at $\hat{q}_1$ per unit time

$$\dot{\delta n}|_{q_1} = f_{es}\, \hat{\delta p}_1 . \hat{\delta p}_2 \ldots\ldots\ldots \hat{\delta p}_l . \hat{\delta q}_1 . \hat{\delta q}_2 \ldots\ldots\ldots \hat{\delta q}_l . \frac{\dot{\hat{q}}_1}{\hat{\delta q}_1} \qquad \text{(A.2)}$$

where $\dot{\hat{q}}_1$ is the velocity at $\hat{q}_1$. At $\hat{q}_1 + \mathrm{d}\hat{q}_1$, the number of points leaving the system

$$\dot{\delta n}|_{\hat{q}_1 + d\hat{q}_1} = \left(f_{es} + \frac{\partial f_{es}}{\partial \hat{q}_1} \hat{\delta q}_1 \right) \hat{\delta p}_1 . \hat{\delta p}_2 \ldots\ldots \hat{\delta p}_l . \hat{\delta q}_1 . \hat{\delta q}_2 \ldots\ldots \hat{\delta q}_l . \frac{\left(\dot{\hat{q}}_1 + \frac{\partial \dot{\hat{q}}_1}{\partial \hat{q}_1} \hat{\delta q}_1 \right)}{\hat{\delta q}_1} \qquad \text{(A.3)}$$

Subtracting Equation A.3 from Equation A.2

$$\dot{\delta n}|_{\hat{q}_1} - \dot{\delta n}|_{\hat{q}_1 + d\hat{q}_1} = -\left(\frac{\partial f_{es}}{\partial \hat{q}_1} \hat{q}_1 + f_{es} \frac{\partial \dot{\hat{q}}_1}{\partial \hat{q}_1} \right) \hat{\delta p}_1 . \hat{\delta p}_2 \ldots\ldots \hat{\delta p}_l . \hat{\delta q}_1 . \hat{\delta q}_2 \ldots\ldots \hat{\delta q}_l \qquad \text{(A.4)}$$

Similarly for momenta,

$$\dot{\delta n}|_{\hat{p}_1} - \dot{\delta n}|_{\hat{p}_1 + d\hat{p}_1} = -\left(\frac{\partial f_{es}}{\partial \hat{p}_1} \hat{p}_1 + f_{es} \frac{\partial \dot{\hat{p}}_1}{\partial \hat{p}_1} \right) \hat{\delta p}_1 . \hat{\delta p}_2 \ldots\ldots \hat{\delta p}_l . \hat{\delta q}_1 . \hat{\delta q}_2 \ldots\ldots \hat{\delta q}_l \qquad \text{(A.5)}$$

The net flow into the volume is found by summing the contributions from all directions in phase space

$$\dot{\delta n} = -\sum_{j=1}^{l}\left(\frac{\partial f_{es}}{\partial \hat{q}_1}\hat{q}_1 + f_{es}\frac{\partial \dot{\hat{q}}_1}{\partial \hat{q}_1} + \frac{\partial f_{es}}{\partial \hat{p}_j}\hat{p}_j + f_{es}\frac{\partial \dot{\hat{p}}_j}{\partial \hat{p}_j}\right)\hat{\delta p}_1.\hat{\delta p}_2....\hat{\delta p}_l.\hat{\delta q}_1.\hat{\delta q}_2....\hat{\delta q}_l \qquad \text{(A.6)}$$

The net flow of phase points through the volume element is equal to the change of δn with respect to time.

$$\frac{\partial(\delta n)}{\partial t} = \dot{\delta n} \qquad \text{(A.7)}$$

We note that the Hamiltonian (H) satisfies the following relations

$$\frac{\partial \hat{H}}{\partial \hat{p}_j} = \dot{\hat{q}}_j \qquad \text{(A.8)}$$

$$\frac{\partial \hat{H}}{\partial \hat{q}_j} = -\dot{\hat{p}}_j \qquad \text{(A.9)}$$

Differentiating the Equation A.8 with respect to $\partial \hat{q}_j$ and Equation A.9 with respect to $\partial \hat{p}_j$, we have

$$\frac{\partial \dot{\hat{q}}_j}{\partial \hat{q}_j} = -\frac{\partial \dot{\hat{p}}_j}{\partial \hat{p}_j} \qquad \text{(A.10)}$$

Using Equation A.10 in Equation A.7 and using Equation A.1 to eliminate δn

$$\frac{\partial f_{es}}{\partial t} = -\sum_{j=1}^{l}\left(\frac{\partial f_{es}}{\partial \hat{q}_j}\dot{\hat{q}}_j + \frac{\partial f_{es}}{\partial \hat{p}_j}\dot{\hat{p}}_j\right) \tag{A.11}$$

If we now consider each system in the ensemble to be a particle and imagine a system that contains non interacting particles with distribution function f_{ep} the above relation holds

$$\frac{\partial f_{ep}}{\partial t} + \sum_{j=1}^{l}\left(\frac{\partial f_{ep}}{\partial \hat{q}_j}\dot{\hat{q}}_j + \frac{\partial f_{ep}}{\partial \hat{p}_j}\dot{\hat{p}}_j\right) = 0 \tag{A.12}$$

Defining generalized coordinates $\hat{z}_j$ and velocities $\hat{w}_j$ (related to momenta) Equation A.12 becomes

$$\frac{\partial f_{ep}}{\partial t} + \sum_{j=1}^{l}\left(\frac{\partial f_{ep}}{\partial \hat{z}_j}\dot{\hat{z}}_j + \frac{\partial f_{ep}}{\partial \hat{w}_j}\dot{\hat{w}}_j\right) = 0 \tag{A.13}$$

Using the relation between coordinates and velocities Equation A.13 further simplifies to

$$\frac{\partial f_{ep}}{\partial t} + \sum_{j=1}^{l}\left(\frac{\partial f_{ep}}{\partial \hat{z}_j}\hat{w}_j + \frac{\partial f_{ep}}{\partial \hat{w}_j}\dot{\hat{w}}_j\right) = 0 \tag{A.14}$$

If we consider that collisions take place between the different particles then the RHS of Eq. (A.14) equates to a collision term

$$\left(\frac{\partial f_{ep}}{\partial t}\right)_{coll.} = \frac{\partial f_{ep}}{\partial t} + \sum_{j=1}^{l}\left(\frac{\partial f_{ep}}{\partial \hat{z}_j}\hat{w}_j + \frac{\partial f_{ep}}{\partial \hat{w}_j}\dot{\hat{w}}_j\right) \tag{A.15}$$

A fraction distribution f would also satisfy the Eq. (A.15). Therefore

$$\left(\frac{\partial f}{\partial t}\right)_{coll.} = \frac{\partial f}{\partial t} + \sum_{j=1}^{l}\left(\frac{\partial f}{\partial \hat{z}_j}\hat{w}_j + \frac{\partial f}{\partial \hat{w}_j}\dot{\hat{w}}_j\right) \tag{A.16}$$

The collision term can be treated with the introduction of relaxation time τ and equilibrium distribution f_0 such that

$$\left(\frac{\partial f}{\partial t}\right)_{coll.} = -\frac{f - f_0}{\tau(z_j, w_j)} \tag{A.17}$$

Eq. (A.16) is the Boltzmann Transport Equation which describes the time evolution of a classical mechanical system in non equilibrium.

Let us now derive the non Fourier heat conduction equation for a 1-D classical mechanical system with no external force applied (the acceleration term $\dot{\hat{w}}_j$ goes to zero). If u_x is the velocity in the x direction, then Boltzmann Transport Equation becomes

$$\frac{\partial f}{\partial t} + \frac{\partial f}{\partial x}u_x = -\frac{(f - f_0)}{\tau} \tag{A.18}$$

Energy flux is given by $q(x,t) = \int u_x f \varepsilon D(\varepsilon) d\varepsilon$ where $D(\varepsilon)$ is the density of states

Multiplying Equation A.18 by $u_x \varepsilon D(\varepsilon) d\varepsilon$ and integrating over all energy states

$$\frac{\partial q}{\partial t} + \int {u_x}^2 \frac{\partial f}{\partial x} \varepsilon D(\varepsilon) d\varepsilon = -\int \frac{f}{\tau} u_x \varepsilon D(\varepsilon) d\varepsilon + \int \frac{f_0}{\tau} u_x \varepsilon D(\varepsilon) d\varepsilon$$

(A.19)

The last integral term goes to zero since integrating the equilibrium distribution over energy goes to zero.

$$\frac{\partial q}{\partial t} + \int {u_x}^2 \frac{\partial f}{\partial x} \varepsilon D(\varepsilon) d\varepsilon = -\int \frac{f}{\tau} u_x \varepsilon D(\varepsilon) d\varepsilon \qquad \text{(A.20)}$$

We now make two assumptions

a) τ is constant

b) $\frac{\partial f}{\partial x} = \left(\frac{df_0}{d\nu}\right)\left(\frac{\partial \nu}{\partial x}\right)$

Based on our assumptions, Eq. (A.20) simplifies to

$$\frac{\partial q}{\partial t} + \int \left(\frac{df_0}{dT}\right)\left(\frac{\partial \nu}{\partial x}\right) {u_x}^2 \varepsilon D(\varepsilon) d\varepsilon = -\frac{1}{\tau} \int f u_x \varepsilon D(\varepsilon) d\varepsilon \qquad \text{(A.21)}$$

Solving Boltzmann Transport Equation for steady state yields $f = f_0 - \tau u_x \frac{\partial f}{\partial x}$ and substituting in Eq. (A.21)

$$\frac{\partial q}{\partial t} - \int \left(\frac{df_0}{d\nu}\right)\left(\frac{\partial \nu}{\partial x}\right) {u_x}^2 \varepsilon D(\varepsilon) d\varepsilon = \frac{1}{\tau} \int \tau {u_x}^2 \frac{\partial f}{\partial x} \varepsilon D(\varepsilon) d\varepsilon \qquad \text{(A.22)}$$

If we assume the temperature gradient $\frac{\partial \nu}{\partial x}$ to be negative then the heat flux q and thermal conductivity k can be defined as

$$q = \frac{\partial \nu}{\partial x} \int u_x^{\,2} \frac{df_0}{d\nu} \varepsilon D(\varepsilon) d\varepsilon \tag{A.23}$$

$$\mathrm{k} = \int u_x^{\,2} \frac{df_0}{d\nu} \varepsilon D(\varepsilon) d\varepsilon \tag{A.24}$$

Using Eq. (A.23) and Eq. (A.24) in Eq. (A.22), we get

$$\frac{\partial q}{\partial t} + \frac{q}{\tau} = -\frac{1}{\tau} \frac{\partial (k\nu)}{\partial x} \tag{A.25}$$

Eq. (A.25) is the non Fourier heat conduction equation. It is also known as the Cattaneo equation. Differentiating Eq. (A.25) with respect to x and combining it with the conservation of energy equation

$$\rho c_p \frac{\partial \nu}{\partial t} + \frac{\partial q}{\partial x} = 0 \tag{A.26}$$

We get non Fourier heat conduction equation in the hyperbolic form

$$\frac{\partial}{\partial x}\left(k \frac{\partial \nu}{\partial x} \right) = \rho c_p \left(\frac{\partial \nu}{\partial t} + \tau \frac{\partial^2 \nu}{\partial t^2} \right) \tag{A.27}$$

Appendix B: Calibration of pressure transducer

The differential pressure transducer was calibrated using a dead weight tester. A dead weight tester has a piston cylinder mechanism and works on the basic principle that the pressure is the ratio or force over area. The force applied on the piston is generally known through the use of calibrated weights. The differential pressure transducer was connected to the dead weight tester and a known pressure was applied. The corresponding millivolt (mV) reading from the pressure transducer was read using a multimeter. The pressures applied spanned the operational pressure of the pressure transducer i.e. from 0 – 30 psi. Once a minimum set of points was obtained (more than 3), the results were plotted (Fig. B.1) and a linear equation giving the corresponding pressure value from the voltage reading. The R^2 value obtained was close to 1 thus validating the accuracy of our curve fitting. The dead weight tester provides known pressure through psi values and so to convert the value to Pascal we used Eq. (B.1).

$$\Pr essure = 6894.75 * (239.2666 * (mV) - 0.3472) \quad \text{(B.1)}$$

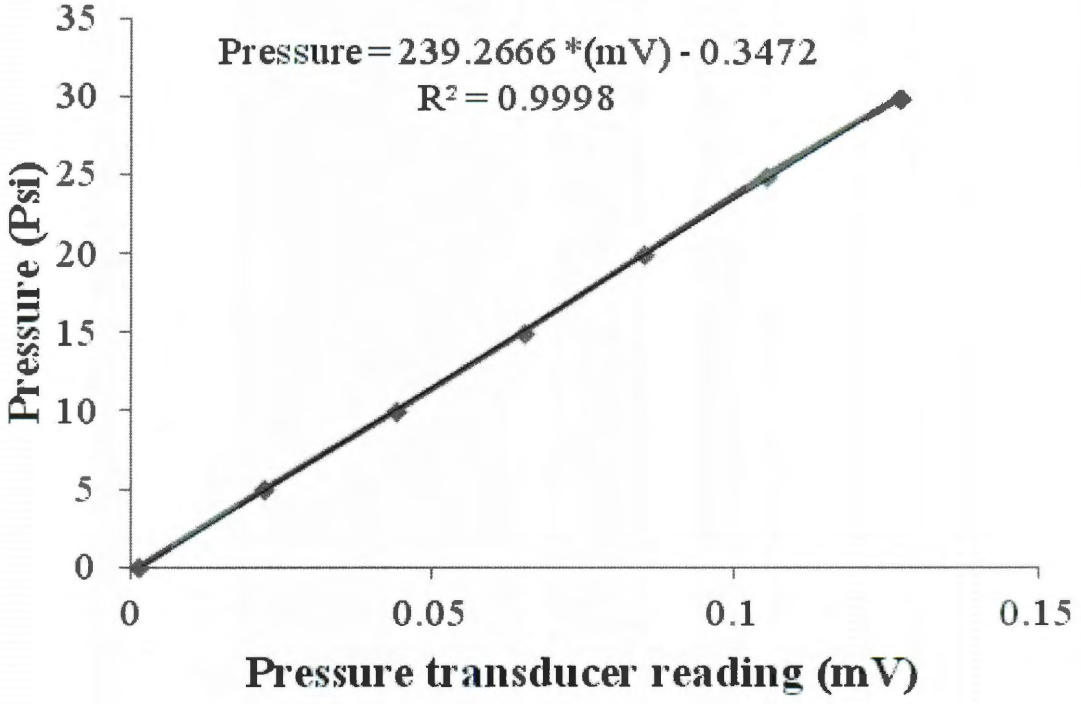

Figure B.1: Pressure vs millivolt reading of the pressure transducer

Appendix C: Heat loss calculations

Heat loss is unavoidable in our experiment though we have sufficiently insulated the heat carrying components. It is important that heat loss be calculated and the correct heat flux applied to the silicon base of the three devices be determined. To calculate our heat loss (HL) we obtain a relation between the heat flux (hf_{num}) and the base temperature (T_w) for a particular flow rate using the numerical results of the no MWNTs device as shown in Fig. C.1. The heat loss for a particular flow rate and a particular base temperature can now be calculated using the experimental results.

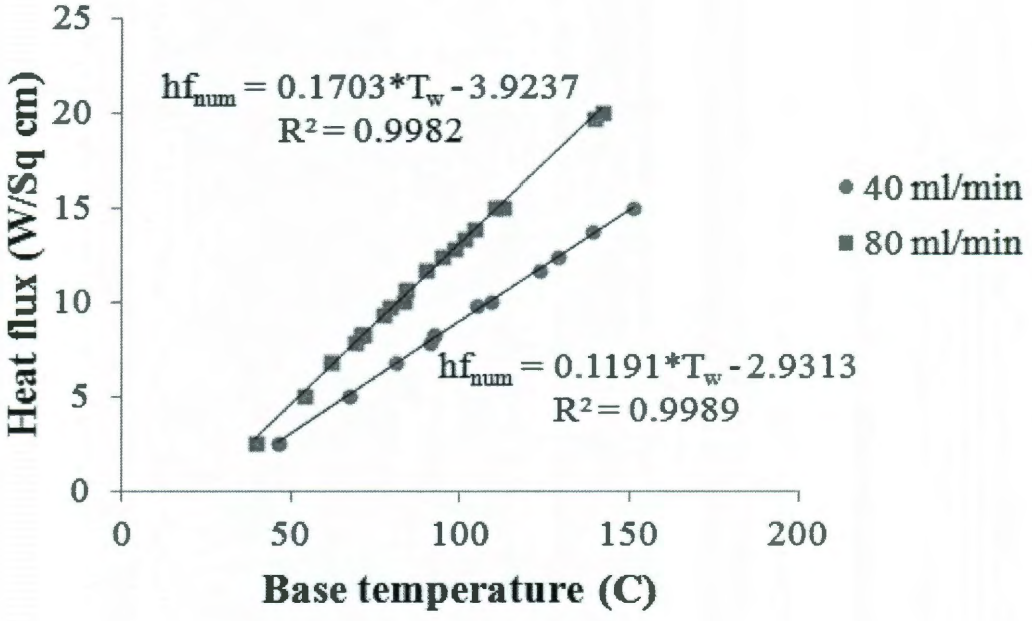

Figure C.1: Numerical results for No MWNTs device

Table C.1 gives the heat loss calculation details for 40 ml/min and Table C.2 gives the heat loss calculation details for 80 ml/min. The numerical heat flux shown in the tables is obtained using the relations obtained in Fig. C.1. The corresponding heat loss equations:

For 40 ml/min,

$$HL_{40} = -0.0286 * T_w + 5.3389 \quad \text{(C.1)}$$

For 80 ml/min,

$$HL_{80} = -0.0529 * T_w + 5.7908 \quad \text{(C.2)}$$

Therefore by using Eqs. (C.1) and (C.2), we can find out the heat loss for a particular base temperature for the fully covered MWNTs device and the 6 x 12 MWNT bundles device. The heat loss values obtained can then be used to adjust the experimental heat flux values for these two devices to obtain the heat flux applied to the base.

Table C.1: Heat loss calculations for 40 ml/min

Run #	Base Temperature (C)	Heat flux (W/sq cm)		Heat loss (W/sq cm)
		Experimental	Numerical	
Run 1	26.11722222	4.97722222	0.179261167	4.797961056
	34.763375	5.877125	1.209017963	4.668107038
	45.80425	7.14975	2.523986175	4.625763825
	60.97916667	8.60041667	4.33131875	4.269097917
	78.837	10.1726923	6.4581867	3.714505608
	104.9083636	12.8353636	9.563286109	3.272077527
	127.6186923	14.9979231	12.26808625	2.729836823
	142.6385714	16.1272143	14.05695386	2.070260429
Run 2	25.94730769	4.77446154	0.159024346	4.615437192
	33.957	5.92791667	1.1129787	4.814937967
	45.84990909	7.20890909	2.529424173	4.679484918
	62.45563636	8.71827273	4.507166291	4.211106436
	79.46736364	10.3649091	6.533263009	3.831646082
	104.7893333	12.5043333	9.5491096	2.955223733
	121.3006364	14.4062727	11.51560579	2.890666936
	142.2982222	16.4764444	14.01641827	2.460026178

Table C.2: Heat loss calculations for 80 ml/min

Run #	Base Temperature (C)	Heat flux (W/sq cm)		Heat loss (W/sq cm)
		Experimental	Numerical	
Run 1	26.8845625	5.09460562	0.654740994	4.439864627
	33.44072222	6.05327778	1.771254994	4.282022783
	44.68942857	6.81752381	3.686909686	3.130614124
	57.47578947	8.344	5.864426947	2.479573053
	74.28215385	10.3611538	8.7265508	1.634603046
	89.22816667	11.878	11.27185678	0.606143217
	110.1073333	14.5302667	14.82757887	-0.2973122
	130.5821818	16.8554545	18.31444556	-1.458991018
	145.3051818	18.8609091	20.82177246	-1.960863373
Run 2	26.20677778	4.8061	0.539314256	4.266785744
	33.6988125	5.866375	1.815207769	4.051167231
	44.06184615	6.94076923	3.5800324	3.360736831
	59.715125	9.07085714	6.245785788	2.825071355
	69.364	10.4936667	7.8889892	2.604677467
	93.275	13.1940769	11.9610325	1.233044423
	110.6349286	15.2995714	14.91742834	0.382143093
	125.00525	16.3946667	17.36469408	-0.970027408
	137.6501	18.3617	19.51811203	-1.15641203

Appendix D: Uncertainty analysis

The experimentally measured quantities are the flow rate, the temperature and the pressure drop. The uncertainties for the rotameter and the pressure transducer are factory provided and are 6% and 7% respectively. To calculate the uncertainty in the measurement of the thermocouples, the thermocouples were dipped in a constant temperature bath. The bath temperature was accurately determined using an Omega DP32 thermocouple. The experimental thermocouple measurements and the Omega DP32 thermocouple measurements were recorded and then analyzed statistically to determine the uncertainty in the temperature measured by the thermocouples. The uncertainty calculated was within 0.1 ^{0}C for the thermocouples. Since the heat flux was a derived quantity using the Fourier equation,

$$q = k\frac{\Delta T}{\Delta x} \tag{D.1}$$

Therefore, we used the Kline and Mclintock method [96] to determine the uncertainty.

$$\frac{\omega_q}{q} = \sqrt{\left(\frac{\omega_k}{k}\right)^2 + 2\left(\frac{\omega_T}{\Delta T}\right)^2 + \left(\frac{\omega_x}{\Delta x}\right)^2} \tag{D.2}$$

where k, ΔT and Δx are the thermal conductivity, the difference between adjacent thermocouple temperatures and the distance between adjacent thermocouples; and ω_k, ω_T and ω_x are the associated uncertainties respectively. The thermal

conductivity uncertainty and the position uncertainty were negligible and the Eq. (D.2) reduced to

$$\frac{\omega_q}{q} = \sqrt{2}\left(\frac{\omega_T}{\Delta T}\right) \tag{D.3}$$

Uncertainties were determined using Eq. (D.3) for each of the three heat fluxes for every base temperature and an average uncertainty was determined. The average uncertainties for the heat flux ranged from 3.6% to 17% with the uncertainties being higher at lower heat fluxes.

Appendix E: Steady state solution

E.1 Solution of hyperbolic heat conduction equation with Fourier boundary condition

The governing hyperbolic heat conduction equation and the boundary conditions are as follows

$$\tau\frac{\partial^2 T}{\partial t^2}+\frac{\partial T}{\partial t}=\alpha\left(\frac{\partial^2 T}{\partial r^2}+\frac{1}{r}\frac{\partial T}{\partial r}\right) \tag{E.1}$$

$$Lim_{r\to 0} r\frac{\partial T}{\partial r}=-\frac{Pe^{i2\omega t}}{\pi kl} \tag{E.2a}$$

$$\Delta T(r=\infty, t>0)=0 \tag{E.2b}$$

$$T(r,t=0)=0 \tag{E.2c}$$

In general the steady state oscillations are given by

$$T(r,t)=\Delta T(r)e^{i2\omega t} \tag{E.3}$$

Substituting Eq. (E.3) in Eq. (E.1), the oscillatory component cancels out to give an equation that consists of only the position component

$$r^2\frac{d^2(\Delta T)}{dr^2}+r\frac{d(\Delta T)}{dr}-r^2\left(\frac{i2\omega}{\alpha}-\frac{4\omega^2\tau}{\alpha}\right)\Delta T=0 \tag{E.4}$$

The corresponding boundary conditions given by Eq. (E.2a) and (E.2b) become

$$Lim_{r\to 0} r\frac{\partial(\Delta T)}{\partial r} = -\frac{P}{\pi kl} \tag{E.5a}$$

$$\Delta T(r=\infty, t>0) = 0 \tag{E.5b}$$

Substituting R = qr where $q \equiv \left(\frac{i2\omega}{\alpha} - \frac{4\tau\omega^2}{\alpha}\right)^{1/2}$ in Eq. (E.4), the equation becomes

$$R^2\frac{d^2(\Delta T)}{dR^2} + R\frac{d(\Delta T)}{dR} - R^2\Delta T = 0 \tag{E.6}$$

The general solution to Eq. (E.6) [97] is

$$\Delta T(r) = C_1 I_0(qr) + C_2 K_0(qr) \tag{E.7}$$

Using boundary condition Eq. (E.5b) we get $C_1 = 0$

$$\Delta T(r) = C_2 K_0(qr) \tag{E.8}$$

Using boundary condition Eq. (E.6b), we get

$$C_2 Lim_{r\to 0}(qr) K_1(qr) = \frac{P}{\pi kl} \tag{E.9}$$

From [98], we know in general

$$Lim_{\xi\to 0}\xi^n K_n(\xi) = 2^{n-1}(n-1)! \tag{E.10}$$

Using Eqs. (E.10) and (E.9), we have $C_2 = P/\pi kl$, Therefore solution for temperature amplitude in terms of position is given by

$$\Delta T(r) = \frac{P}{\pi kl} K_0(qr) \tag{E.11}$$

E.2 Solution of Fourier equation with Fourier boundary condition

The governing Fourier conduction equation and the boundary conditions are as follows

$$\frac{\partial T}{\partial t} = \alpha\left(\frac{\partial^2 T}{\partial r^2} + \frac{1}{r}\frac{\partial T}{\partial r}\right) \tag{E.12}$$

$$Lim_{r\to 0} r\frac{\partial T}{\partial r} = -\frac{Pe^{i2\omega t}}{\pi kl} \tag{E.13a}$$

$$\Delta T(r=\infty, t>0) = 0 \tag{E.13b}$$

$$T(r, t=0) = 0 \tag{E.13c}$$

In general the steady state oscillations are given by

$$T(r,t) = \Delta T(r)e^{i2\omega t} \tag{E.14}$$

Substituting Eq. (E.14) in Eq. (E.12), we get an equation that consists of only the position component

$$r^2\frac{d^2(\Delta T)}{dr^2} + r\frac{d(\Delta T)}{dr} - r^2\left(\frac{i2\omega}{\alpha}\right)\Delta T = 0 \tag{E.15}$$

The corresponding boundary conditions given by Eq. (E.13a) and (E.13b) become

$$Lim_{r\to 0} r\frac{\partial(\Delta T)}{\partial r} = -\frac{P}{\pi kl} \tag{E.16a}$$

$$\Delta T(r=\infty, t>0)=0 \tag{E.16b}$$

We solve Eq. (E.15) subject to boundary conditions given by Eq. (E.16) as in the previous section E.1 to get the solution for the temperature amplitude in terms of position

$$\Delta T(r)=\frac{P}{\pi kl}K_0(q_f r) \tag{E.17}$$

where $q_f \equiv \left(\frac{i2\omega}{\alpha}\right)^{1/2}$

E.3 Solution of hyperbolic heat conduction equation with non Fourier boundary condition

The governing equation and the boundary condition are as follows,

$$\tau\frac{\partial^2 T}{\partial t^2}+\frac{\partial T}{\partial t}=\alpha\left(\frac{\partial^2 T}{\partial r^2}+\frac{1}{r}\frac{\partial T}{\partial r}\right) \tag{E.18}$$

$$lim_{r\to 0} r\frac{\partial T}{\partial r}=-\frac{Pe^{i2\omega t}}{\pi kl}\left(1+i2\omega\tau\right) \tag{E.19a}$$

$$T(r=\infty, t>0)=0 \tag{E.19b}$$

$$T(r, t=0)=0 \tag{E.19c}$$

We can solve the Eqs. (E.18) and (E.19) as given in section E.1 to get the solution of the temperature amplitude in terms of position

$$\Delta T(r)=\frac{P\left(1+i2\tau\omega\right)}{\pi kl}K_0(qr) \tag{E.20}$$

where $q \equiv \left(\frac{i2\omega}{\alpha} - \frac{4\tau\omega^2}{\alpha} \right)^{1/2}$

E.4 Solution of Fourier equation with non Fourier boundary condition

The governing equation and the boundary conditions are as given below,

$$\frac{\partial T}{\partial t} = \alpha \left(\frac{\partial^2 T}{\partial r^2} + \frac{1}{r} \frac{\partial T}{\partial r} \right) \tag{E.21}$$

$$lim_{r \to 0} r \frac{\partial T}{\partial r} = -\frac{P e^{i2\omega t}}{\pi k l} \left(1 + i2\omega\tau\right) \tag{E.22a}$$

$$\Delta T(r = \infty, t > 0) = 0 \tag{E.22b}$$

$$T(r, t = 0) = 0 \tag{E.22c}$$

The above Eqs (E.21) and (E.22) can be solved using the methodology described in Section E.2 to get the solution of the temperature amplitude in terms of position,

$$\Delta T(r) = \frac{P\left(1 + i2\tau\omega\right)}{\pi k l} K_0(q_f r) \tag{E.23}$$

where $q_f \equiv \left(\frac{i2\omega}{\alpha} \right)^{1/2}$

Appendix F: Finite width of metal line

The line source solution considers all the heat to be deposited through a line with zero width. However, in reality the metal line will have a width 2b and we can assume the heat to be deposited over the width 2b of the metal line. The heat can be considered to be deposited over a square wave (H(x)) of width 2b over the sample and can be mathematically expressed as

$$H(x)=\begin{cases}\dfrac{1}{2b} & if\ -b\le x\le b\\ 0 & elsewhere\end{cases} \tag{F.1}$$

Since H(x) is an even function symmetrical over x = 0, the Fourier transform of the function can be expressed as

$$H(z)=\int_{-\infty}^{\infty}H(x)\cos(zx)dx \tag{F.2}$$

Using Eq. (F.1) in Eq. (F.2), the integral becomes

$$H(z)=\frac{1}{2b}\int_{-b}^{b}\cos(zx)dx \tag{F.3}$$

The integral can then be solved to give the Fourier transform of the heat source

$$H(z)=\frac{\sin(zb)}{zb} \tag{F.4}$$

The temperature oscillations measured by the metal line considered as a line source contains modified Bessel function of the second kind. Therefore the temperature

oscillations $\Delta T(x)$ can be considered to be an even function over x = 0. The Fourier transform is given by

$$\Delta T(z) = \int_{-\infty}^{\infty} \Delta T(x)\cos(zx)dx \tag{F.5}$$

F.1 Solution of hyperbolic heat conduction equation with Fourier boundary condition

The temperature oscillations measured by the metal line as a line source is given by

$$\Delta T(x) = \frac{P}{\pi kl} K_0(qx) \tag{F.6}$$

Using Eq. (F.6) in Eq. (F.5), we have

$$\Delta T(z) = \frac{P}{\pi kl} \int_{-\infty}^{\infty} K_0(qx)\cos(zx)dx \tag{F.7}$$

Eq. (F.7) can be solved using standard integral transform [99] to give

$$\Delta T(z) = \frac{P}{kl} \frac{1}{\left(z^2 + q^2\right)^{1/2}} \tag{F.8}$$

Using convolution of Fourier transforms, we get from Eqs. (F.8) and (F.4)

$$\Delta T(z) = \frac{P}{kl} \frac{\sin(zb)}{(zb)\left(z^2 + q^2\right)^{1/2}} \tag{F.9}$$

Taking inverse Fourier transform and taking the average over the width (2b) of the metal line, we have

$$\Delta T(x) = \frac{P}{\pi kl}\frac{1}{b}\int_0^b \int_0^\infty \frac{\sin(zb)\cos(zx)}{(zb)(z^2+q^2)^{1/2}}\,dzdx \tag{F.10}$$

Integrating over x, gives the temperature oscillations measured by the metal line

$$\Delta T = \frac{P}{\pi kl}\int_0^\infty \frac{\sin^2(zb)}{(zb)^2(z^2+q^2)^{1/2}}\,dz \tag{F.11}$$

F.2 Solution of Fourier equation with Fourier boundary condition

The temperature oscillations measured by the metal line as a line source is given by

$$\Delta T(x) = \frac{P}{\pi kl}K_0(q_f x) \tag{F.12}$$

Using Eq. (F.6) in Eq. (F.5), we have

$$\Delta T(z) = \frac{P}{\pi kl}\int_{-\infty}^{\infty} K_0(q_f x)\cos(zx)dx \tag{F.13}$$

Eq. (F.13) can be solved using standard integral transform [99] to give

$$\Delta T(z) = \frac{P}{kl}\frac{1}{\left(z^2+{q_f}^2\right)^{1/2}} \tag{F.14}$$

Using convolution of Fourier transforms, we get from Eqs. (F.14) and (F.4)

$$\Delta T(z) = \frac{P}{kl} \frac{\sin(zb)}{(zb)\left(z^2 + {q_f}^2\right)^{1/2}} \tag{F.15}$$

Taking inverse Fourier transform and taking the average over the width (2b) of the metal line, we have

$$\Delta T(x) = \frac{P}{\pi kl} \frac{1}{b} \int_0^b \int_0^\infty \frac{\sin(zb)\cos(zx)}{(zb)(z^2 + {q_f}^2)^{1/2}} dz dx \tag{F.16}$$

Integrating over x, gives the temperature oscillations measured by the metal line

$$\Delta T = \frac{P}{\pi kl} \int_0^\infty \frac{\sin^2(zb)}{(zb)^2 (z^2 + {q_f}^2)^{1/2}} dz \tag{F.17}$$

F.3 Solution of hyperbolic heat conduction equation with non Fourier boundary condition

The temperature oscillations measured by the metal line as a line source is given by,

$$\Delta T(r) = \frac{P(1 + i2\tau\omega)}{\pi kl} K_0(qr) \tag{F.18}$$

The finite width of the metal line can be incorporated into Eq. (F.18) by following steps similar to section F.1 to obtain the amplitude of temperature oscillations measured by the metal line of width 2b,

$$\Delta T = \frac{P(1+i2\tau\omega)}{\pi kl}\int_0^\infty \frac{\sin^2(zb)}{(zb)^2(z^2+q^2)^{1/2}}\,dz \tag{F.19}$$

F.4 Solution of Fourier equation with Fourier boundary condition

The temperature oscillations measured by the metal line as a line source is given by,

$$\Delta T(r) = \frac{P(1+i2\tau\omega)}{\pi kl} K_0(q_f r) \tag{F.20}$$

The finite width of the metal line can be incorporated into Eq. (F.20) by following steps similar to section F.2 to obtain the amplitude of temperature oscillations measured by the metal line of width 2b,

$$\Delta T = \frac{P(1+i2\tau\omega)}{\pi kl}\int_0^\infty \frac{\sin^2(zb)}{(zb)^2(z^2+q_f{}^2)^{1/2}}\,dz \tag{F.21}$$

Appendix G: Temperature amplitude solution

G.1 Solution of hyperbolic heat conduction equation with Fourier boundary condition

The amplitude of the temperature oscillations measured by the metal line is given by

$$\Delta T = \frac{P}{\pi k l}\int_0^{1/b}\frac{1}{(z^2+q^2)^{1/2}}dz \tag{G.1}$$

From the table of integrals [99] and substituting the definition of q, the Eq. (G.1) becomes

$$\Delta T = \frac{P}{\pi k l}\left[\ln\left(1+\sqrt{1-\frac{4\omega^2\tau b^2}{\alpha}+\frac{i2\omega b^2}{\alpha}}\right)-\ln\left(\sqrt{\frac{4\omega^2\tau b^2}{\alpha}+\frac{i2\omega b^2}{\alpha}}\right)\right] \tag{G.2}$$

The square roots of the complex numbers in the above equation can be solved using [100] to give

$$\Delta T = \frac{P}{\pi k l}\left[\ln(1+m+in)-\frac{1}{2}\ln\left(\frac{4\omega^2\tau b^2}{\alpha}+\frac{i2\omega b^2}{\alpha}\right)\right] \tag{G.3}$$

where,

$$m = \frac{1}{\sqrt{2}}\sqrt{1-\frac{4\tau\omega^2 b^2}{\alpha}+\sqrt{\left(1-\frac{4\tau\omega^2 b^2}{\alpha}\right)^2+\frac{4\omega^2 b^4}{\alpha^2}}} \tag{G.4}$$

$$n = \frac{\omega b^2}{\alpha m} \tag{G.5}$$

Using the definition of natural logarithm of a complex number, the Eq. (G.3) simplifies to the following real and imaginary parts

$$\Delta T = \mathrm{Re}(\Delta T) + i\,\mathrm{Im}(\Delta T) \tag{G.6}$$

where,

$$\mathrm{Re}(\Delta T) = \frac{P}{\pi k l}\left[\frac{1}{2}\ln\left((1+m)^2 + n^2\right) - \frac{1}{2}\ln\omega - \frac{1}{4}\ln\left(4\tau^2\omega^2 + 1\right) - \frac{1}{4}\ln\frac{4b^4}{\alpha^2}\right] \tag{G.7}$$

$$\mathrm{Im}(\Delta T) = \frac{P}{\pi k l}\left[i\left(\tan^{-1}\left(\frac{n}{1+m}\right) - \frac{1}{2}\tan^{-1}\left(\frac{1}{-2\tau\omega}\right)\right)\right] \tag{G.8}$$

G.2 Solution of Fourier equation with Fourier boundary condition

The amplitude of the temperature oscillations measured by the metal line is given by

$$\Delta T = \frac{P}{\pi k l}\int_0^{1/b} \frac{1}{(z^2 + q_f{}^2)^{1/2}}\,dz \tag{G.9}$$

From the table of integrals [99] and substituting the definition of q_f, the Eq. (G.9) becomes

$$\Delta T = \frac{P}{\pi k l}\left[\ln\left(1+\sqrt{1+\frac{i2\omega b^2}{\alpha}}\right)-\ln\left(\sqrt{\frac{i2\omega b^2}{\alpha}}\right)\right] \tag{G.10}$$

Taking the square roots of the complex numbers [100] in the above equation gives

$$\Delta T = \frac{P}{\pi k l}\left[\ln\left(1+m+in\right)-\frac{1}{2}\ln\left(\frac{i2\omega b^2}{\alpha}\right)\right] \tag{G.11}$$

where,

$$m = \frac{1}{\sqrt{2}}\sqrt{1+\sqrt{1+\frac{4\omega^2 b^4}{\alpha^2}}} \tag{G.12}$$

$$n = \frac{\omega b^2}{\alpha m} \tag{G.13}$$

Using the definition of natural logarithm of a complex number, Eq. (G.11) simplifies to

$$\Delta T = \mathrm{Re}\left(\Delta T\right) + i\,\mathrm{Im}\left(\Delta T\right) \tag{G.14}$$

where,

$$\mathrm{Re}\left(\Delta T\right) = \frac{P}{\pi k l}\left[\frac{1}{2}\ln\left(\left(1+m\right)^2+n^2\right)-\frac{1}{2}\ln\omega-\frac{1}{4}\ln\frac{4b^4}{\alpha^2}\right] \tag{G.15}$$

$$\mathrm{Im}\left(\Delta T\right) = \frac{P}{\pi k l}\left[i\left(\tan^{-1}\left(\frac{n}{1+m}\right)-\frac{\pi}{4}\right)\right] \tag{G.16}$$

G.3 Solution of hyperbolic heat conduction equation with non Fourier boundary condition

The amplitude of the temperature oscillations measured by the metal line for the condition where $|qb| \square\ 1$ is given by

$$\Delta T = \frac{P(1+i2\tau\omega)}{\pi kl}\int_0^{1/b}\frac{1}{(z^2+q^2)^{1/2}}dz \tag{G.17}$$

The Eq. (G.17) can be solved as shown in section G.1 to give the real and imaginary parts of the temperature amplitude

$$\Delta T = \mathrm{Re}(\Delta T) + i\,\mathrm{Im}(\Delta T) \tag{G.18}$$

and

$$\mathrm{Re}(\Delta T) = \frac{P}{\pi kl}\left[\frac{\ln\left((1+m)^2+n^2\right)}{2} - \frac{\ln\omega}{2} - \frac{\ln\left(4\tau^2\omega^2+1\right)}{4} - \frac{1}{4}\ln\frac{4b^4}{\alpha^2} - 2\tau\omega\left(\tan^{-1}\left(\frac{n}{1+m}\right) - \frac{1}{2}\tan^{-1}\left(\frac{1}{-2\tau\omega}\right)\right)\right] \tag{G.19}$$

$$\mathrm{Im}(\Delta T) = \frac{P(2\tau\omega)}{\pi kl}\left[\frac{\ln\left((1+m)^2+n^2\right)}{2} - \frac{\ln\omega}{2} - \frac{\ln\left(4\tau^2\omega^2+1\right)}{4} - \frac{1}{4}\ln\frac{4b^4}{\alpha^2} + \frac{1}{2\tau\omega}\left(\tan^{-1}\left(\frac{n}{1+m}\right) - \frac{1}{2}\tan^{-1}\left(\frac{1}{-2\tau\omega}\right)\right)\right] \tag{G.20}$$

where

$$m = \frac{1}{\sqrt{2}}\sqrt{1 - \frac{4\tau\omega^2b^2}{\alpha}\sqrt{\left(1 - \frac{4\tau\omega^2b^2}{\alpha}\right)^2 + \frac{4\omega^2b^4}{\alpha^2}}} \tag{G.21}$$

and

$$n = \frac{\omega b^2}{\alpha m} \tag{G.22}$$

G.4 Solution of Fourier equation with non Fourier boundary condition

The amplitude of the temperature oscillations measured by the metal line for the condition where $|q_f b| \ll 1$ is given by

$$\Delta T = \frac{P(1+i2\tau\omega)}{\pi k l} \int_0^{1/b} \frac{1}{(z^2+q^2)^{1/2}} dz \tag{G.23}$$

The Eq. (G.23) can be solved as shown in section G.2 to give the real and imaginary parts of the temperature amplitude

$$\Delta T = \mathrm{Re}(\Delta T) + i\,\mathrm{Im}(\Delta T) \tag{G.24}$$

and

$$\mathrm{Re}(\Delta T) = \frac{P}{\pi k l}\left[\frac{\ln\left((1+m)^2+n^2\right)}{2} - \frac{\ln\omega}{2} - \frac{1}{4}\ln\frac{4b^4}{\alpha^2} - 2\tau\omega\left(\tan^{-1}\left(\frac{n}{1+m}\right) - \frac{\pi}{4}\right)\right] \tag{G.25}$$

$$\mathrm{Im}(\Delta T) = \frac{P(2\tau\omega)}{\pi k l}\left[\frac{\ln\left((1+m)^2+n^2\right)}{2} - \frac{\ln\omega}{2} - \frac{1}{4}\ln\frac{4b^4}{\alpha^2} + \frac{1}{2\tau\omega}\left(\tan^{-1}\left(\frac{n}{1+m}\right) - \frac{\pi}{4}\right)\right] \tag{G.26}$$

where

$$m = \frac{1}{\sqrt{2}}\sqrt{1+\sqrt{1+\frac{4\omega^2 b^4}{\alpha^2}}} \tag{G.27}$$

and

$$n = \frac{\omega b^2}{\alpha m} \tag{G.28}$$

References

[1] J. Hone, M. Whitney, C. Piskoti, A. Zettl, Thermal conductivity of single-walled carbon nanotubes, Physical Review B, 59(4) (1999) R2514-R2516.

[2] P. Kim, L. Shi, A. Majumdar, P.L. McEuen, Thermal transport measurements of individual multiwalled nanotubes, Physical Review Letters, 87(21) (2001) 215502.

[3] H.L. Zhang, J.F. Li, B.P. Zhang, K.F. Yao, W.S. Liu, H. Wang, Electrical and thermal properties of carbon nanotube bulk materials: Experimental studies for the 328-958 K temperature range, Physical Review B, 75(20) (2007) 205407.

[4] A.E. Aliev, M.H. Lima, E.M. Silverman, R.H. Baughman, Thermal conductivity of multi-walled carbon nanotube sheets: radiation losses and quenching of phonon modes, Nanotechnology, 21(3) (2010) 035709.

[5] J. Hone, M.C. Llaguno, M.J. Biercuk, A.T. Johnson, B. Batlogg, Z. Benes, J.E. Fischer, Thermal properties of carbon nanotubes and nanotube-based materials, Applied Physics a-Materials Science & Processing, 74(3) (2002) 339-343.

[6] S. Iijima, Helical Microtubules of Graphitic Carbon, Nature, 354(6348) (1991) 56-58.

[7] A. Jorio, M.S. Dresselhaus, G. Dresselhaus, Carbon nanotubes: advanced topics in synthesis, structure, properties and applications, Springer, Heidelberg, 1959, pp. 4.

[8] R.H. Baughman, A.A. Zakhidov, W.A. de Heer, Carbon nanotubes - the route toward applications, Science, 297(5582) (2002) 787-792.

[9] E.T. Thostenson, C.Y. Li, T.W. Chou, Nanocomposites in context, Composites Science and Technology, 65(3-4) (2005) 491-516.

[10] S. Berber, Y.K. Kwon, D. Tomanek, Unusually high thermal conductivity of carbon nanotubes, Physical Review Letters, 84(20) (2000) 4613-4616.

[11] M.S. Dresselhaus, G. Dresselhaus, P. Avouris, Carbon nanotubes: synthesis, structure, properties and applications, Springer, Heidelberg, 2001, pp. 282.

[12] V. Varshney, S.S. Patnaik, A.K. Roy, B.L. Farmer, Modeling of Thermal Conductance at Transverse CNT-CNT Interfaces, Journal of Physical Chemistry C, 114(39) (2010) 16223-16228.

[13] S. Liwei, M. Liu, W. Wei, Diameter-dependant thermal conductance models of carbon nanotubes, in: Nanotechnology, 2007. IEEE-NANO 2007. 7th IEEE Conference on, 2007, pp. 206-210.

[14] N. Jain, Harsh, Analysis of thermal conductance of carbon nanotubes, European Physical Journal-Applied Physics, 51(1) (2010) 10602.

[15] D.B. Tuckerman, R.F.W. Pease, High-performance heat sinking for VLSI, IEEE Electronic Device Letters 2, (1981) 126-129.

[16] T.M. Tritt, Thermal conductivity: theory, properties and applications, Kluwer Academic/Plenum Publishers, New York, 2004, pp. 167.

[17] D.P. Almond, P.M. Patel, Photothermal science and techniques, Chapman and Hall, London, 1996, pp. 216.

[18] W.S. Capinski, H.J. Maris, T. Ruf, M. Cardona, K. Ploog, D.S. Katzer, Thermal-conductivity measurements of GaAs/AlAs superlattices using a picosecond optical pump-and-probe technique, Physical Review B, 59(12) (1999) 8105-8113.

[19] K. Katayama, H. Yui, T. Sawada, Recent development of photothermal and photoacoustic spectroscopy, Jpn. Soc. Appl. Phys., 70 (2001) 272-276.

[20] D.G. Cahill, Thermal Conductivity Measurement from 30 K to 750 K : the 3 Omega Method, Review of Scientific Instruments, 61(2) (1990) 802-808.

[21] D.D. Joseph, L. Preziosi, Heat Waves, Reviews of Modern Physics, 62(2) (1990) 375-391.

[22] M.E. Steinke, S.G. Kandlikar, Single-phase heat transfer techniques in microchannel and minichannel flows, in: Proceedings of the ASME 2004 2nd International Conference on Microchannels and Minichannels, ASME, Rochestor, New York, 2004, pp. 141-148.

[23] X.L. Xie, Z.J. Liu, Y.L. He, W.Q. Tao, Numerical study of laminar heat transfer and pressure drop characteristics in a water-cooled minichannel heat sink, Applied Thermal Engineering, 29(1) (2009) 64-74.

[24] S. Reynaud, F. Debray, J.P. Franc, T. Maitre, Hydrodynamics and heat transfer in two-dimensional minichannels, International Journal of Heat and Mass Transfer, 48(15) (2005) 3197-3211.

[25] R. Schmidt, Challenges in electronic cooling - Opportunities for enhanced thermal management techniques - Microprocessor liquid cooled minichannel heat sink, Heat Transfer Engineering, 25(3) (2004) 3-12.

[26] W.L. Qu, I. Mudawar, Experimental and numerical study of pressure drop and heat transfer in a single-phase micro-channel heat sink, International Journal of Heat and Mass Transfer, 45(12) (2002) 2549-2565.

[27] M.E. Steinke, S.G. Kandlikar, Single-phase liquid heat transfer in plain and enhanced microchannels, in: Proceedings of the ASME 4th International Conference on Nanochannels, Microchannels and Minichannels, Parts A and B, ASME, Limerick, England, 2006, pp. 943-951.

[28] R. Narayanaswamy, T.T. Chandratilleke, A.J.L. Foong, Laminar convective heat transfer in microchannel with internal fins, in: Proceedings of the ASME 6th International Conference on Nanochannels, Microchannels and Minichannels, ASME, Darmstadt, Germany, 2008, pp. 159-163.

[29] S.G. Kandlikar, Fundamental issues related to flow boiling in minichannels and microchannels, Experimental Thermal and Fluid Science, 26(2-4) (2002) 389-407.

[30] G. Wang, P. Cheng, H. Wu, Unstable and stable flow boiling in parallel microchannels and in a single microchannel, International Journal of Heat and Mass Transfer, 50(21-22) (2007) 4297-4310.

[31] W.L. Qu, I. Mudawar, Flow boiling heat transfer in two-phase micro-channel heat sinks - I. Experimental investigation and assessment of correlation methods, International Journal of Heat and Mass Transfer, 46(15) (2003) 2755-2771.

[32] R. Chein, J. Chuang, Experimental microchannel heat sink performance studies using nanofluids, International Journal of Thermal Sciences, 46(1) (2007) 57-66.

[33] S. Lee, S.U.S. Choi, S. Li, J.A. Eastman, Measuring thermal conductivity of fluids containing oxide nanoparticles, Journal of Heat Transfer-Transactions of the Asme, 121(2) (1999) 280-289.

[34] C.J. Ho, L.C. Wei, Z.W. Li, An experimental investigation of forced convective cooling performance of a microchannel heat sink with Al(2)O(3)/water nanofluid, Applied Thermal Engineering, 30(2-3) (2010) 96-103.

[35] J. Lee, I. Mudawar, Assessment of the effectiveness of nanofluids for single-phase and two-phase heat transfer in micro-channels, International Journal of Heat and Mass Transfer, 50(3-4) (2007) 452-463.

[36] B.C. Pak, Y.I. Cho, Hydrodynamic and heat transfer study of dispersed fluids with submicron metallic oxide particles, Experimental Heat Transfer, 11(2) (1998) 151-170.

[37] Y.M. Xuan, Q. Li, Investigation on convective heat transfer and flow features of nanofluids, Journal of Heat Transfer-Transactions of the Asme, 125(1) (2003) 151-155.

[38] M.S. Murshed, D. Milanova, R. Kumar, An experimental study of surface tension dependent pool boiling characteristics of carbon nanotubes-nanofluids, in: Proceedings of the ASME 7th International Conference on Nanochannels, Microchannels and Minichannels, ASME, Pohang, South Korea, 2009, pp. 75-80.

[39] K.S. Yang, Y.R. Jeng, C.M. Huang, C.C. Wang, Heat Transfer and Flow Pattern Characteristics for HFE-7100 Within Microchannel Heat Sinks, Heat Transfer Engineering, 32(7-8) (2011) 697-704.

[40] T.L. Chen, S.V. Garimella, Local heat transfer distribution and effect of instabilities during flow boiling in a silicon microchannel heat sink, International Journal of Heat and Mass Transfer, 54(15-16) (2011) 3179-3190.

[41] M.Z. Yuan, J.J. Wei, Y.F. Xue, J.B. Fang, Subcooled flow boiling heat transfer of FC-72 from silicon chips fabricated with micro-pin-fins, International Journal of Thermal Sciences, 48(7) (2009) 1416-1422.

[42] V. Khanikar, I. Mudawar, T.S. Fisher, Flow Boiling in a Micro-Channel Coated With Carbon Nanotubes, Ieee Transactions on Components and Packaging Technologies, 32(3) (2009) 639-649.

[43] N. Singh, V. Sathyamurthy, W. Peterson, J. Arendt, D. Banerjee, Flow boiling enhancement on a horizontal heater using carbon nanotube coatings, International Journal of Heat and Fluid Flow, 31(2) (2010) 201-207.

[44] Z. Mo, R. Morjan, J. Anderson, E.E.B. Campbell, J. Liu, Integrated nanotube microcooler for microelectronics applications, in: Proceedings of the IEEE Electronics Components and Technology Conference, IEEE, Laker Buena Vista, Florida 2005, pp. 51-54.

[45] B.E. Jakaboski, Y.K. Joshi, M. Rightley, Forced Convection in a microchannel heat sink using carbon nanotubes for heat transfer enhancement, Heat Transfer 2, (2004) 227-233.

[46] C.R. Dietz, Y.K. Joshi, Single-phase forced convection in microchannels with carbon nanotubes for electronics cooling applications, Nanoscale and Microscale Thermophysical Engineering, 12(3) (2008) 251-271.

[47] K.E. Bean, Anisotropic chemical etching of silicon, IEEE Transactions of Electronic Devices, 25(10) (1978) 1185-1193.

[48] M. Shimbo, K. Furukawa, K. Fukuda, K. Tanzawa, Silicon-to-Silicon Direct Bonding Method, Journal of Applied Physics, 60(8) (1986) 2987-2989.

[49] M.A. Schmidt, Wafer-to-wafer bonding for microstructure formation, Proceedings of the Ieee, 86(8) (1998) 1575-1585.

[50] M. Roode, Y. Bayazitoglu, Wetting physics of water-carbon nanocarpet interfaces, in: ICHMT Proceedings of Thermal and Materials Nanoscience and Nanotechnology, Begell House, Antalya, Turkey, 2011.

[51] S.M. Lee, S.I. Kwun, Heat Capacity Measurement of Dielectric Solids Using a Linear Surface Heater - Application to Ferroelectrics, Review of Scientific Instruments, 65(4) (1994) 966-970.

[52] S.M. Lee, D.G. Cahill, Heat transport in thin dielectric films, Journal of Applied Physics, 81(6) (1997) 2590-2595.

[53] T. Yamane, N. Nagai, S. Katayama, M. Todoki, Measurement of thermal conductivity of silicon dioxide thin films using a 3 omega method, Journal of Applied Physics, 91(12) (2002) 9772-9776.

[54] T. Tong, A. Majumdar, Reexamining the 3 omega technique for thin film thermal characterization, Review of Scientific Instruments, 77(10) (2006) 104902.

[55] C.E. Raudzis, F. Schatz, D. Wharam, Extending the 3 omega method for thin-film analysis to high frequencies, Journal of Applied Physics, 93(10) (2003) 6050-6055.

[56] S. Ahmed, R. Liske, T. Wunderer, M. Leonhardt, R. Ziervogel, C. Fansler, T. Grotjohn, J. Asmussen, T. Schuelke, Extending the 3 omega-method to the MHz range

for thermal conductivity measurements of diamond thin films, Diamond and Related Materials, 15(2-3) (2006) 389-393.

[57] P.B. Kaul, K.A. Day, A.R. Abramson, Application of the three omega method for the thermal conductivity measurement of polyaniline, Journal of Applied Physics, 101(8) (2007) 083507.

[58] X.J. Hu, A.A. Padilla, J. Xu, T.S. Fisher, K.E. Goodson, 3-omega measurements of vertically oriented carbon nanotubes on silicon, Journal of Heat Transfer-Transactions of the Asme, 128(11) (2006) 1109-1113.

[59] A. Jacquot, F. Vollmer, B. Bayer, M. Jaegle, D.G. Ebling, H. Bottner, Thermal Conductivity Measurements on Challenging Samples by the 3 Omega Method, Journal of Electronic Materials, 39(9) (2010) 1621-1626.

[60] C. Cattaneo, A form of heat conduction equation which eliminates the paradox of instantaneous propagation, Comptes Rendus, 247 (1958) 431-433.

[61] P. Vernotte, Les paradoxes de la theorie continue de l'equation de la chaleur, Comptes Rendus, 246 (1958) 3145-3155.

[62] C. Bai, M. Chung, A.S. Lavine, Transient heat transfer in thin films, in: ASME/JSME Thermal Engineering Joint Conference, ASME, Maui, HI, 1995, pp. 511-517.

[63] Z.M. Tan, W.J. Yang, Propagation of thermal waves in transient heat conduction in a thin film, Journal of the Franklin Institute-Engineering and Applied Mathematics, 336B(1) (1999) 185-197.

[64] H.T. Chen, K.C. Liu, Study of hyperbolic heat conduction problem in the film and substrate composite with the interface resistance, Japanese Journal of Applied Physics Part 1-Regular Papers Short Notes & Review Papers, 41(10) (2002) 6267-6275.

[65] H. Herwig, K. Beckert, Experimental evidence about the controversy concerning Fourier or non-fourier heat conduction in materials with a nonhomogeneous inner structure, Heat and Mass Transfer, 36(5) (2000) 387-392.

[66] T.J. Bright, Z.M. Zhang, Common Misperceptions of the Hyperbolic Heat Equation, Journal of Thermophysics and Heat Transfer, 23(3) (2009) 601-607.

[67] W. Kaminski, Hyperbolic Heat Conduction Equation for Materials with a Nonhomogeneous Inner Structure, Journal of Heat Transfer-Transactions of the Asme, 112(3) (1990) 555-560.

[68] K. Mitra, S. Kumar, A. Vedavarz, M.K. Moallemi, Experimental Evidence of Hyperbolic Heat Conduction in Processed Meat, Journal of Heat Transfer-Transactions of the Asme, 117(3) (1995) 568-573.

[69] M. Jaunich, S. Raje, K. Kim, K. Mitra, Z.X. Guo, Bio-heat transfer analysis during short pulse laser irradiation of tissues, International Journal of Heat and Mass Transfer, 51(23-24) (2008) 5511-5521.

[70] F. Xu, K.A. Seffen, T.J. Lu, Non-Fourier analysis of skin biothermomechanics, International Journal of Heat and Mass Transfer, 51(9-10) (2008) 2237-2259.

[71] M.N. Ozisik, B. Vick, Propagation and Reflection of Thermal Waves in a Finite Medium, International Journal of Heat and Mass Transfer, 27(10) (1984) 1845-1854.

[72] C. Korner, H.W. Bergmann, The physical defects of the hyperbolic heat conduction equation, Applied Physics a-Materials Science & Processing, 67(4) (1998) 397-401.

[73] A. Barletta, E. Zanchini, Hyperbolic heat conduction and local equilibrium: A second law analysis, International Journal of Heat and Mass Transfer, 40(5) (1997) 1007-1016.

[74] D. Jou, J. Casasvazquez, G. Lebon, Extended Irreversible Thermodynamics, Reports on Progress in Physics, 51(8) (1988) 1105-1179.

[75] M. Chester, Second Sound in Solids, Physical Review, 131(5) (1963) 2013-&.

[76] S.L. Shinde, S.G. Jitendra, High thermal conductivity materials, Springer, New York, 2005, pp. 210.

[77] Y. Li, R.E. Taylor, A. Nabi, Thermal-Diffusivity Measurement of Cvd Diamond Film Using a Step Heating Technique, International Journal of Thermophysics, 14(2) (1993) 285-295.

[78] Y. Isono, H. Kishimoto, T. Tanaka, Evaluation of mechanical and thermal properties of cubic boron nitride by ab-initio calculation, Materials Science Research International, 4(1) (1998) 39-44.

[79] T. Atake, A. Honda, Y. Saito, K. Saito, Low-Temperature Heat-Capacity of Cubic Boron-Nitride, Japanese Journal of Applied Physics Part 2-Letters, 29(10) (1990) L1869-L1870.

[80] S.F. Wang, Y.F. Hsu, J.C. Pu, J.C. Sung, L.G. Hwa, Determination of acoustic wave velocities and elastic properties for diamond and other hard materials, Materials Chemistry and Physics, 85(2-3) (2004) 432-437.

[81] G. Yang, A.D. Migone, K.W. Johnson, Heat-Capacity and Thermal-Diffusivity of a Glass Sample, Physical Review B, 45(1) (1992) 157-160.

[82] J. Ordonez-Miranda, J.J. Alvarado-Gil, Thermal wave oscillations and thermal relaxation time determination in a hyperbolic heat transport model, International Journal of Thermal Sciences, 48(11) (2009) 2053-2062.

[83] S. Galovic, D. Kostoski, Photothermal wave propagation in media with thermal memory, Journal of Applied Physics, 93(5) (2003) 3063-3070.

[84] A. Barletta, E. Zanchini, Hyperbolic heat conduction and thermal resonances in a cylindrical solid carrying a steady periodic electric field, International Journal of Heat and Mass Transfer, 39(6) (1996) 1307-1315.

[85] R. Shirmohammadi, A. Moosaie, Non-Fourier heat conduction in a hollow sphere with periodic surface heat flux, International Communications in Heat and Mass Transfer, 36(8) (2009) 827-833.

[86] D.W. Tang, N. Araki, Non-Fourier heat conduction in a finite medium under periodic surface thermal disturbance, International Journal of Heat and Mass Transfer, 39(15) (1996) 3305-3308.

[87] C. Kittel, Introduction to solid state physics, 8th ed., John Wiley & Sons, Hoboken, 2005, pp. 156.

[88] Q. Chen, Carbon nanotube reinforced metal composite, U.S. Patent 7,651,766 B2, issued Jan. 26, 2010.

[89] Y.L. Yang, Y.D. Wang, Y. Ren, C.S. He, J.N. Deng, J. Nan, J.G. Chen, L. Zuo, Single-walled carbon nanotube-reinforced copper composite coatings prepared by electrodeposition under ultrasonic field, Materials Letters, 62(1) (2008) 47-50.

[90] W.M. Daoush, Processing and characterization of CNT/Cu nanocomposites by powder technology, Powder Metallurgy and Metal Ceramics, 47(9-10) (2008) 531-537.

[91] S.M. Uddin, T. Mahmud, C. Wolf, C. Glanz, I. Kolaric, C. Volkmer, H. Holler, U. Wienecke, S. Roth, H.J. Fecht, Effect of size and shape of metal particles to improve hardness and electrical properties of carbon nanotube reinforced copper and copper alloy composites, Composites Science and Technology, 70(16) (2010) 2253-2257.

[92] K. Chu, Q.Y. Wu, C.C. Jia, X.B. Liang, J.H. Nie, W.H. Tian, G.S. Gai, H. Guo, Fabrication and effective thermal conductivity of multi-walled carbon nanotubes reinforced Cu matrix composites for heat sink applications, Composites Science and Technology, 70(2) (2010) 298-304.

[93] E. Khar, Metals Handbook, 9th ed., American Society for Metals, Metals Park, 1984, pp. 117.

[94] Y.H. Wang, H.W. Shan, R.H. Hauge, M. Pasquali, R.E. Smalley, A highly selective, one-pot purification method for single-walled carbon nanotubes, Journal of Physical Chemistry B, 111(6) (2007) 1249-1252.

[95] T. Kuzumaki, K. Miyazawa, H. Ichinose, K. Ito, Processing of carbon nanotube reinforced aluminum composite, Journal of Materials Research, 13(9) (1998) 2445-2449.

[96] S.J. Kline, F.A. McClintock, Describing uncertainties in single sample experiments, Mechanical Engineering, 75(1) (1953) 38.

[97] H.S. Carslaw, J.C. Jaeger, Conduction of heat in solids, 2 ed., Oxford University Press, Oxford, 1959, pp. 193.

[98] C. Cercignani, G.M. Kremer, The Relativistic Boltzmann Equation: Theory and Applications, Birkhauser Verlag, Basel, 2002, pp. 69.

[99] A. Erdelyi, Table of integral transforms, McGraw-Hill, New York, 1954, pp. 49.

[100] A. Mostowski, M. Stark, Introduction to higher algebra, Pergamon Press, New York, 1964, pp. 49.